#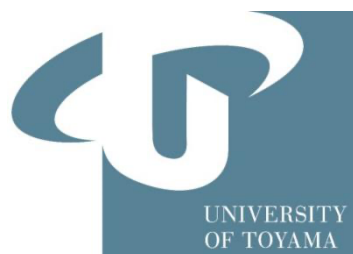 Dual engineering of olivetolic acid cyclase and tetraketide synthase for the formation of longer alkyl-chain olivetolic acid analogs and their antibacterial activities

LEE YUAN-E

SECTION OF NATURAL PRODUCTS

& DRUG DISCOVERY

INSTITUTE OF NATURAL MEDICINE

UNIVERSITY OF TOYAMA

2023

Dual engineering of olivetolic acid cyclase and tetraketide synthase for the formation of longer alkyl-chain olivetolic acid analogs and their antibacterial activities

By

LEE YUAN-E

A dissertation submitted to the

Graduate School of Medicine and Pharmaceutical Sciences

University of Toyama

In fulfillment of the requirements for the

Degree of Doctor of Philosophy

2023

Table of contents

Abbreviations

AtHS1	*Arabidopsis thaliana* heat stable protein
CB1	cannabinoid receptor type 1
CB2	cannabinoid receptor type 2
CBD	cannabidiol
CHS	chalcone synthase
DABB	dimeric $\alpha+\beta$ barrel
GST	glutathione *S*-transferase
IPTG	isopropyl-β-D-1-thiogalactopyranoside
OA	olivetolic acid
OAC	olivetolic acid cyclase
PET	perrottetinene
PKS	polyketide synthase
PF	Photon Factory
PSP	PreScission Protease
SP1	*Populus tremula* boiling stable protein
THCA	tetrahydrocannabinolic acid
THC	Δ^9-tetrahydrocannabinol
TKS	tetraketide synthase

Introduction

Δ^9-Tetrahydrocannabinol (Δ^9-THC) and cannabidiol (CBD) are the two most studied and pharmacologically interesting phytocannabinoids that are prospective compounds for the treatment of chronic pain, stress, anxiety, depression, and insomnia (**Fig. 1**).[1] The pharmacological activities of these cannabinoids principally occur through their interactions with two G-protein-coupled receptors (GPCRs), cannabinoid receptors (CB1 and CB2), which mediates the biological effects of the human endocannabinoid system.[2] In particular, the psychotropic effect of Δ^9-THC is shown to be mediated by the partial agonist activity at CB1 receptors. In addition, Δ^9-THC and CBD also exert other effects at the molecular targets outside the endocannabinoid system which involves a complex aggregate of several therapeutic targets, multiple signaling pathways, and ion channels.[3] The use of cannabis strains containing Δ^9-tetrahydrocannabinolic acid (Δ^9-THCA) and cannabidiolic acid (CBDA), which are precursor of Δ^9-THC and CBD, has been approved for the treatment of chronic pain in adults. In addition, the use of cannabis is reported to show improvement in disease-related symptoms such as pain, spasticity, nausea, multiple sclerosis, epilepsy, and glaucoma.[4-8] However, acute effects such as psychoactive, mild euphoric, 'high' or relaxing intoxication which causes minor psychomotor and cognitive function changes has prevented their use as drug. This somehow brings the attention of the scientists to other non-psychoactive cannabinoids, such as cannabigerol (CBG) (**1b**), cannabigerolic acid (CBGA) (**2b**), cannabinol (CBN), cannabichromene (CBC), CBDA, and others (**Fig.1**).

Apart from these, the discovery of homologs of cannabidiol (CBD) and Δ^9-THC with *n*-heptyl moiety in the Italian FM2 cannabis variety showed that these new cannabinoids possess significant binding affinity against human CB1 receptor, which is as potent as the full CB1 agonist CP55940[9], suggesting the potential of the modification on the *n*-pentyl side chain as biological activity modulators. In addition, the identification of (−)-*cis*-perrottetinene (*cis*-PET), the C-3 phenylethyl derivative of Δ^9-THC produced by the liverwort *Radula* genus, showed that this analog penetrates the brain and induces effect such catalepsy, hypothermia, analgesia in a CB1 receptor-dependent manner, with the reduction of the Δ^9-THC-related side effects.[10] Furthermore, the elongation of the side-chain at C-3 of Δ^9-THC reportedly increased its receptor-binding affinity. These observations suggest that the C-3 alkyl side-chain

is one of the most critical pharmacophores and it is therefore interesting to create Δ^9-THC and **1b**-analogs with different alkyl-chain length for the development of better medicines. However, complicated structure with two stereocenters prevented effective chemical production of Δ^9-THC and its analogs.[11]
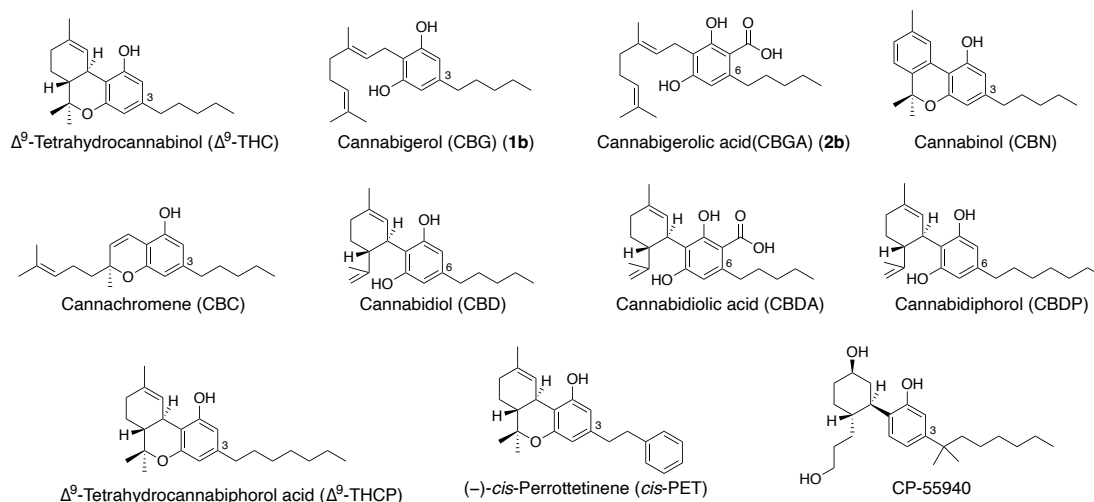

Fig. 1 Δ^9-THC and related cannabinoids.

In contrast, a yeast expression system producing Δ^9-THCA was recently developed by incorporating four biosynthetic genes, tetraketide synthase (TKS), olivetolic acid cyclase (OAC), geranylpyrophosphate:olivetolate geranyltransferase (PT4), and tetrahydrocannabinolic acid synthase (THCAS) into *Saccharomyces cerevisiae* (**Fig. 2**).[12] Among them, TKS is the type III polyketide synthase (PKS) that catalyzes the sequential condensations of three malonyl-CoAs with hexanoyl-CoA (**5b**) to produce a linear pentyltetra-β-ketide-CoA (**8b**) intermediate[13], while OAC is the polyketide cyclase that catalyzes C2-C7 aldol-type cyclization of the linear **8b** intermediate to form olivetolic acid (**3b**), the initial core of Δ^9-THC with a pentyl moiety (**Fig. 2**).[14] This expression system successfully generated Δ^9-THC analogs with butyl-, hexyl-, 3-methylpentyl-, 1-pentenyl-, and 1-hexynyl moieties (**Fig. 3**), respectively, by feeding the corresponding fatty acids into this yeast system.[12] However, simultaneously, previous study also demonstrated that this system cannot be utilized to generate Δ^9-THCA analogs with alkyl side-chain more than *n*-octyl moiety, and this is caused from the limitations of the substrate promiscuities of TKS and/or OAC, which has been verified from absence of corresponding **3b**-analogs in the products of the yeast expression system. It is thus strongly assumed that engineered

TKS and/or OAC are required to generate Δ^9-THC analogs with longer C-3 alkyl side chain by exploiting the yeast expression system.
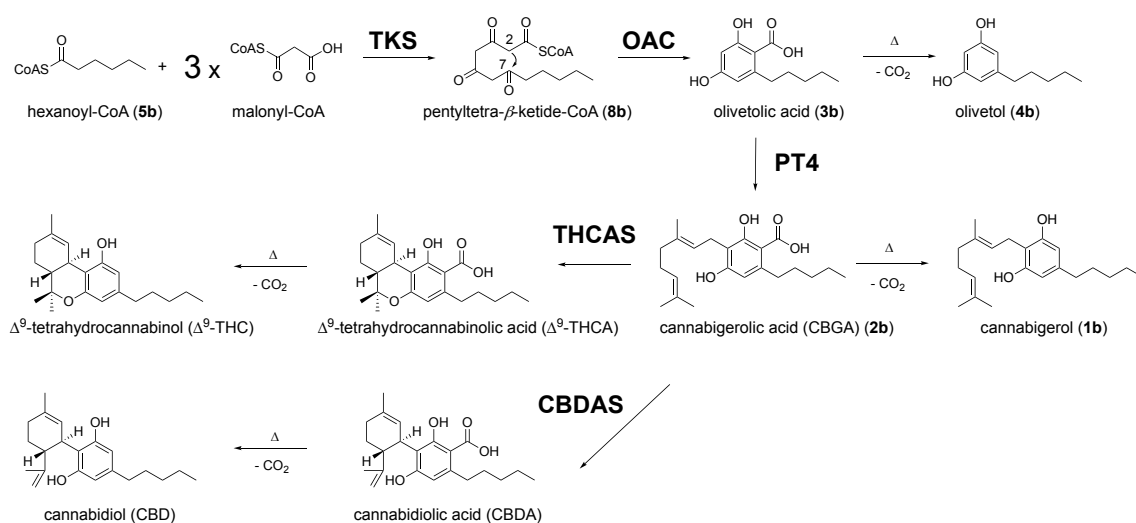

Fig 2. Biosynthesis of Δ^9-THCA and CBDA and decarboxylative productions of **1b**, **4b**, Δ^9-THC, and CBD.

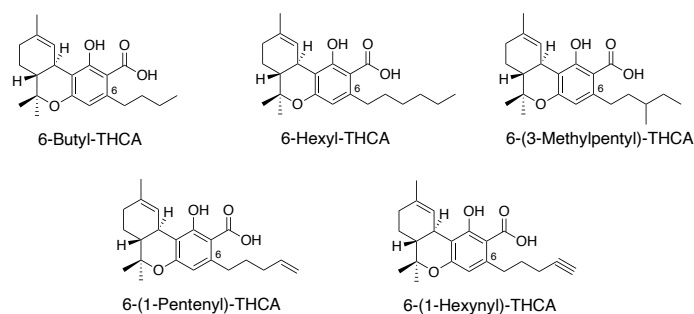**Fig. 3** Δ^9-THC analogs with butyl-, hexyl-, 3-methylpentyl-, 1-pentenyl-, and 1-hexynyl moieties produced by yeast expression system.

Meanwhile, a recent study revealed that despite its low brain penetration, compound **3b** exhibited a moderate anticonvulsant effect in a mouse model of Dravet syndrome, with comparable potency to the known anticonvulsant cannabinoid, CBD (**Fig. 1 & 2**).[15] To the best of our knowledge, no other activity has been reported for **3b**. Apart from this, compound **1b**, the prenylated analogs of **3b**, has recently received much attention due to its versatile and promising pharmacological properties. Structurally, **1b** consists of an alkylresorcinol core attached to a linear isoprenyl residue (**Fig. 1**). This prenylated cannabinoid is a potent α2-adrenoceptor agonist, moderate 5-HT$_{1A}$R competitive antagonist, and does not show undesired psychoactive

effect like Δ^9-THC (**Fig. 1**).[16-17] In addition, a recent study showed that **2b** and cannabidiolic acid (CBDA) were able to block the live severe acute respiratory syndrome coronavirus-2 (SARS-CoV-2) and the emerging variants, B.1.1.7 and B.1.351.[18] Despite having different side chains (monoterpenyl for **2b** and cyclohexene terpene ring for CBDA), the results showed equal effectiveness of **2b** and CBDA which somehow indicates that the main olivetol core could be a critical pharmacophore in the binding of ligands to the SARS-CoV-2 spike protein. In addition, **1b** and **2b** have been well studied on their antibacterial activities against *S. aureus* with MIC values ranging from 2–4 μg/mL.[19] In light of the previously reported structural role of the prenylation of the compounds[20], the **3b**-analogs with longer alkyl side-chain may be potential active compounds like **1b** and **2b**, due to the gained hydrophobicity at longer C-3 alkyl-chain.

Thus, this study aims to create OAC and TKS mutant enzymes, which can give rise to longer alkyl-chain **3b**-analogs, as well as to evaluate the antibacterial activities of the generated **3b**-analogs (**3c–e**) and their derivatives (**3a**, **3f**, **1a–f**, **2a–f**, and **4a–f**) (**Fig. 4**) against *Staphylococcus aureus* and *Bacillus subtilis* as a preliminary investigation of their biological activities. As a result, the structure-guided site-directed mutagenesis studies successfully created OAC and TKS mutants that can facilitate the formation of the cannabinoid core with a linear fatty acyl moiety up to C11.[21] Furthermore, investigations of antibacterial activities of **3b**- and its analogs, as well as their derivatives revealed that the incorporation of longer alkyl chains to the C-6 position in **3b** conferred antibacterial properties against *S. aureus* and *B. subtilis*.[22] The study also demonstrated that the *n*-heptyl alkyl chain modification at C-6 of **2b** effectively enhanced the activity against *B. subtilis*, suggesting the importance of the alkyl side-chain in modulating the bioactivity. Chapter 1 will discuss the dual engineering of TKS and OAC including their crystal structure analysis and the effect of the mutation on their enzyme activities. Finally, the antibacterial activities of the compounds shown in **Fig. 4** against two Gram-positive bacteria will be discussed in Chapter 2.
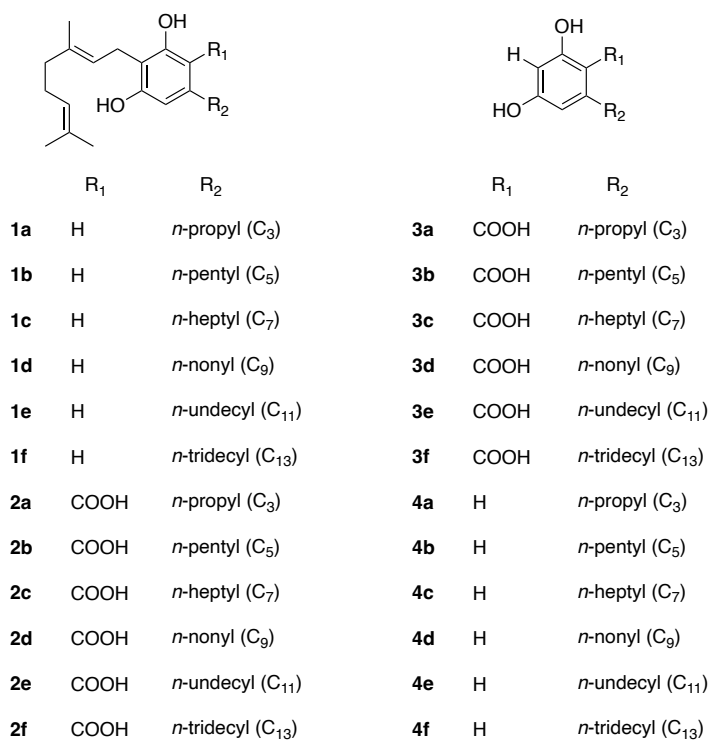
	R₁	R₂		R₁	R₂
1a	H	*n*-propyl (C₃)	**3a**	COOH	*n*-propyl (C₃)
1b	H	*n*-pentyl (C₅)	**3b**	COOH	*n*-pentyl (C₅)
1c	H	*n*-heptyl (C₇)	**3c**	COOH	*n*-heptyl (C₇)
1d	H	*n*-nonyl (C₉)	**3d**	COOH	*n*-nonyl (C₉)
1e	H	*n*-undecyl (C₁₁)	**3e**	COOH	*n*-undecyl (C₁₁)
1f	H	*n*-tridecyl (C₁₃)	**3f**	COOH	*n*-tridecyl (C₁₃)
2a	COOH	*n*-propyl (C₃)	**4a**	H	*n*-propyl (C₃)
2b	COOH	*n*-pentyl (C₅)	**4b**	H	*n*-pentyl (C₅)
2c	COOH	*n*-heptyl (C₇)	**4c**	H	*n*-heptyl (C₇)
2d	COOH	*n*-nonyl (C₉)	**4d**	H	*n*-nonyl (C₉)
2e	COOH	*n*-undecyl (C₁₁)	**4e**	H	*n*-undecyl (C₁₁)
2f	COOH	*n*-tridecyl (C₁₃)	**4f**	H	*n*-tridecyl (C₁₃)

Fig. 4 Structures of compound **1a–f**, **2a–f**, **3a–f**, and **4a–f.**

CHAPTER 1

Engineering of OAC and TKS

1.1 Introduction

As mentioned above, TKS is a member from the type III polyketide synthase family. These enzymes are reported to have broad substrate promiscuity and catalytic potential, and can accept structurally distinct various CoA-thioesters as the starter substrate with malonyl-CoA to produce different product analogs.[23-27] On the other hand, OAC is the only known plant polyketide cyclase that can accept linear-β-polyketide intermediate to produce **3b**. Thus, this engineering study begins with the mutagenesis on OAC.

1.2 Construction and expression of OAC variants

OAC is the dimeric α+β barrel (DABB) protein consisting of 101 amino acid residues (**Fig. 5**).[13] Previous crystal structure analysis of OAC complexed with **3b** (PDB ID: 5B09[28], OAC:**3b**) (**Fig. 6**) revealed that this enzyme employs His78 and Tyr72 as the catalytic dyad as well as a 9 Å-long hydrophobic pocket, namely pentyl-binding pocket to lock the acyl moiety of the substrate during the enzyme reaction, and the residues Phe24 and Val59, which are lining the bottom of the pentyl-binding pocket, were shown to accommodate the alkyl moiety of the OAC substrates to regulate the **3b**-forming activities. It can be hypothesized that replacing the F24 and V59 with smaller residues might lead to the expansion of this pentyl-binding pocket for the acceptance of longer alkyl-chain substrates. Thus, F24 was substituted with I/V and V59 was substituted with I/L, respectively. All the constructed expression plasmid were individually transformed into *Escherichia coli* M15 (pREP4) cells and each mutant was expressed as a *N*-terminally glutathione *S*-transferase (GST)-tagged protein, as in the case of wild-type OAC. The F24I and V59I/L mutants were successfully produced as GST-fused proteins in *E. coli*. On the other hand, the OAC F24V mutant was not obtained as a soluble protein. Thus, GST-tag of the F24I and V59I/L mutants was cleaved on a GST affinity column, and GST-tag removal mutants were further purified with the size-exclusion chromatography (HiLoad 16/60 Superdex 200 pg column, GE Healthcare) to be used for enzyme reactions and crystallizations (**Fig. 7**). In addition, in the previous crystal structure analysis of OAC[28], the OAC

F24L, Y27F/L/M/W, and V59M mutants were also constructed to evaluate the role of the pentyl-binding pocket, but their effects on the substrate promiscuity were not evaluated. Hence, the effects of these mutations were also re-evaluated in this study. All the enzyme reaction products **3**, **4**, **6**, and **7** observed were identified by comparing their MS (ESI), MS/MS (ESI), UV spectral data, and HPLC retention times with those of the authentic compounds (**Figs. 21**–**24**).

Fig. 5 Primary sequence comparison of OAC with other DABB proteins. The catalytic residues of OAC and the equivalent residues of AtHS1 (48% amino acid sequence identity) and SP1 (38% amino acid sequence identity) are colored red (numbering according to OAC:**3b**). *Arabidopsis thaliana* AtHS1 (Uniprot code Q9LUV2), Populus tremula SP1 (P0A881).
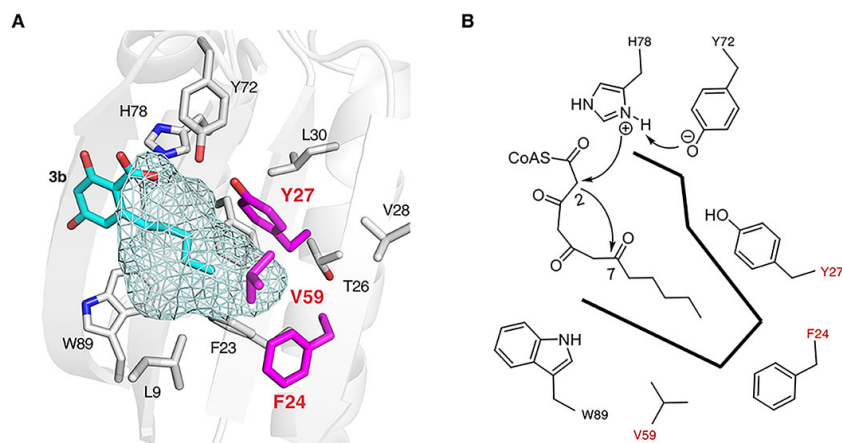

Fig. 6 Close-up views of the pentyl-binding pocket of wild-type OAC complexed with **3b** (OAC:**3b**). (**A**) Residues at the active-site of wild-type OAC. The pentyl-binding pocket is depicted as a light cyan grid surface. Compound **3b** is shown as a cyan stick model. Residues F24, Y27, and V59 are depicted as pink stick models. (**B**) Schematic representation of the active-site cavity of wild-type OAC.
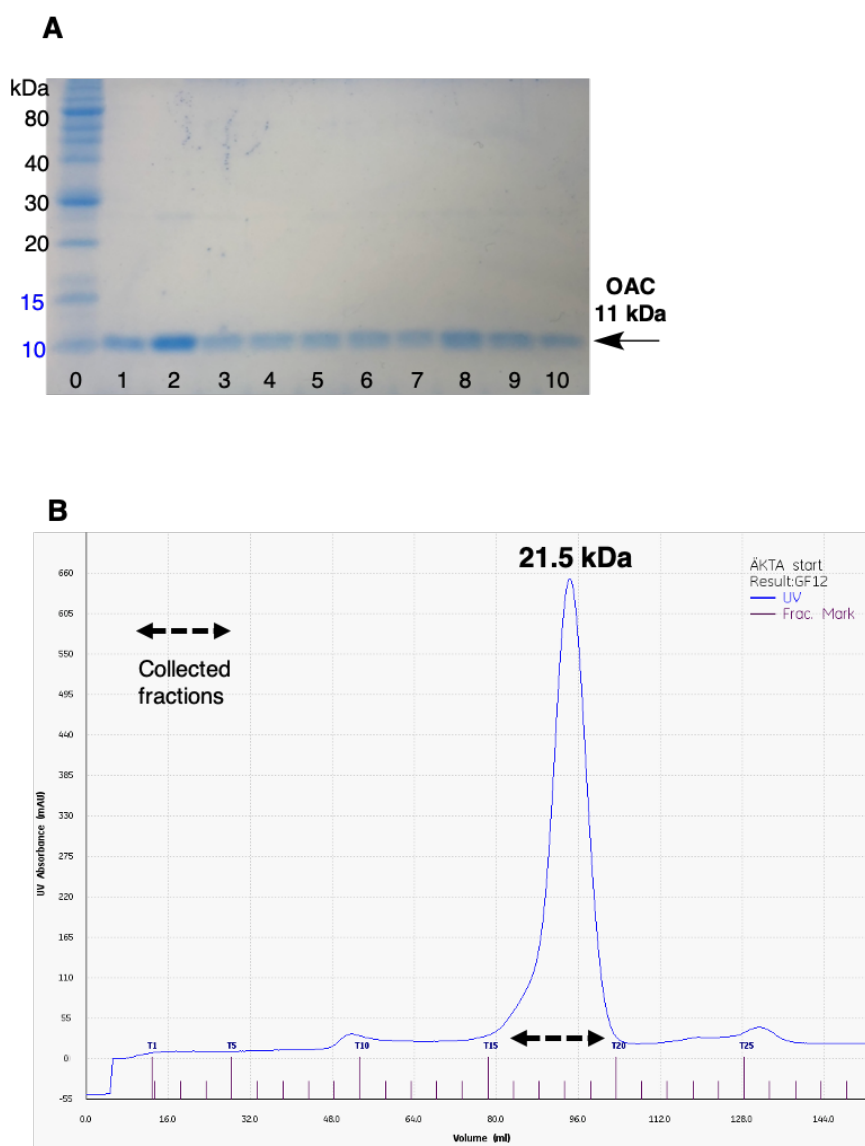
16

Fig. 7 Purification of wild-type OAC and its variants. (**A**) SDS-PAGE of wild-type OAC, OAC F24I, F24L, Y27F, Y27L, Y27M, Y27W, V59I, V59L, and V59M mutants. Lane 0: marker; lane 1: wild-type OAC; lane 2: F24I; lane 3: F24L; lane 4: Y27F; lane 5: Y27L; lane 6: Y27M; lane 7: Y27W; lane 8: V59I; lane 9: V59L; and lane 10: V59M. (**B**) Chromatogram of size-exclusion chromatography.

1.3 Co-incubation assays of OACs and wild-type TKS

The co-incubation assays of wild-type OAC and its mutants were performed with *E. coli* overexpressed TKS using C_5–C_{13} linear aliphatic substrates (**5b**–**f**) (**Fig. 8**) and malonyl-CoA to assess the outcome of the mutations on their **3b**-forming activities, since the pentyltetra-β-ketide-CoA (**8b**) is not directly available due to its

instability. All the OAC mutants retained their **3b**-forming activities in the co-incubation assay (**Fig. 9**). The OAC Y27F mutant showed highest **3b**-forming activity with 1.38 times increase when compared to wild-type OAC, which is similar to previously reported results.[27] In cases of the OAC Y27L/M/W and V59M mutants, the activities were decreased to less than 56%. The **3b**-forming activity of OAC V59I mutant was 1.17 times higer than that of the wild type OAC, whereas OAC F24I/L and V59L mutants showed decreased activities in a lesser degree as compare with that of wild-type OAC.
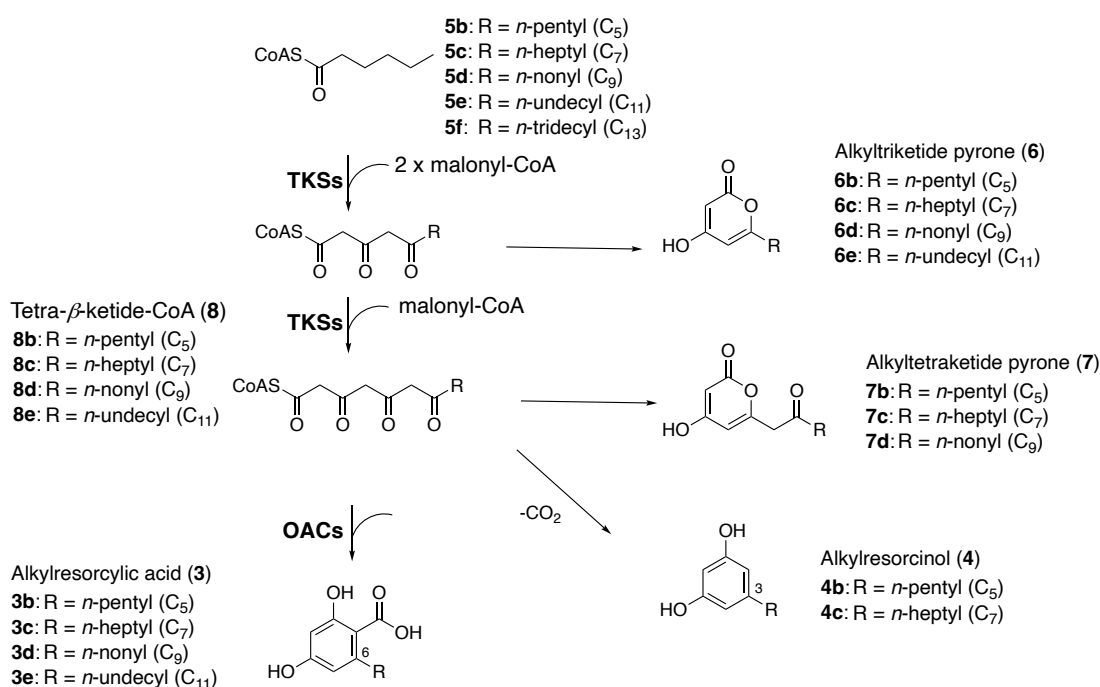

Fig. 8 Alkylresorcylic acids, alkylresorcinols, and alkyltri- and alkyltetraketide pyrones detected in the reaction mixtures of OACs and TKSs using linear fatty acyl-CoAs and malonyl-CoA as starter substrates.

Presumably, the Y27F substitution increased both the hydrophobicity of the pentyl-binding pocket and the electrostatic interaction between the catalytic residues Y72 and H78, which lead to the increase of its **3b**-forming activity. In the case of the Y27L/M/W and V59M mutants, the substitutions could somehow prevent the access of the pentyl moiety of the substrate, thereby showing a decrease in their **3b**-forming activities. The V59I substitution near to Y27 likely alter the hydrophobicity of the active-site cavity without causing a significant conformational change of the pentyl-

binding pocket, which could lead to slight increase of the **3b**-forming activity of this V59I mutant. On the other hand, although the small-to-large V59L substitution increased the hydrophobicity, this substitution most likely caused the narrowing of the pentyl-binding pocket. Hence, its **3b**-forming activity was decreased. On the other hand, the large-to-small F24I/L substitutions might expand the pentyl-binding pocket of both the mutants, which would reduce the binding affinity to the pentyl moiety of **5b**, to show a decrease in their **3b**-forming activities.
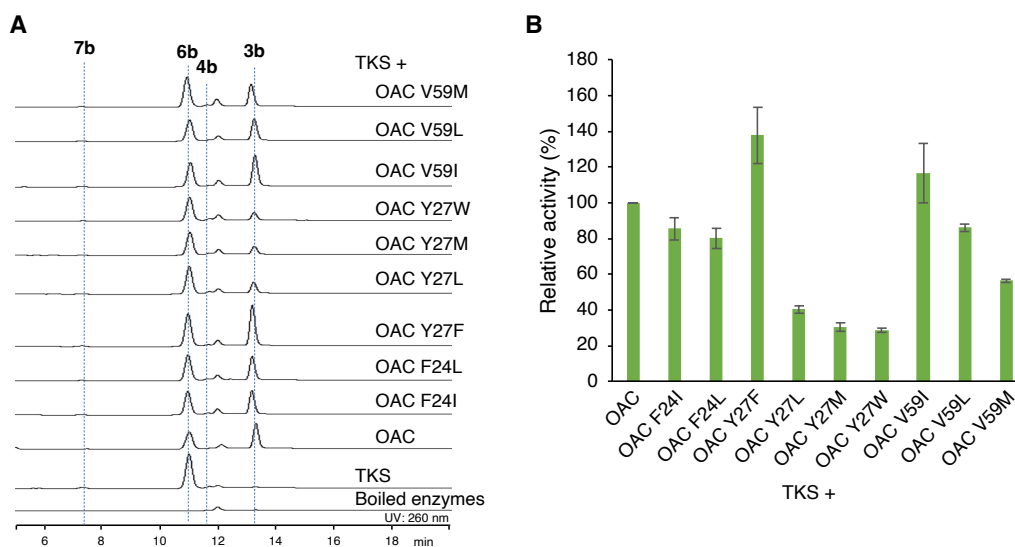

Fig. 9 HPLC profiles of OACs and wild-type TKS using hexanoyl-CoA (**5b**) and malonyl-CoA as substrates. (**A**) HPLC chromatogram of OACs and TKS enzyme reaction products and (**B**) relative activities of OACs for **3b** formation in co-incubation with wild-type TKS. The activities are percentages of **3b** production relative to that of wild-type OAC. Data are mean ± SD; $n = 3$ independent samples under the same reaction conditions. The boiled TKS and OAC enzymes were used as controls.

TKS was previously reported to accepts heptanoyl-CoA (**5c**) as the starter substrate to condense two molecules of malonyl-CoA.[13] In addition, current study also demonstrated that TKS is able to accept **5c** to produce **8c**.[21] This was confirmed by the detection of **7c** in the enzyme reaction product. As such, I proceeded to evaluate the **3c**-forming activity of the wild-type OAC and its mutant enzymes in the co-incubation assays with TKS (**Fig. 10**). Interestingly, wild-type OAC showed slight **3c**-forming activity, which has been never reported in the literature. All the mutants also retained their **3c**-forming activities ranging from 11% to 106% relative to that of the wild type.
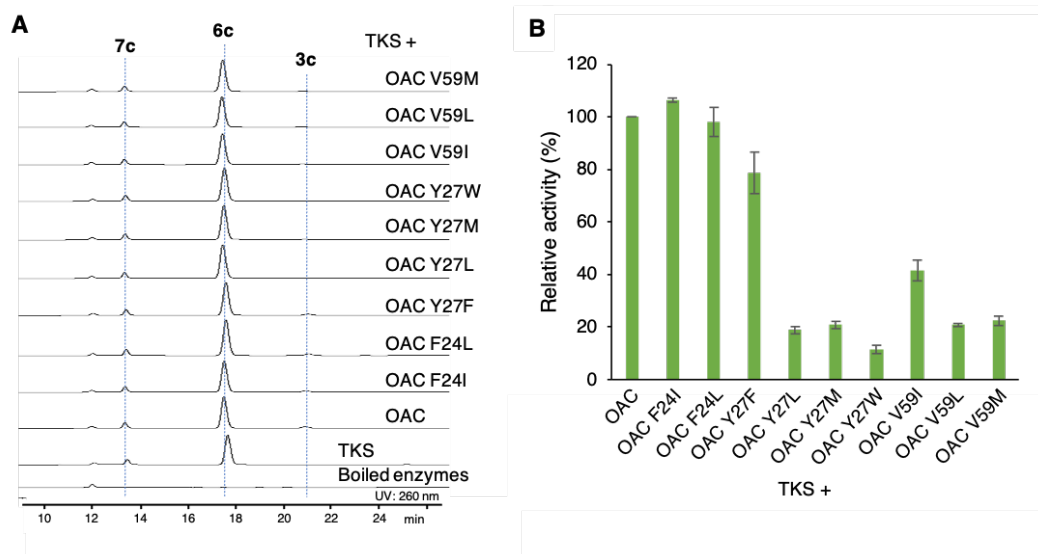
Fig. 10 HPLC profiles of OACs and wild-type TKS using heptanoyl-CoA (**5c**) and malonyl-CoA as substrates. (**A**) HPLC chromatogram of OACs and TKS enzyme reaction products and (**B**) relative activities of OACs for **3c** formation in co-incubation with wild-type TKS. The activities are percentages of **3c** production relative to that of wild-type OAC. Data are mean $\pm$ SD; $n = 3$ independent samples under the same reaction conditions. The boiled TKS and OAC enzymes were used as controls.

However, further investigation of the ability of the wild-type OAC and its variants in the presence of TKS indicated that 2,4-dihydroxy-6-heptylbenzoic acid (**3d**) and 2,4-dihydroxy-6-undecylbenzoic acid (**3e**) was not produced in any of the reactions using decanoyl-CoA (**5d**) and lauroyl-CoA (**5e**) as the starter substrates (**Fig. 11**). This suggests a possibility that the performed single substitutions of OAC are not enough to expand the substrate promiscuity of OAC for longer alkyl moiety of the substrate. However, simultaneously, the sole incubation assay of TKS also revealed that it was capable of accepting **5d** and **5e** as the starter substrates to form the corresponding **6**, but **4** and **7** were no longer detected in the reaction mixture (**Fig. 11**). Thus, other possibility was that the TKS reaction may be terminated after only two condensations of malonyl-CoA to the starter substates, **5d** and **5e**.
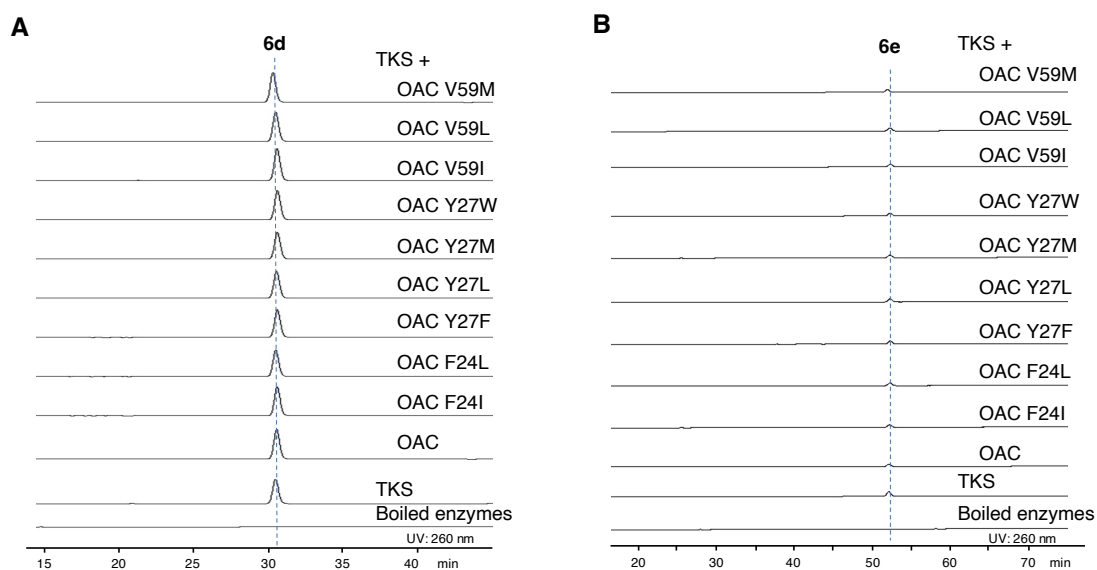
Fig. 11 HPLC profiles of OACs and wild-type TKS using (**A**) decanoyl-CoA (**5d**) and (**B**) dodecanoyl-CoA (**5e**), and malonyl-CoA as substrates. (**A** and **B**) HPLC chromatograms of OACs and TKS enzyme reaction products.

1.4 Crystal structure analyses of OAC F24I

The aforementioned results suggested that either further expansion of the OAC or TKS substrate promiscuity may be required to generate longer alkyl-side chain **3b**-analogs. In order to confirm the requirement of further engineering of OAC, co-crystallization of the OAC F24I mutant with the most potent **3c**-forming activity and longer alkyl-chain **3b**-analogs were performed (**Figs. 12, 13, 15A, and 15B**). The crystal structure of OAC F24I mutant with **3c** indicated that the F24I substitution significantly extended its pentyl-binding pocket to accommodate heptyl-moiety of **3c** (**Fig. 15C**). Notably, the crystal structure also suggested that the mutant enzyme retain the space between the top of the heptyl-moiety of **3c** and the bottom of its pentyl-binding pocket, suggesting that the mutant enzyme has an ability to accept the longer acyl-moiety substrate than heptyl-*β*-tetraketide-CoA. Indeed, this mutant adopted to accommodate not only **3b** and **3c**, but also **3d** in the active site cavity by expanding the pentyl-binding pocket toward W42 located at the protein surface as shown in the in the crystal structures of the OAC F24I mutant complexed with **3d** (OAC-F24I:**3d**) (**Figs. 14**, **15D**, and **Table 3** in the Materials and methods section). This crystal structure also indicated the slight conformational changes of residues such as L9, Y27,

and W42, as well as a nearly 120˚ rotation of the V59 side-chain, as compared with those of wild-type OAC:**3b** (**Fig. 15E**). As a result, the pentyl-binding pocket of the OAC F24I mutant was extended to a 12.3 Å long, which is enough to accommodate the *n*-nonyl moiety of **3d**, as compared to the 9.0 Å long wild-type pocket in the crystal structure, suggesting that OAC-F24I:**3d** thereby accommodated **3d** in its active site cavity (**Figs. 14 and 15D**). From a point of view of the crystal structure, the OAC F24I mutant should accept nonyltetra-β-ketide-CoA (**8d**) as the substrate to generate **3d**. In addition, presumably, the F24I/L mutants decreased the **3b**-forming activities, due to the reduced binding affinity to the pentyl moiety of **8b**. However, the results obtained from the crystal structure is not consistent with the previous results obtained from the in *vitro* enzyme reaction, where no production of **3d** was observed (**Fig. 11A**).
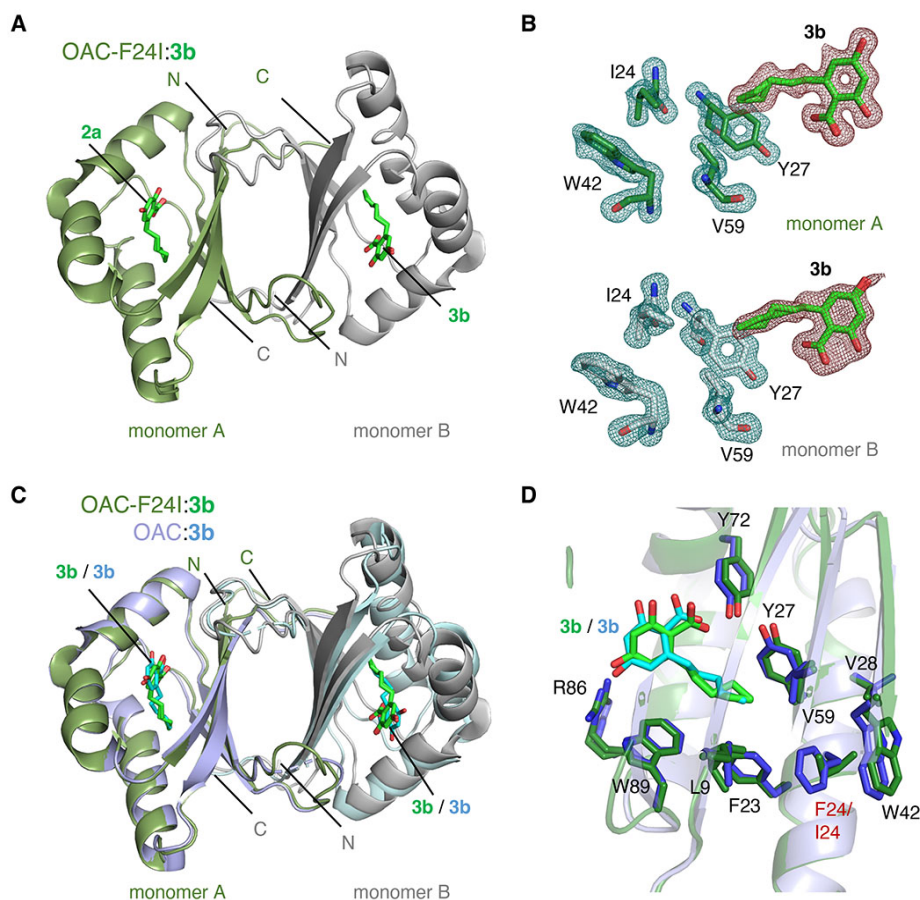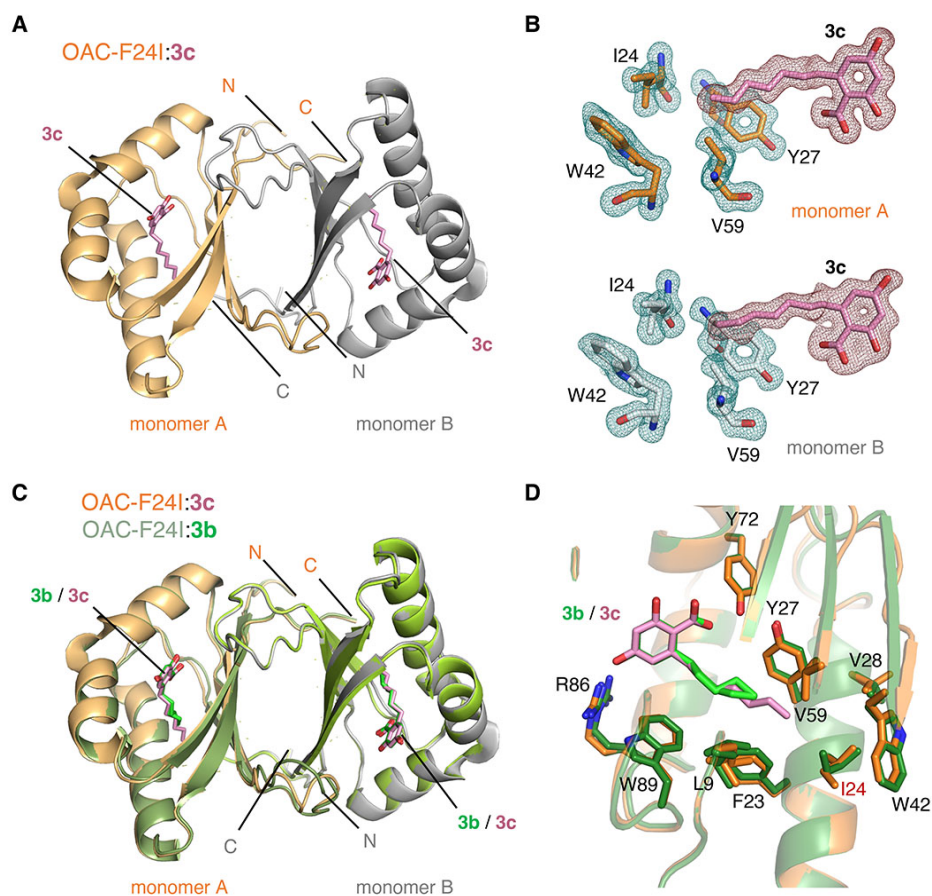
Fig. 12 Crystal structure of OAC F24I complexed with **3b** (OAC-F24I:**3b**; PDB ID: 7W6D). (**A**) Overall structure of the OAC-F24I:**3b** complex. (**B**) OMIT electron density maps (mF$_o$−DF$_c$) contoured at 3.0σ around **3b** (red mesh) and 4.0σ around the I24, Y27, W42, and V59 residues of OAC-F24I:**3b** (blue mesh) in monomers A and B. (**C**) Superimposition of the overall structures of OAC-F24I:**3b** and wild-type OAC:**3b** (PDB ID: 5B09[21]). (**D**) Close-up view of the active site cavities of OAC-F24I:**3b** and OAC:**3b**. Monomers A and B of OAC-F24I:**3b** and those of OAC:**3b** are shown in forest green, grey, blue, and cyan, respectively. Compound **3b** in OAC-F24I:**3b** and OAC:**3b** is indicated by green and cyan stick models, respectively. Monomers A and B of OAC-F24I:**3b** showed high structural similarity with a Root Mean Square Deviation (RMSD) value of 0.411 Å for the Cα-atoms. OAC-F24I:**3b** and OAC:**3b** showed similar structures with an RMSD value of 1.074 Å for the Cα-atoms.
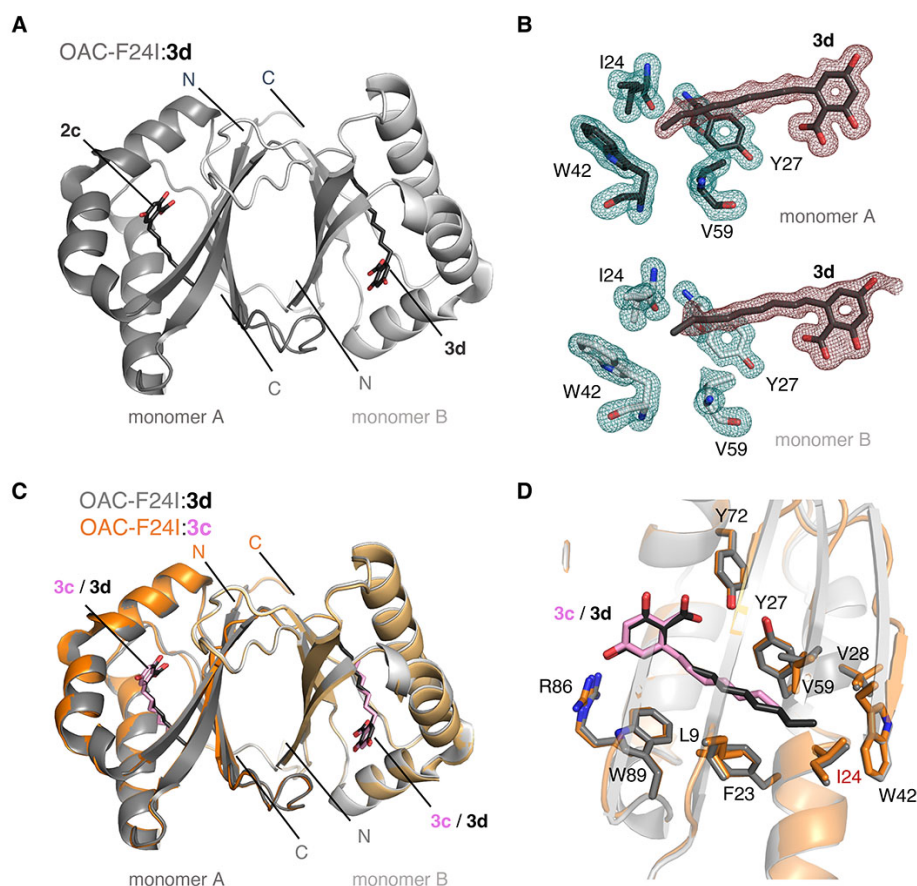
Fig. 13 Crystal structure of OAC F24I complexed with **3c** (OAC-F24I:**3c**; PDB ID: 7W6E). (**A**) Overall structure of the OAC-F24I:**3c** complex. (**B**) OMIT electron density maps (mF$_o$−DF$_c$) contoured at 3.0σ around **3c** (red mesh) and 4.0σ around the I24, Y27, W42, and V59 residues of OAC-F24I:**3c** (blue mesh) in monomers A and B. (**C**) Superimposition of the overall structures of OAC-F24I:**3c** and OAC-F24I:**3b**. (**D**) Close-up view of the active site cavities of OAC-F24I:**3c** and OAC-F24I:**3b**. Monomers A and B of OAC-F24I:**3c** and those of OAC:**3b** are shown in orange, grey, forest green, and limon, respectively. Compounds **3c** in OAC-F24I:**3c** and **3b** in OAC-F24I:**3b** are indicated by pink and green stick models, respectively. Monomers A and B of OAC-F24I:**3c** showed high structural similarity with an RMSD value of 0.394 Å for the Cα-atoms. No significant conformational changes of the overall structures between OAC-F24I:**3c** and OAC-F24I:**3b** were observed (Cα RMSD = 0.394 Å).

Fig. 14 Crystal structure of OAC F24I complexed with **3d** (OAC-F24I:**3d**; PDB ID: 7W6F). (**A**) Overall structure of the OAC-F24I:**3d** complex. (**B**) OMIT electron density map (mF$_o$−DF$_c$) contoured at 3.0σ around **3d** (red mesh) and 4.0σ around the I24, Y27, W42, and V59 residues of OAC-F24I:**3d** (blue mesh) in monomers A and B. (**C**) Superimposition of overall structures of OAC-F24I:**3d** and OAC-F24I:**3c**. (**D**) Close-up view of the active site cavities of OAC-F24I:**3d** and OAC-F24I:**3c**. Monomers A and B of OAC-F24I:**3d** and those of OAC-F24I:**3c** are shown in dark grey, grey, and orange, respectively. Compounds **3d** in OAC-F24I:**3d** and **3c** in OAC-F24I:**3c** are indicated by black and pink stick models, respectively. Monomers A and B of OAC-F24I:**3d** showed high structural similarity with an RMSD value of 0.412 Å for the Cα-atoms. No significant conformational changes of the overall structures between OAC-F24I:**3d** and OAC-F24I:**3c** were observed (Cα RMSD = 0.193 Å).
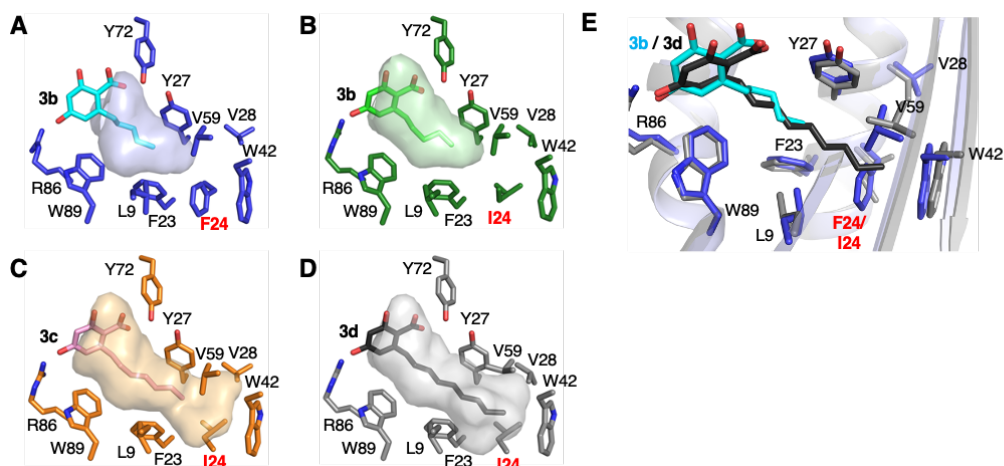
Fig. 15 The active site architectures of (**A**) OAC:**3b**, (**B**) OAC-F24I:**3b**, (**C**) OAC-F24I:**3c**, and (**D**) OAC-F24I:**3d** and (**E**) the comparison of the active site residues of OAC:**3b** and OAC-F24I:**3d**. The active site cavities are represented by surface models. The **3b** molecules bound to OAC:**3b** and OAC-F24I:**3b** are shown as cyan and green stick models, respectively. Molecules **3c** and **3d** bound to OAC-F24I:**3c** and OAC-F24I:**3d** are indicated as pink and black stick models, respectively. The F24 and I24 residues are highlighted in red bold fonts.

1.5 Construction and expression of TKS and its L190G mutant

The crystal structure analysis of the OAC F24I mutant thus suggested that catalytic activity of TKS rather than OAC (or OAC F24I) is insufficient to yield **8**, especially more than *n*-heptyl moiety. So far, various type III PKS has been reported, and some of them may be available for the formation of longer alkyl **3b**-analogs instead of TKS. In particular, PKS-A from *Arabidopsis thaliana* reportedly produced C_6-C_{20} acyltetraketide pyrones associated with corresponding tetra-β-ketide-CoA productions.[29] Furthermore, Page *et al* reported that no protein-protein interaction between OAC and TKS is required for the formation of **3b** during the enzyme reaction.[14] Thus, PKS-A was expressed in *E. coli*, and used for the co-incubation assay of wild type OAC and its F24I mutant using *A. thaliana* PKS-A instead of TKS (**Fig. 16**). However, the production of not only **3b**, but also **3b**-analogs were detected in the reaction products, suggesting that *A. thaliana* PKS-A is a type III PKS that produces pyrones before releasing the corresponding acyltetraketide-CoAs from the enzyme.

This would be the reason why the alternative use of *A. thaliana* PKS-A in the co-incubation assay showed no efficacy for the formation of acylresorcylic acid.
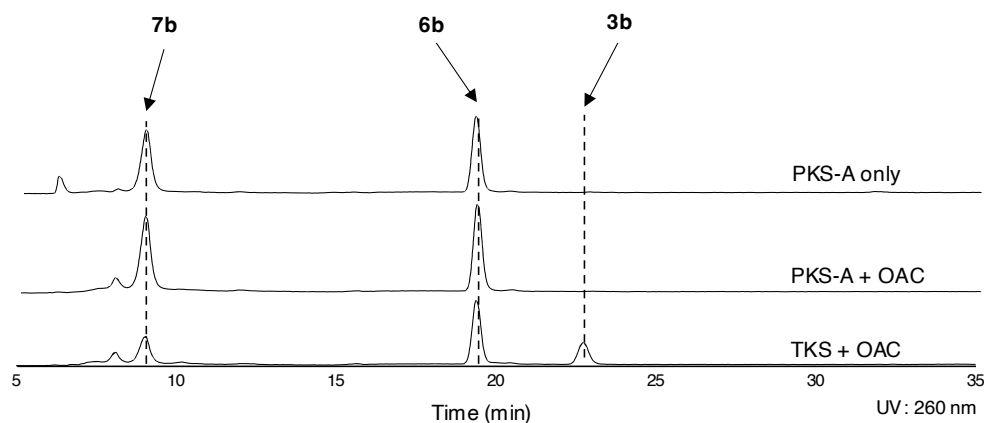

Fig. 16 HPLC elution profiles of PKS-A and OAC using **5b** and malonyl-CoA as substrates.

Thus, in the absence of other type III PKSs that have been identified to generate tetra-β-ketide-CoAs with longer acyl moiety than C_6, I shifted my focus on the engineering of TKS. Previous study showed that the homologous residue at L190 of TKS in *Aloe arborescens* octaketide synthase (OKS) (**Fig. 17**) has also been found to control the acyl-chain length specificity of the starter substrates.[30] The small-to-large amino acid substitution in the site-directed mutagenesis of OKS showed this mutant enzyme accepts only shorter fatty acyl CoAs (up to the C_{12} chain length) as a starter substrate instead of long chain aliphatic CoAs (up to the C_{20} chain length) in the wild-type OKS. This homologous residue L190 in TKS thus might be a suitable candidate for further mutagenesis. Indeed, the crystal structure of wild-type TKS complexed with the CoA-SH (PDB ID: 6GW3, TKS:CoA-SH) solved by the other group indicated that this L190 residue lies in the main active site cavity of TKS and is fully buried inside the vertical pocket behind the L190 and M187 residues.[31] Accordingly, the L190 residue in TKS was substituted with the least bulky glycine, to fully open the gate of the vertical pocket behind the residues L190 and M187.
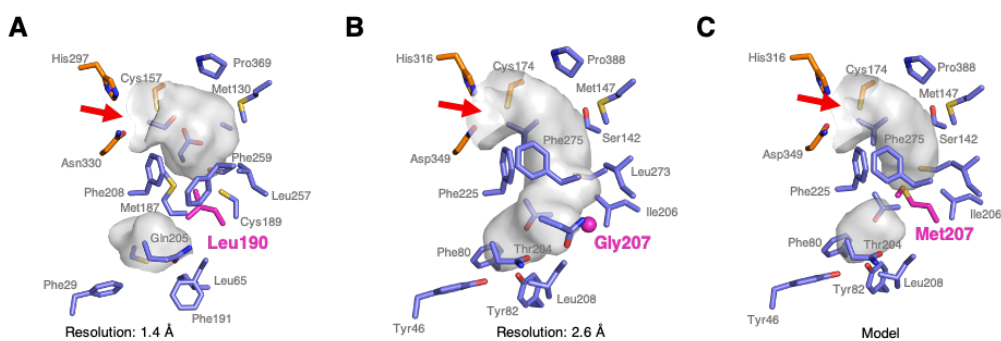
Fig. 17 Active site architectures of (**A**) TKS and (**B**) OKS, and (**C**) model structure of OKS. The catalytic triad is depicted as orange sticks. The homologous residues at L190 of TKS, G207 at OKS, and M207 at OKS model are shown as pink stick models.

1.6   Crystal structure of TKS L190G

As a result, the crystal structure of the TKS L190G mutant complexed with **5e** (TKS-L190G:**5e**) was solved at 2.10 Å resolution (**Fig. 18** and **Table 3** in the Materials and methods section). A comparison of TKS-L190G:**5e** and TKS:CoA-SH showed that the large-to-small L190 residue indeed dramatically elongated the active site cavity by combining it with the vertical hidden pocket observed in the wild-type TKS crystal structure. The cavity volume was estimated to be 471 Å^3, which would have enough capacity to accommodate longer acyl-CoA chains than the wild-type TKS with the active site cavity of only 417 Å^3. It is quite remarkable that this single amino acid replacement caused significant increase in the active-site cavity volume. As mentioned earlier, the large-to-small G210M substitution in OKS resulted in reducing the enzyme functionality.[30] Thus, the opposite large-to-small L190G substitution in TKS might result in the change of enzyme promiscuity of this mutant enzyme.
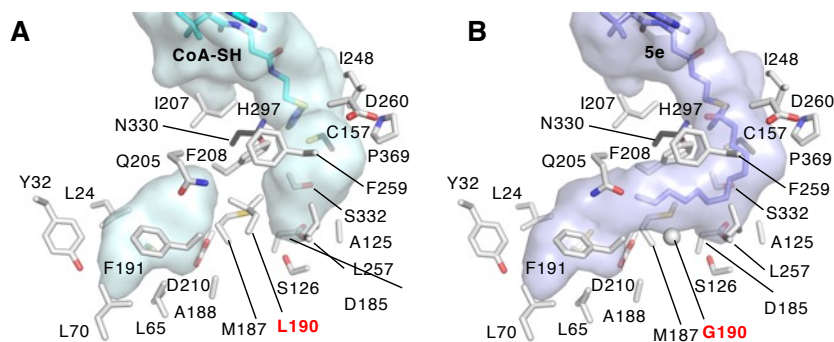
Fig. 18 Comparison of active site architectures of (**A**) TKS:CoA-SH and (**B**) TKS-L190G:**5e**. The active site cavities are represented by surface models. CoA-SH and **5b** molecules bound to TKS:CoA-SH and TKS-L190G:**5e** are shown as cyan and blue stick models, respectively. Residues L190 and G190 are both highlighted in red bold fonts.

1.7   Co-incubation assays of OACs and TKS L190G mutant

The incubations of the TKS L190G mutant alone in the presence of **5b-e** as starter substrates and malonyl-CoA indicated that the L190G substitution at least conferred the ability to produce up to **8d**, as confirmed by the production of **7d**. To evaluate the **3b**-forming activities, OACs were co-incubated with the resultant TKS L190G mutant. As a result, except for the OAC Y27F mutant, the **3b** productions of wild-type OAC and its variants were more or less increased by almost the same degree when compared with those from the set of OAC enzymes and wild-type TKS (**Figs. 9**, **19A**, and **B**). Additionally, when the TKS L190G mutant was used, all the OAC enzymes, especially the wild-type OAC and its F24I/L mutants, dramatically increased the **3c** production, as compared with that from the set of OAC enzymes and wild-type TKS in the presence of **5c** and malonyl-CoA (**Figs. 19C** and **D**). It is noteworthy that when **5d** was used as the starter substrate, the wild-type OAC naturally possessed the **3d**-forming activity, as verified from the co-incubation assay of the OAC enzymes with the TKS L190G mutant (**Figs. 20A** and **D**), which has never been reported in the previous study. In addition, this activity was also enhanced by about 10- and 5.5-folds by the F24I/L substitutions, respectively. This could be explained by the expansion of the pentyl-binding pocket observed in OAC-F24I:**3d** (**Figs. 14** and **15D**). Remarkably, the LC-MS analyses showed that only the F24I/L substitutions of OAC conferred the ability to produce **3e** (**Fig. 20B**). However, I could no longer detect the production of
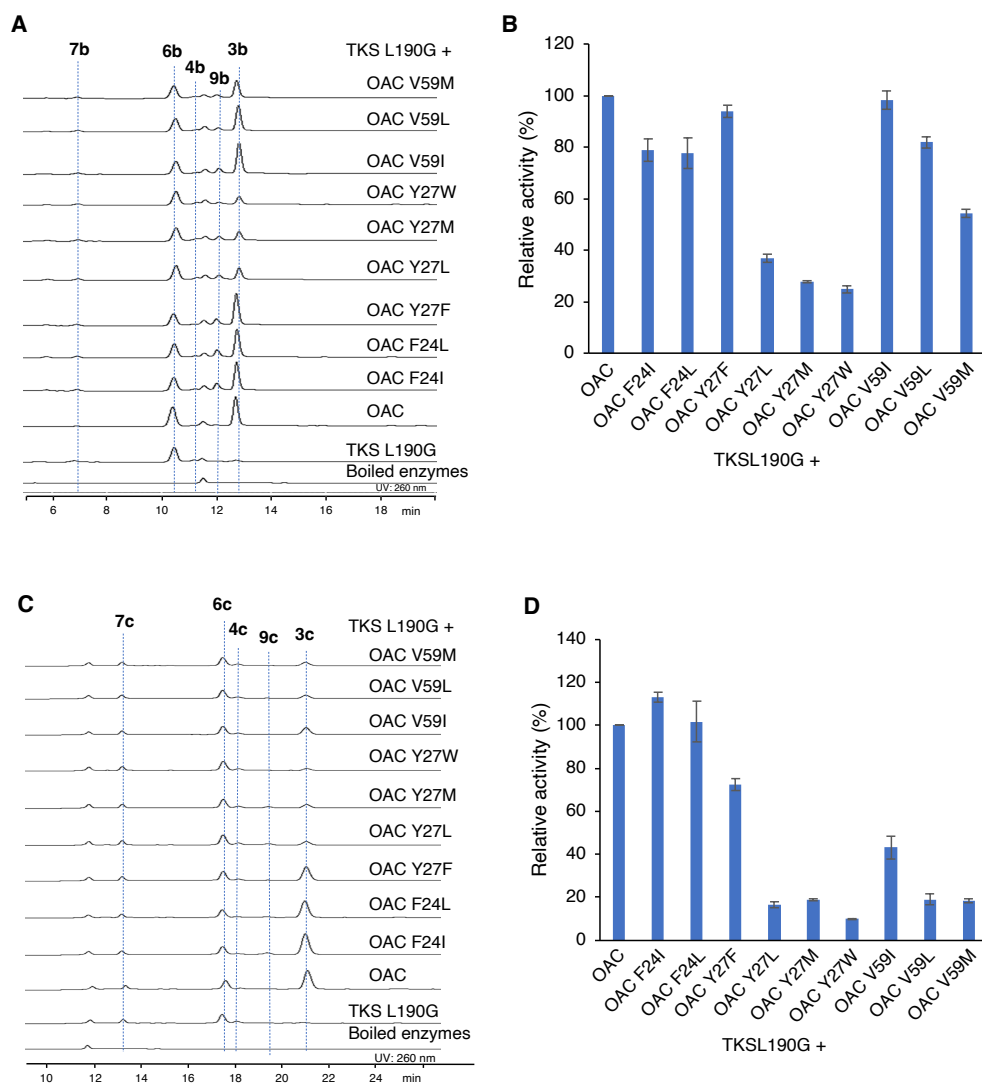
Fig. 19 HPLC profiles of OACs and TKS L190G using (**A** and **B**) hexanoyl-CoA (**5b**) and (**C** and **D**) octanoyl-CoA (**5c**), and malonyl-CoA as substrates. (**A** and **C**) HPLC chromatogram of OACs and TKS L190G enzyme reaction products and (**B** and **D**) relative activities of OACs for (**B**) **3b** and (**D**) **3c** formation in co-incubation with TKS L190G. The activities are percentages of corresponding **3** production relative to that of wild-type OAC. Data are mean ± SD; *n* = 3 independent samples under the same reaction conditions. The boiled TKS L190G and OAC enzymes were used as controls.
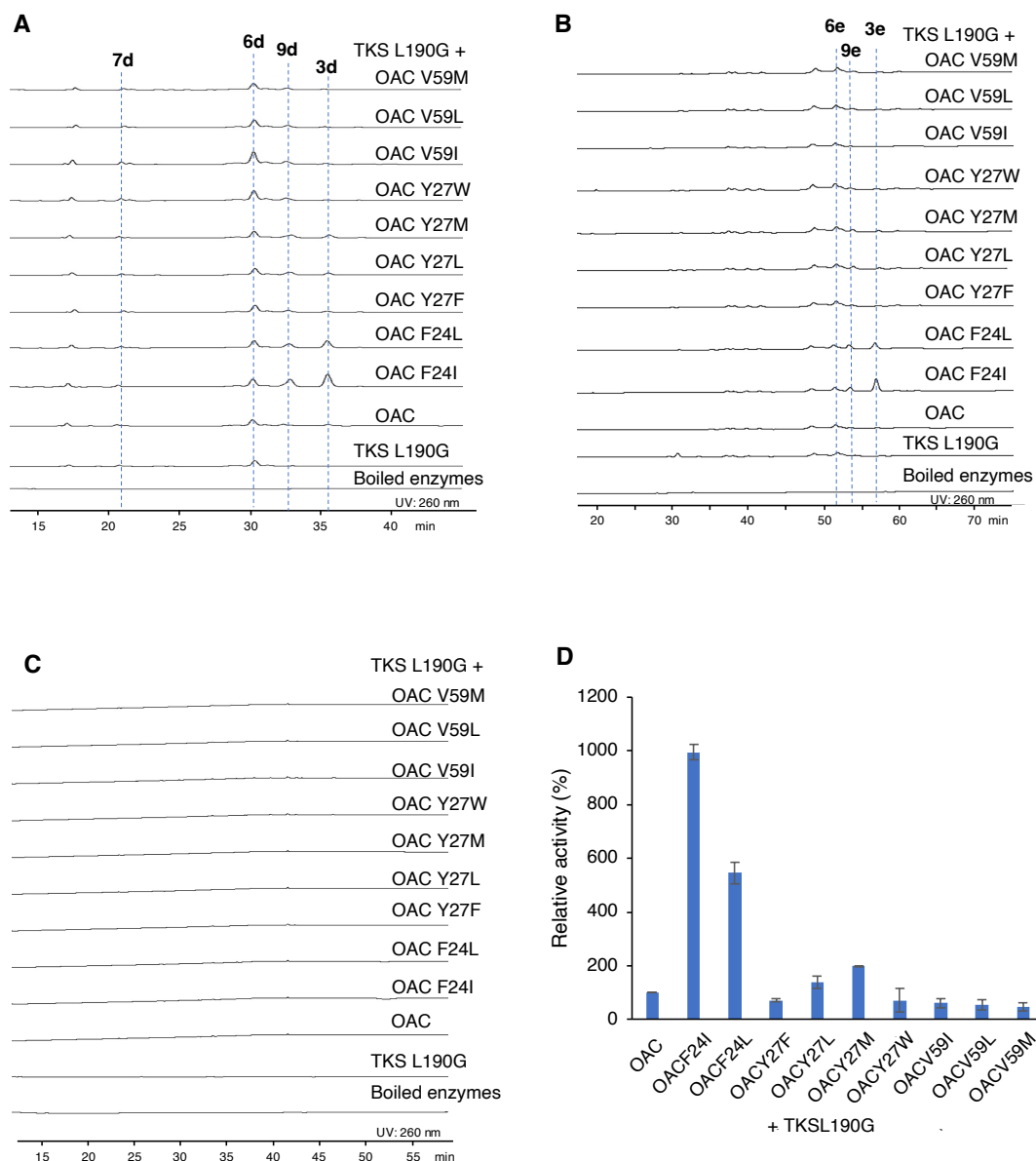
Fig. 20 HPLC profiles of OACs and TKS L190G using (**A**) decanoyl-CoA (**5d**), (**B**) dodecanoyl-CoA (**5e**), (**C**) tetradecanoyl-CoA (**5f**), and malonyl-CoA as substrates. (**A, B** and **C**) HPLC chromatograms of OACs and TKS L190G enzyme reaction products and (**D**) relative activities of OACs for **3d** formation in co-incubation with TKS L190G. The activities are percentages of **3d** production relative to that of wild-type OAC. Data are mean ± SD; $n = 3$ independent samples under the same reaction conditions. The boiled TKS L190G and OAC enzymes were used as controls.
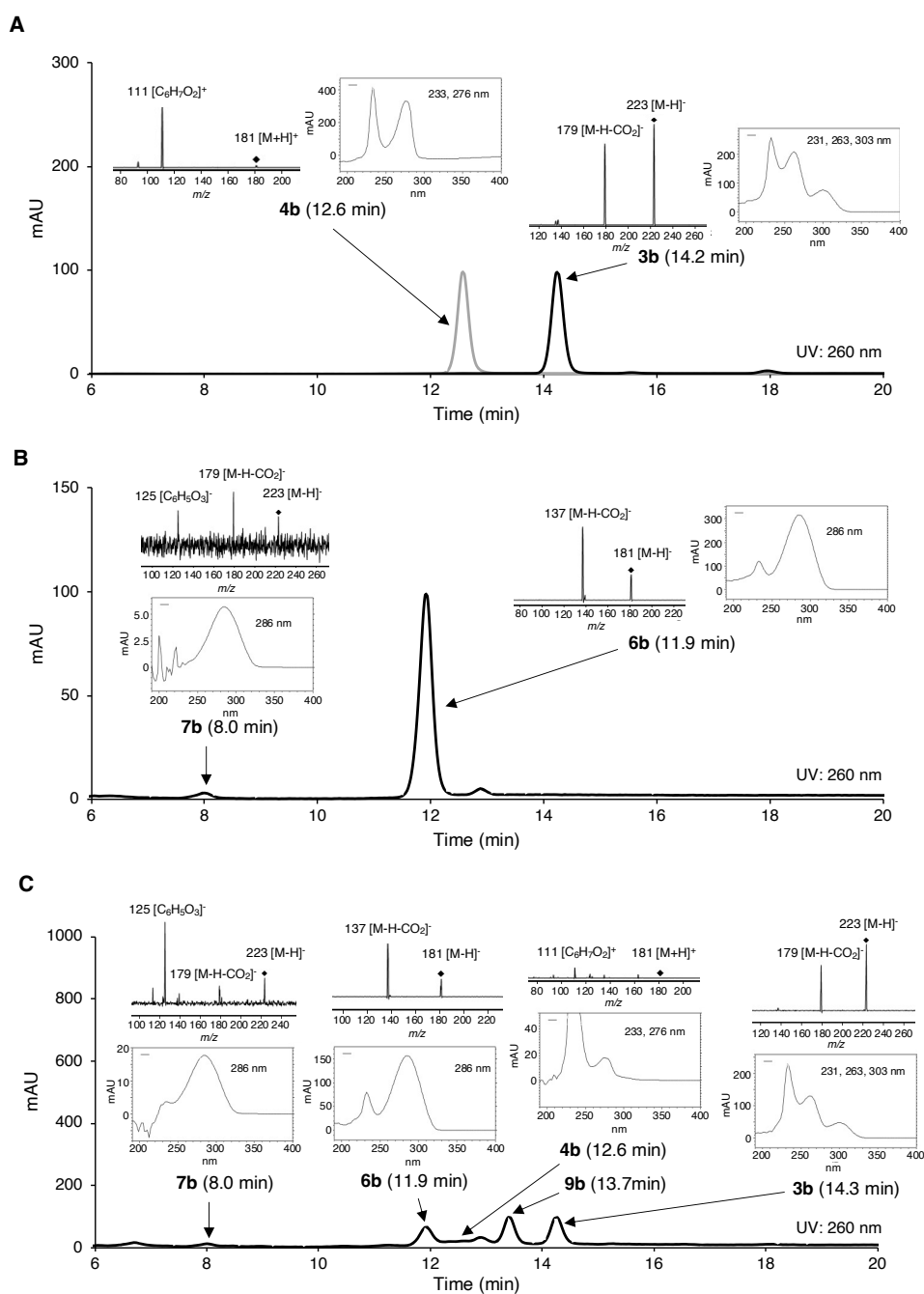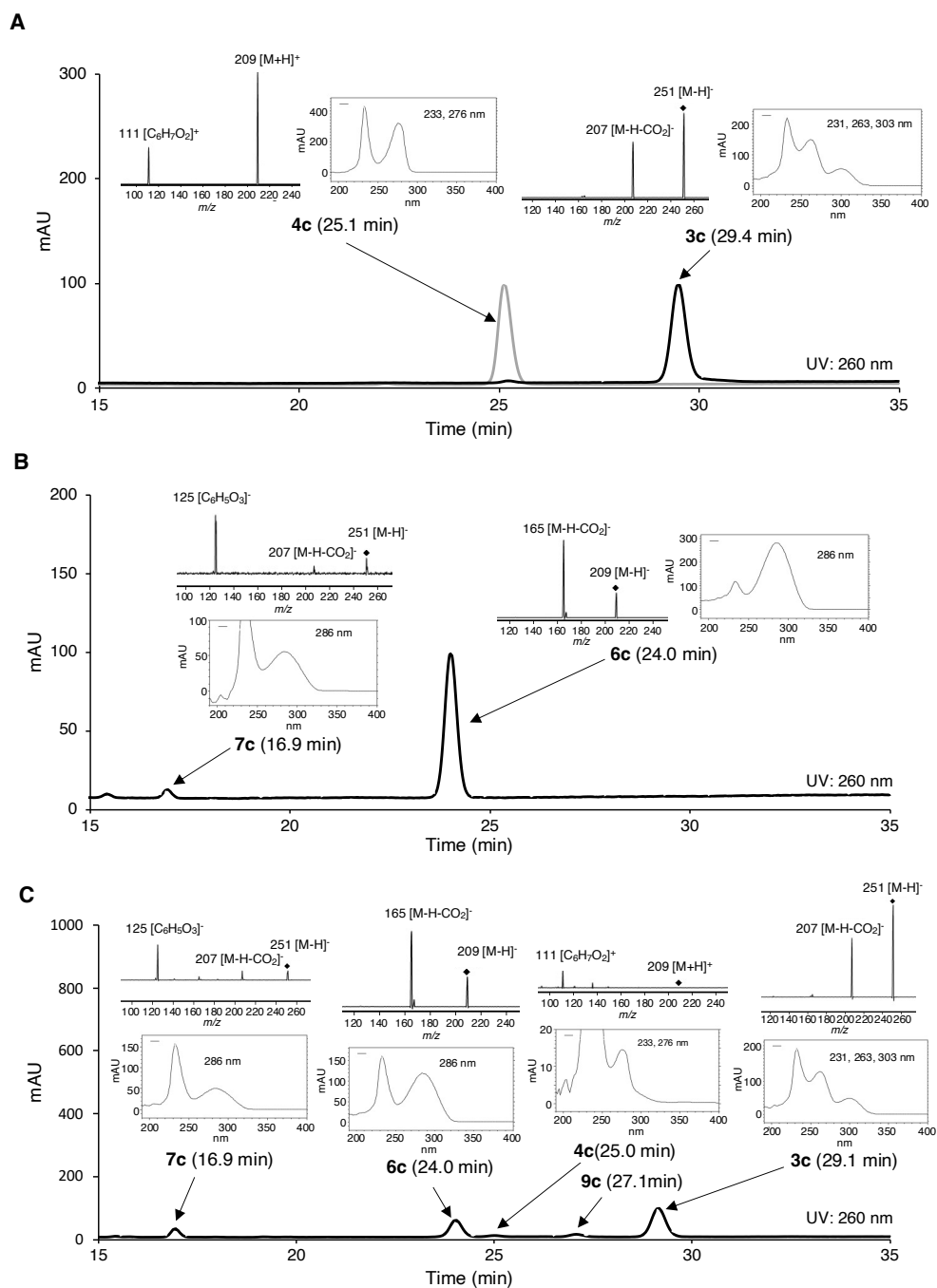
Fig. 21 MS (ESI), MS/MS (ESI), UV spectra and HPLC retention times of olivetolic acid (**3b**), pentyltetraketide pyrone (**6b**), pentyltriketide pyrone (**7b**), and olivetol (**4b**). (**A**) Spectra and retention times of authentic samples of **3b** and **4b**. (**B**) Spectra and retention times of **6b** and **7b** produced by PKS-A using hexanoyl-CoA (**5b**) and malonyl-CoA as substrates. (**C**) Spectra and retention times of **3b**, **6b**, **7b**, and **4b** from co-incubations of the OAC F24I and TKS L190G mutants using **5b** and malonyl-CoA as substrates. Negative ionization was used in MS (ESI) and MS/MS (ESI) for **3b**, **6b**, and **7b**. Positive ionization was used in MS (ESI) and MS/MS (ESI) for **4b**. UV spectra were obtained at 200-400 nm. The MS/MS (ESI) fragmentation analysis of **3b**

indicated an ion fragment peak of *m/z* 179 [M - H - CO$_2$]$^-$ from the pseudo-molecular ion at *m/z* 223 [M - H]$^-$, while the analysis of **7b** indicated an ion fragment peak of *m/z* 125 [C$_6$H$_5$O$_3$]$^-$, corresponding to the α-pyrone from the pseudo-molecular ion at *m/z* 223 [M - H]$^-$, in addition to the ion fragment peak of *m/z* 179 [M - H - CO$_2$]$^-$. LC-MS (ESI) and MS/MS (ESI) condition; see Material and methods. LC-MS (ESI) and MS/MS (ESI) of **9b** were shown in **Fig. 27**.

Fig. 22 MS (ESI), MS/MS (ESI), UV spectra and HPLC retention times of phorolic acid (**3c**), heptyltetraketide pyrone (**6c**), heptyltriketide pyrone (**7c**), and spherophorol (**4c**). (**A**) Spectra and retention times of authentic samples of **3c** and **4c**. (**B**) Spectra and retention times of **6c** and **7c** produced by PKS-A using octanoyl-CoA (**5c**) and malonyl-CoA as substrates. (**C**) Spectra and retention times of **3c**, **6c**, **7c**, and **4c** from co-incubations of the OAC F24I and TKS L190G mutants using **5c** and malonyl-CoA as substrates. Negative ionization was used in MS (ESI) and MS/MS (ESI) for **3c**, **6c**, and **7c**. Positive ionization was used in MS (ESI) and MS/MS (ESI) for **4c**. UV spectra were obtained at 200-400 nm. The MS/MS (ESI) fragmentation analysis of **3c** indicated an ion fragment peak of m/z 207 [M - H - CO$_2$]$^-$ from the pseudo-molecular ion at m/z 251 [M - H]$^-$, while the analysis of **7c** indicated an ion

fragment peak of m/z 125 [$C_6H_5O_3$]$^-$, corresponding to the α-pyrone from the pseudo-molecular ion at m/z 251 [M - H]$^-$, in addition to the ion fragment peak of m/z 207 [M - H - CO_2]$^-$. LC-MS (ESI) and MS/MS (ESI) condition; see Material and Methods. LC-MS (ESI) and MS/MS (ESI) of **9c** were shown in **Fig. 28**.
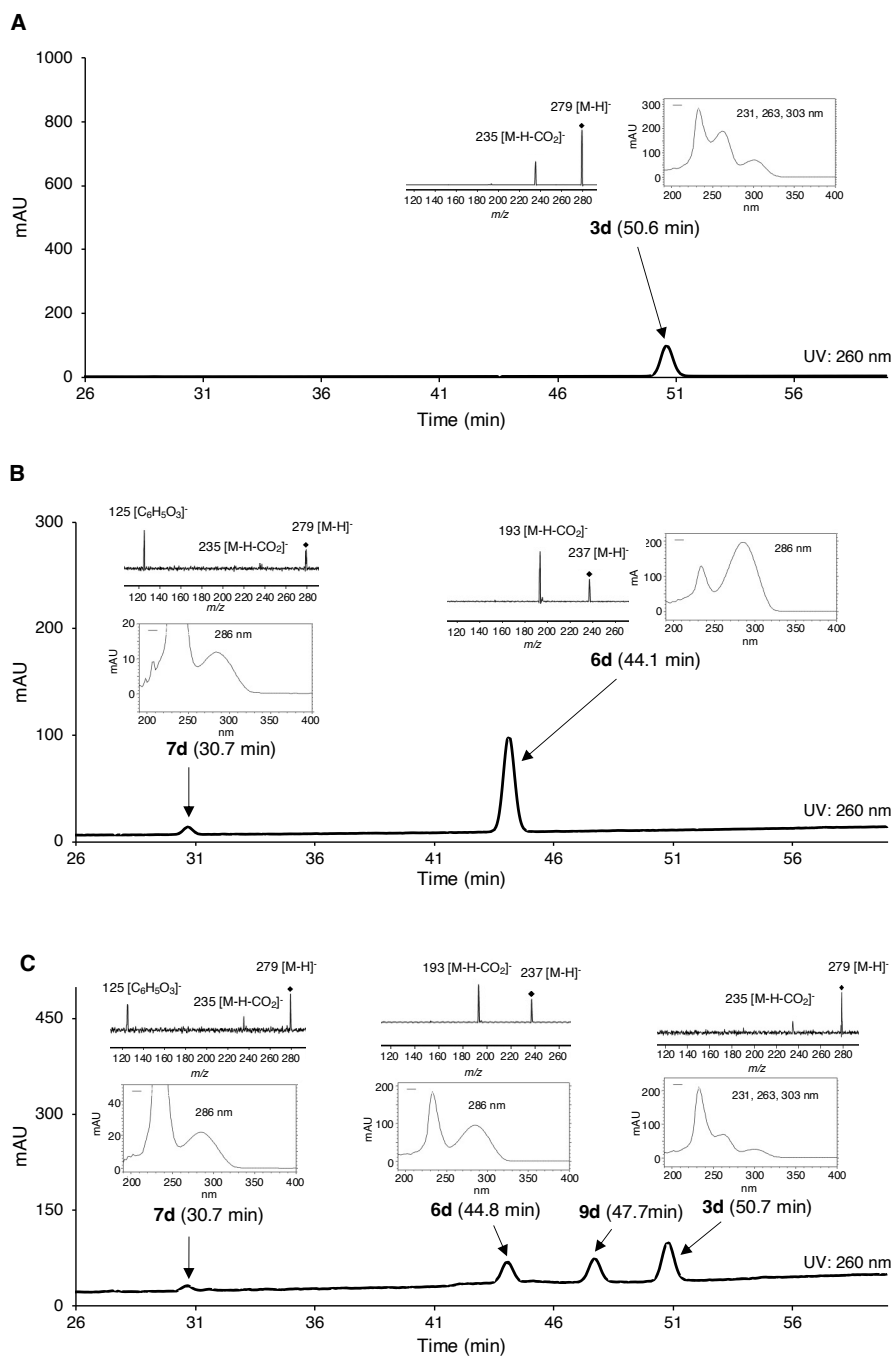
Fig. 23 MS (ESI), MS/MS (ESI), UV spectra and HPLC retention times of 2,4-dihydroxy-6-heptylbenzoic acid (**3d**), heptyltetraketide pyrone (**6d**), and heptyltriketide pyrone (**7d**). (**A**) Spectrum and retention time of an authentic sample of **3d**. (**B**) Spectra and retention times of **6d** and **7d** produced by PKS-A, using decanoyl-CoA (**5d**) and malonyl-CoA as substrates. (**C**) Spectra and retention times of **3d**, **6d**, and **7d** from co-incubations of the OAC F24I and TKS L190G mutants, using **5d** and malonyl-CoA as substrates. Negative ionization was used in MS (ESI) and MS/MS (ESI) for **3d**, **6d**, and **7d**. UV spectra were obtained at 200-400 nm. The MS/MS (ESI) fragmentation analysis of **3d** indicated an ion fragment peak of m/z 235 [M - H - CO$_2$]$^-$ from the pseudo-molecular ion at m/z 279 [M - H]$^-$, while the analysis of **7d** indicated an ion fragment peak of m/z 125 [C$_6$H$_5$O$_3$]$^-$, corresponding to the α-pyrone from the pseudo-

36

molecular ion at m/z 279 [M - H]$^-$, in addition to an ion fragment peak of m/z 235 [M - H - CO$_2$]$^-$. LC-MS (ESI) and MS/MS (ESI) condition; see Material and Methods. LC-MS (ESI) and MS/MS (ESI) of **9d** were shown in **Fig. 29**.
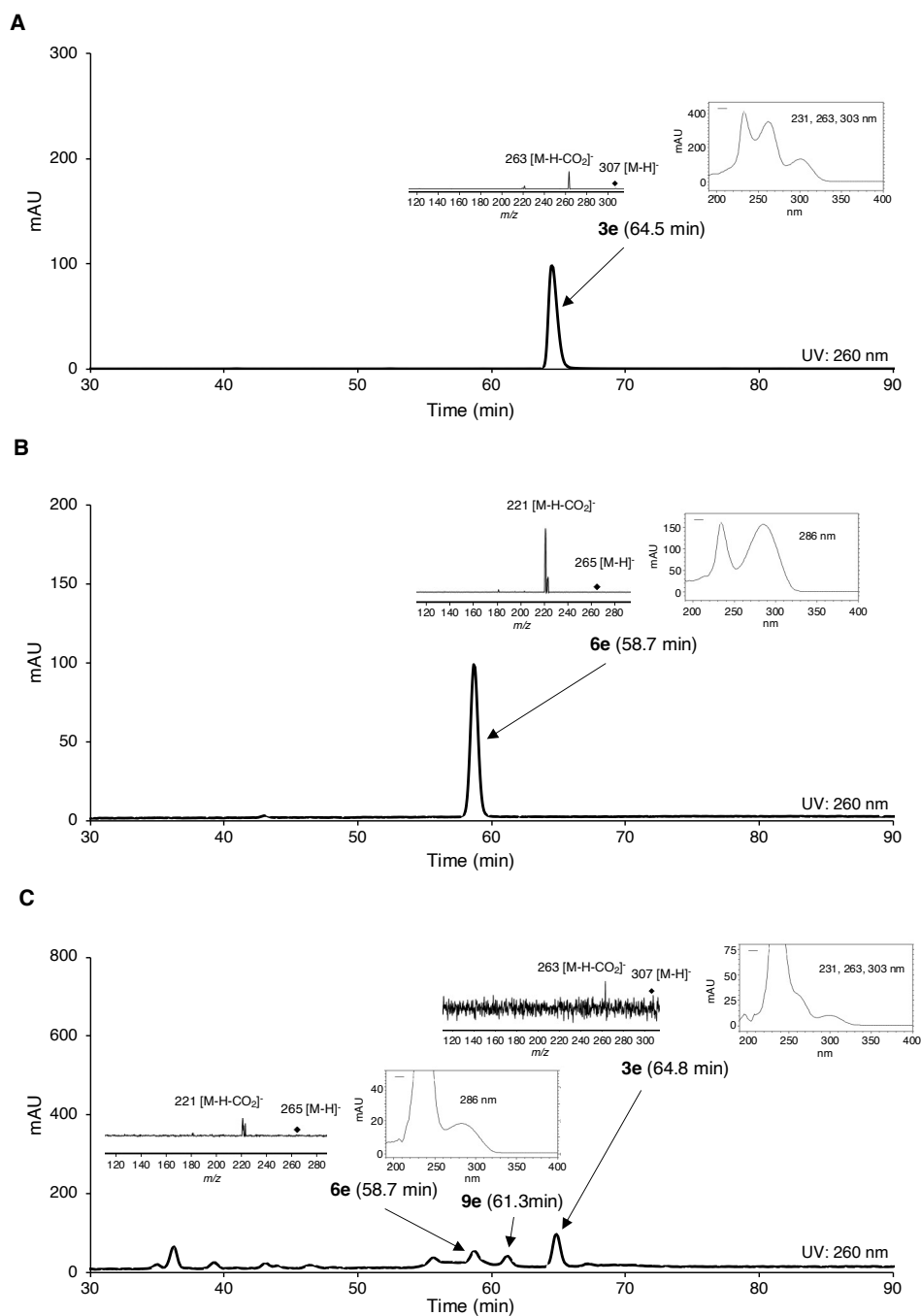
Fig. 24 MS (ESI), MS/MS (ESI), UV spectra and HPLC retention times of 2,4-dihydroxy-6-undecylbenzoic acid (**3e**) and undecyltetraketide pyrone (**6e**). (**A**) Spectra and retention times of authentic samples of **3e**. (**B**) Spectra and retention times of **6e**, produced by PKS-A using lauroyl-CoA (**5e**) and malonyl-CoA as substrates. (**C**) Spectra and retention times of **3e** and **6e** from co-incubations of the OAC F24I and TKS L190G mutants using **5e** and malonyl-CoA as substrates. Negative ionization was used in MS (ESI) and MS/MS (ESI) for **3e** and **6e**. UV spectra were obtained at 200-400 nm. LC-MS (ESI) and MS/MS (ESI) condition; see Material and Methods. LC-MS (ESI) and MS/MS (ESI) of **9e** were shown in **Fig. 30**.

1.8   Proposed structures newly appeared in the co-incubation assay

The co-incubation assays using OACs and the TKS L190G mutant indicated the new productions of compounds **9b**–**e** in the reaction mixture (**Figs. 19**–**20**). The compounds **9b**–**e** can only be seen when the TKS L190G mutant was used for the enzyme reaction with wild-type OAC and its mutants (**Figs. 19**–**24**). In particular, the productions of **9c**–**e** were increased especially when the F24I/L and Y27L/M mutants were co-incubated with the TKS L190G mutant (**Figs. 19**–**20**, **25**, **26**). Careful analyses revealed trace amounts of **9b**–**e** in the sole incubation of the TKS L190G mutant. The HRMS (ESI) analyses revealed that **9b**–**e** possessed the molecular formulas $C_{14}H_{18}O_5$, $C_{16}H_{22}O_5$, $C_{18}H_{26}O_5$, and $C_{20}H_{30}O_5$, respectively, which were one acetyl unit (CH_2CO) higher than those of the corresponding **3** and **7** (**Figs 27**–**30**), suggesting that **9b**–**e** are alkylpentaketides derived from the five malonyl-CoA with hexanoyl-CoA (**5b**) by TKS followed by cyclization of the resultant linear pentylpenta-β-ketide-CoA (**10b**–**e**) by OACs (**Fig. 26**).
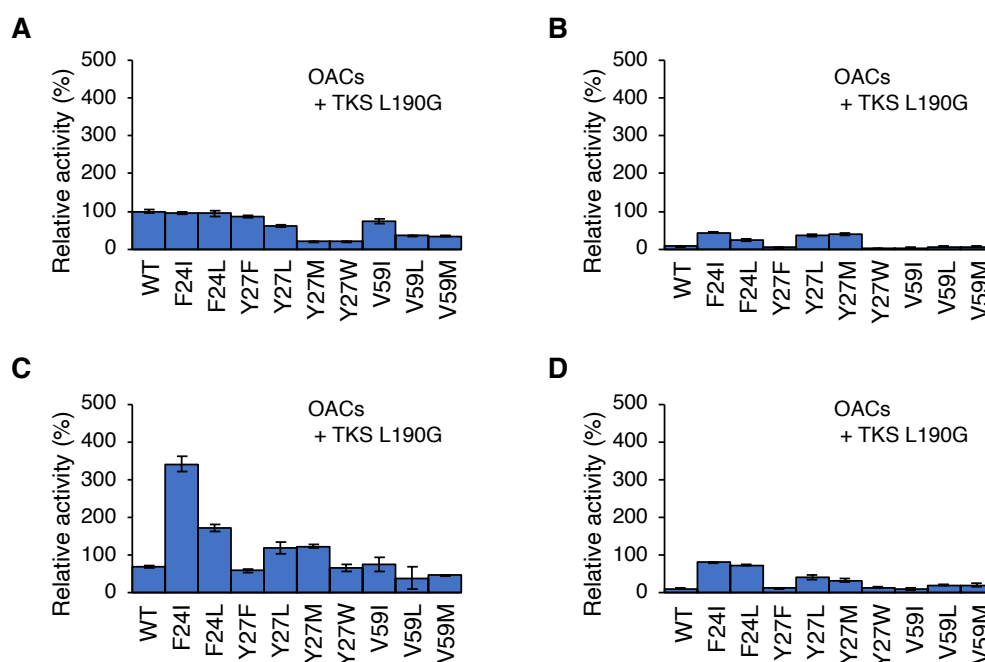

Fig. 25 Relative production of **9** in the co-incubations of OACs with the TKS L190G mutant using (**A**) **5b**, (**B**) **5c**, (**C**) **5d**, and (**D**) **5e** and malonoyl-CoA. The productions are percentages of the **9b**–**e** productions relative to those of wild-type OAC, respectively. Data are presented as mean ± SD (standard deviation, $n = 3$). WT: wild-type enzyme.
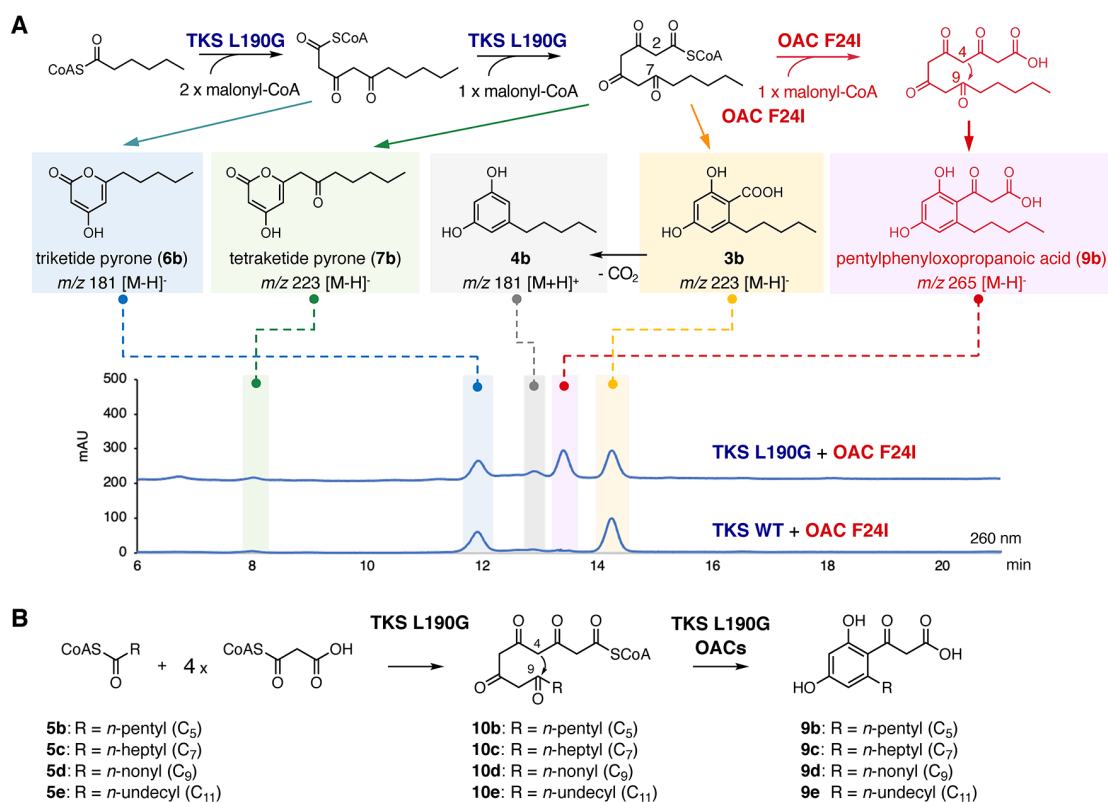
Fig. 26 Plausible structures of **9b**–**e** and the proposed pathway for their formation by TKS L190G and wild-type OAC or its OAC F24I mutant. (A) HPLC elution profiles of the products obtained from co-incubation of OAC F24I and wild-type TKS or its L190G mutant, and proposed pathway for the formation of **3b**, **4b**, **6b**, **7b**, and **9b**. (B) Proposed pathway for the formation of **9b**–**e**.

In order to confirm the structure of **9**, a large-scale enzyme reaction for the production of **9b** was carried out to obtain sufficient amount for NMR measurement. However, during the NMR measurement or fractionation by the HPLC data, compound **9b** was broken, suggesting its instability, although the detail reasons are unclear. Thus, their exact structures have not yet been identified. However, considering the expected molecular formula and cyclization points of linear **10b** that could be produced by the TKS L190G mutant, three structure as shown in **Fig. 31** are predicted. Furthermore, HRMS/MS (ESI) analysis of **9b**–**e** measured on each parent peak, showing decarboxylated fragment ion peaks (**Figs. 27–30**), suggested that the structure **9b-3** (**Fig. 31**) is obviously excluded from candidate structures. In addition, a similar case was also found in the combinatorial biosynthesis study previously performed in our laboratory, in which OAC accepted linear pentylheptyl-β-ketide-

CoA as a substrate derived from **5b** and six malonyl-CoA by OKS to produce C-8/C-13 aldol-type cyclized product, namely pentylaloeson.[31] Considering the comprehensively assessment of the significantly expanded active site cavity of the TKS L190G mutant and the catalytic property of OAC catalyzing the C-2/C-7 aldol type cyclization of **8**, together with the HRMS and MS/MS data, as well as previously observed catalytic potential of OAC for the formation of pentylaloeson, **9b–e** might be 3-(2',4'-dihydroxyphenyl)-3-oxopropanoic acid with *n*-pentyl, *n*-heptyl, *n*-nonyl, and *n*-undecyl moieties at C-6', respectively (**Figs. 26b**, **27-30**). Thus, OACs most likely accepted **10** produced by the TKS L190G mutant and facilitated its C-4/C-9 aldol cyclization to generate **9b–e** (**Fig. 26**).
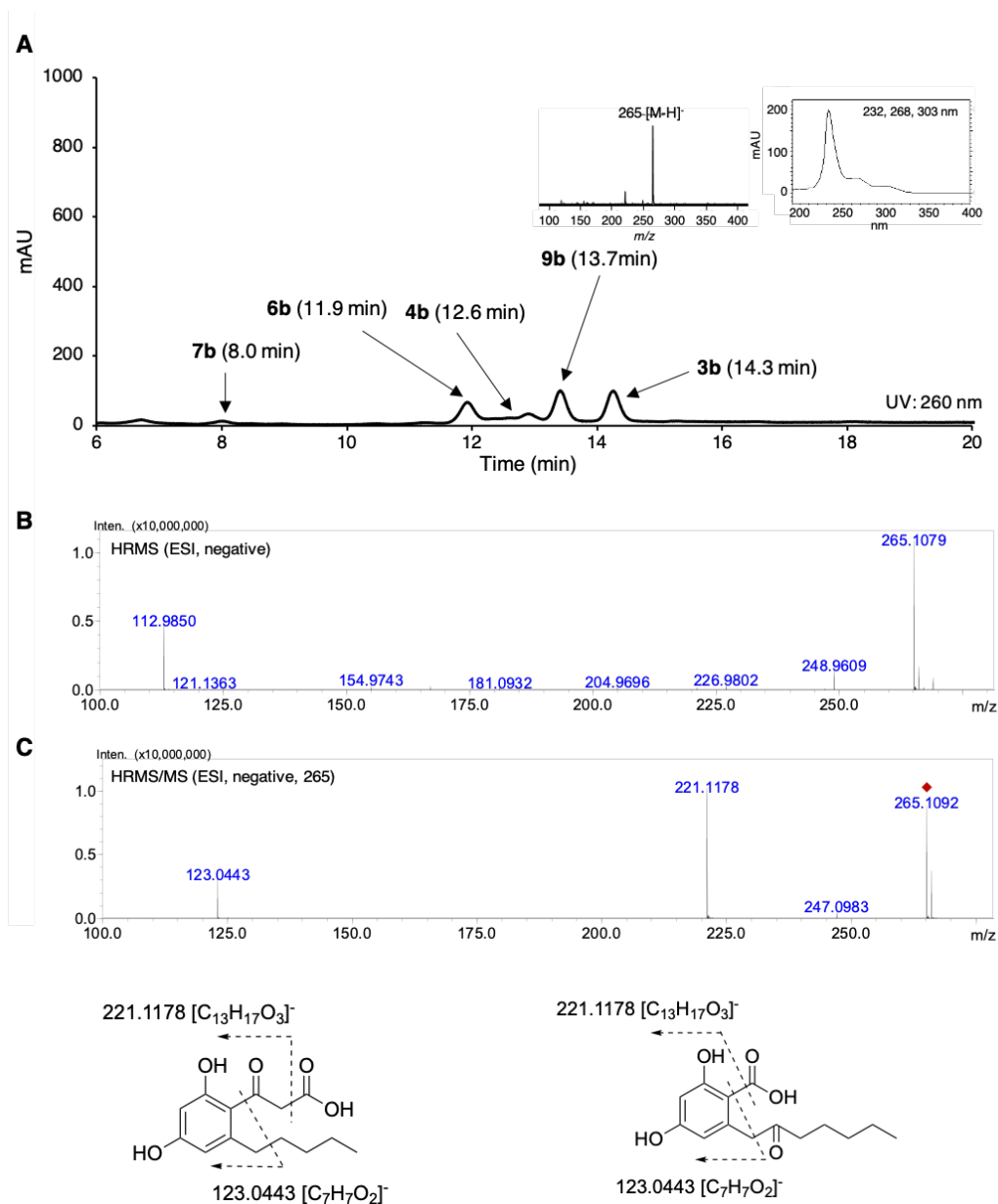
Fig. 27 MS and UV spectrum of **9b**. (**A**) LC-MS (ESI), (**B**) HRMS (ESI), and (**C**) HRMS/MS (ESI). Negative ionization was used. The UV spectrum was obtained at 200-400 nm. LC-MS (ESI) condition; see the Material and Methods.
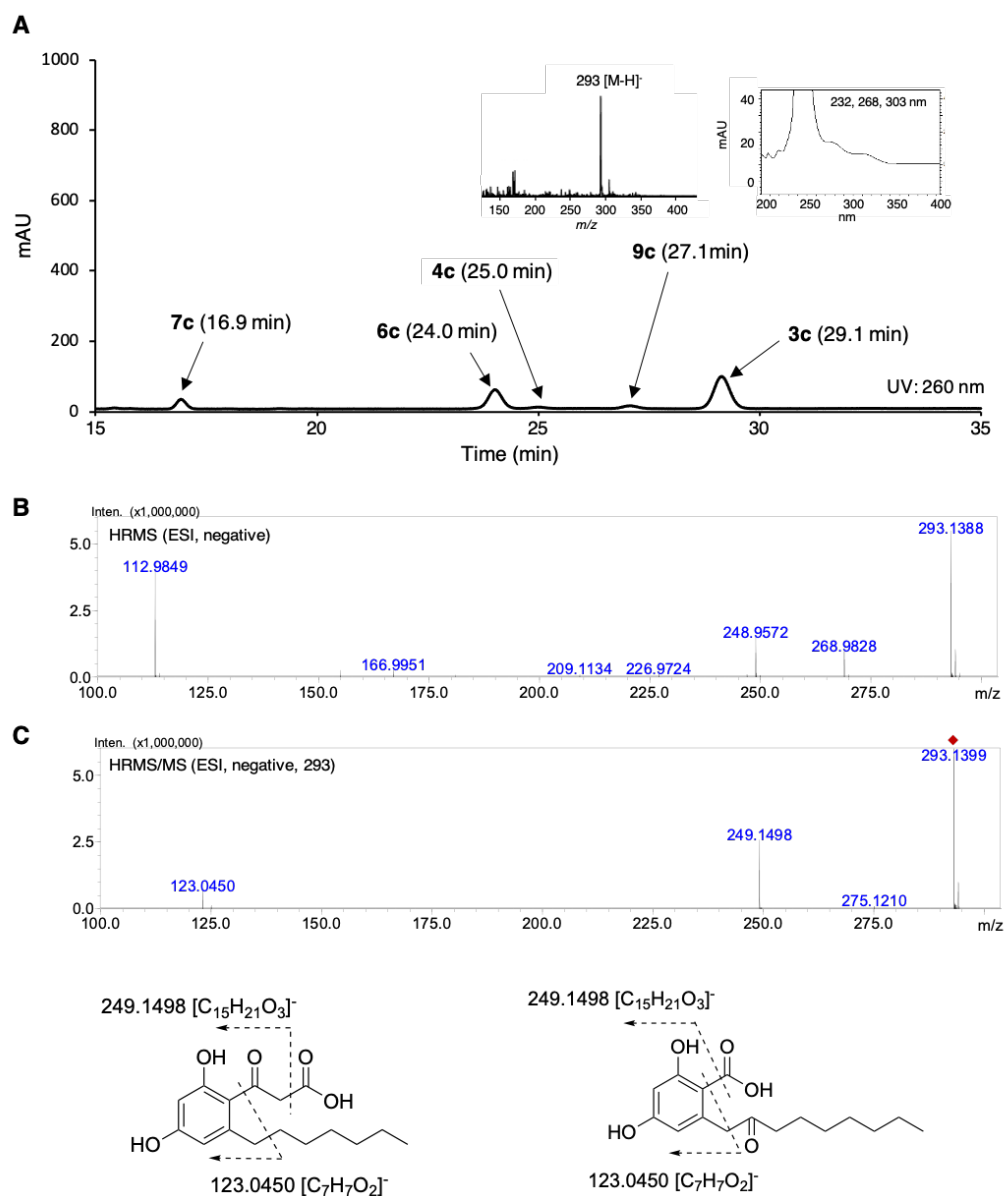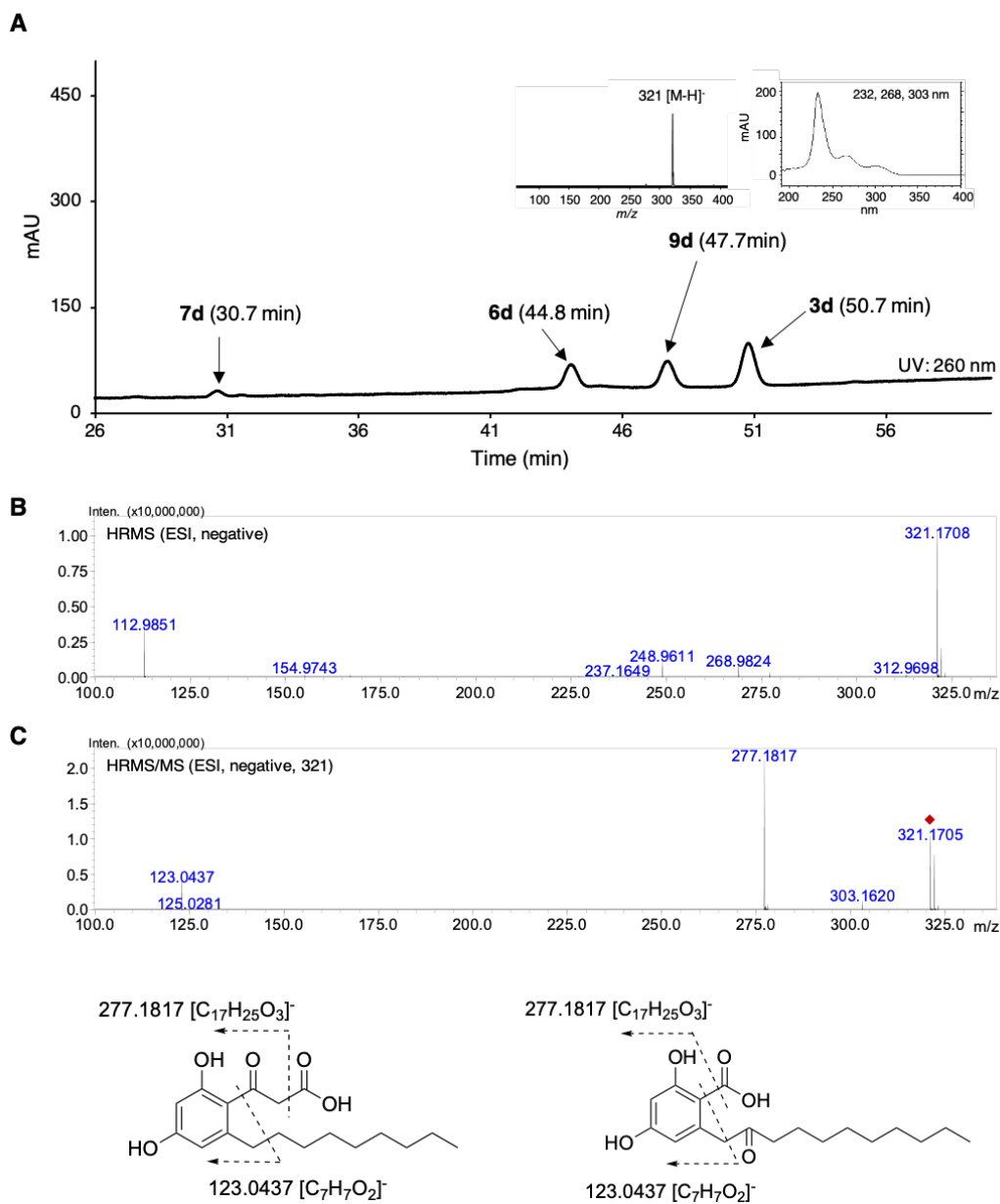
42

Fig. 28 MS and UV spectrum of **9c**. (**A**) LC-MS (ESI), (**B**) HRMS (ESI), and (**C**) HRMS/MS (ESI). Negative ionization was used. The UV spectrum was obtained at 200-400 nm. LC-MS (ESI) condition; see the Material and methods.
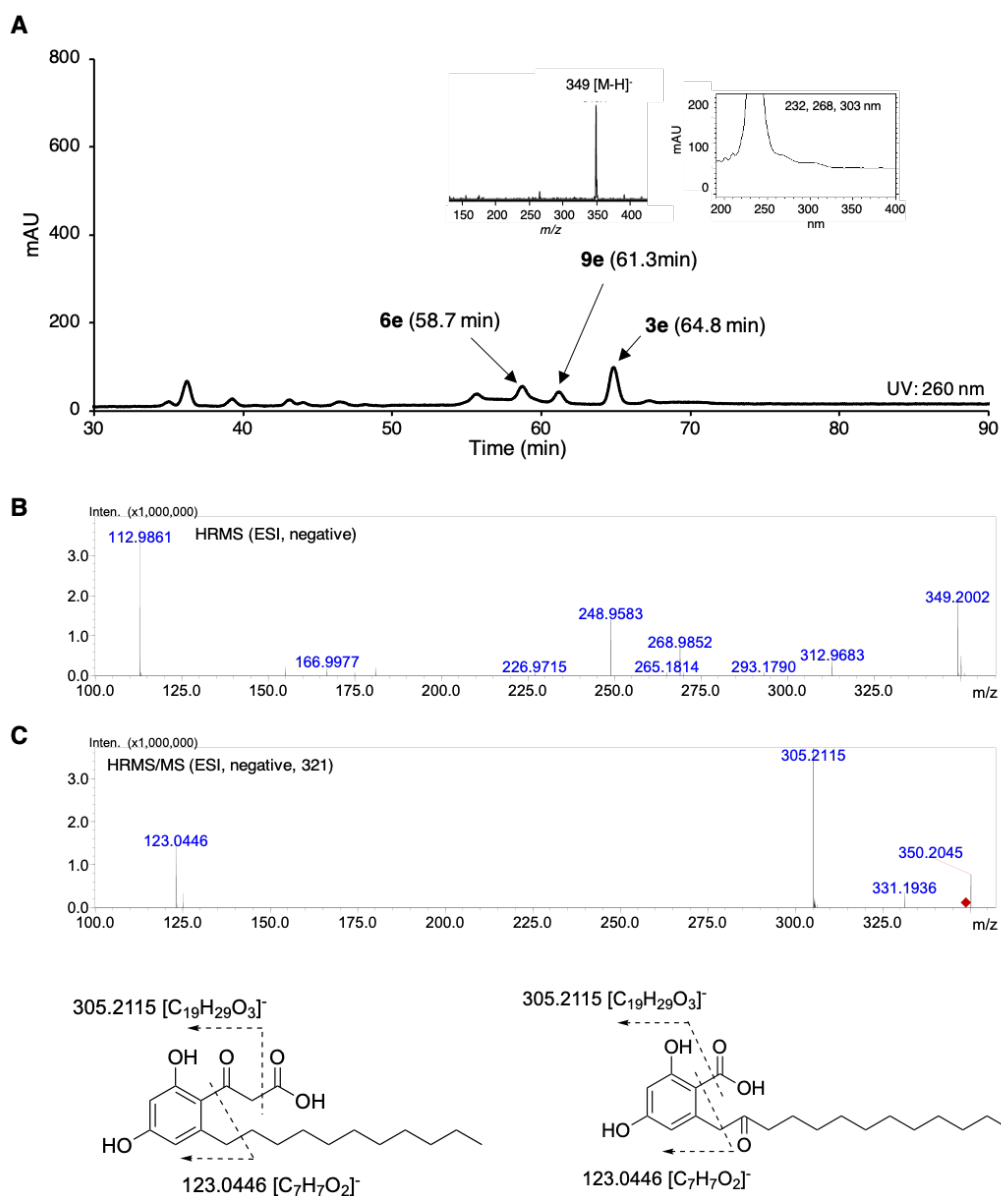
Fig. 29 MS and UV spectrum of **9d**. (**A**) LC-MS (ESI), (**B**) HRMS (ESI), and (**C**) HRMS/MS (ESI). Negative ionization was used. The UV spectrum was obtained at 200-400 nm. LC-MS (ESI) condition; see the Material and methods.
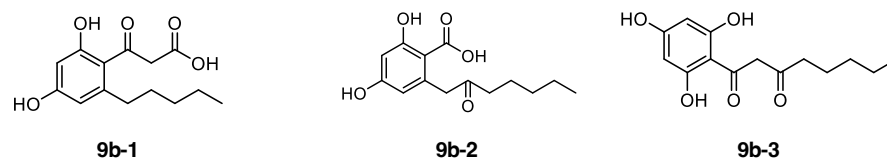
44

Fig. 30 MS and UV spectrum of **9e**. (**A**) LC-MS (ESI), (**B**) HRMS (ESI), and (**C**) HRMS/MS (ESI). Negative ionization was used. The UV spectrum was obtained at 200-400 nm. LC-MS (ESI) condition; see the Material and methods.

45

Fig. 31 Proposed possible structures of **9b** based on the cyclization pattern of OAC and the HRMS (ESI) data.

1.9   Summary of Chapter 1

The engineering approach of the OAC and TKS successfully improved the ability of both enzymes to generate the cannabinoid core with a linear fatty acyl moiety up to *n*-undecyl. The findings provide beneficial insights toward the further development of various alkylcannabinoid analogs by synthetic biological approaches. In addition, further structure elucidations of **9b**–**e** may unveil not only the additional abilities of the TKS L190G mutant to condense four molecules of malonyl-CoA into **10b**–**e**, but also the natural catalytic properties of OAC to accept the penta-*β*-ketide substrates.

CHAPTER 2

Antibacterial properties of 3b and its derivatives

2.1 Introduction

As mentioned above, **3b–e** might be potential drug seeds, due to the acquired hydrophobicity in their structures with the elongated alkyl-side chain (**Fig. 4**). In order to identify their potential, antibacterial activities of **3b–e** against *S. aureus* was evaluated as the preliminary investigation. To this end, I also assessed the antibacterial activities of **3a** and **3f** to further evaluate the chain-lengths effects on their antibacterial activity. Apart from this, the antibacterial potential of the all compounds against *B. subtilis* was also tested in this study, since **1b** reportedly showed antibacterial activity against this Gram-positive bacterium.[33] All the compounds were evaluated on their antibacterial potential by using the MTT methods. Ampicillin was used as a positive control.

2.2 Antibacterial activities of 3b and its analogs

Although **3b–e** were produced by using the engineered OAC and TKS, the *in vitro* reaction seemed to be difficult to obtain enough amount of the compounds for the antibacterial assay, from point of view of the cost of the substrate. Hence, **3b–e** as well as **3a** and **3f** were chemically synthesized according to previously reported method[34], as shown in **Fig. 32**, to obtain sufficient amounts in a more cost-effective way for antibacterial activity evaluations. The antibacterial activities of the tested compounds in this study are summarized in **Table 1**. The assay revealed that both **3a** and **3b** with *n*-butyl and *n*-pentyl moieties demonstrated no antibacterial activities against both tested bacteria, even at 200 μM concentrations, whereas **3c** was found to exhibit potency against both bacteria. Remarkably, further chain-length-dependent increased activities were found in **3e** and **3f**, which exhibited MIC values of 6.25 μM and 2.5 μM against *S. aureus* and *B. subtilis*, respectively. It is interesting to see that the previously inactive **3b** has newly obtained their antibacterial potential with the elongation of their alkyl-side chain, especially against *B. subtilis.*
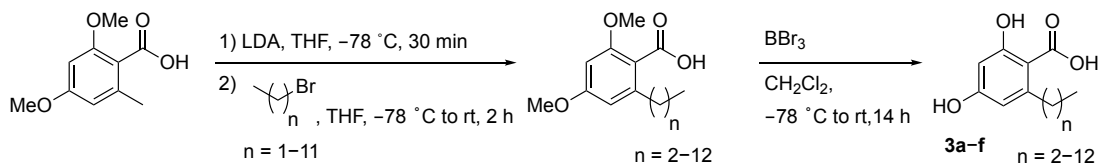
Fig. 32 Synthesis scheme of **3a–f**.

It is remarkable that **3e** and **3f** showed potent antibacterial activity against *B. subtilis* similar to those reported for **1b** and **2b** despite the lack of the prenyl moiety. On the other hand, **4b** which is the decarboxylated form of **3b**, showed antibacterial activity against *S. aureus* with MIC values ranging from 64 to 128 μg/mL in a previously reported study[33] even though it possesses a simpler structure with similar pentyl side-chain when compared with **3b**. However, **3b** showed no antibacterial activity in this study which may suggest that the carboxylate moiety in **3b** might not be beneficial to provide the antibacterial potential to the compound. To clarify this, and in the absence of the literature describing the alkyl chain-length-dependency of **4b**, I synthesized a series of **4b**-analogs according to the previously reported methods[35] (**Fig. 33**) and evaluated their antibacterial activities using the same method as described above.
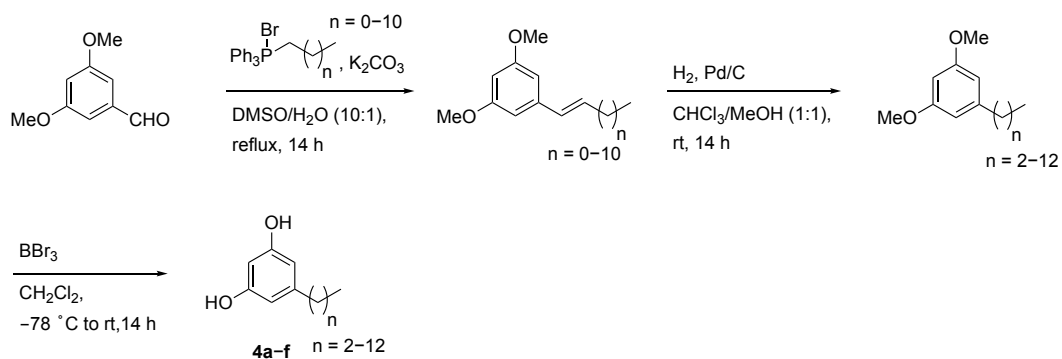

Fig. 33 Synthesis scheme of **4a–f**.

Table 1. Antibacterial activities of **1a–f**, **2a–f**, **3a–f**, and **4a–f**.

Sample	MIC (μM)			
	S. aureus	*B. subtilis*	*K. pneumoniae*	*E. coli*
1a	25	25	>200	>200
1b	2.5	3.13	>200	>200
1c	2.5	6.25	>200	>200
1d	6.25	>200	>200	>200
1e	25	>200	>200	>200
1f	>200	>200	>200	>200
2a	12.5	12.5	>200	>200
2b	3.13	2.5	>200	>200
2c	3.13	1.25	>200	>200
2d	12.5	3.13	>200	>200
2e	25	6.25	>200	>200
2f	>200	50	>200	>200
3a	>200	>200	>200	>200
3b	>200	>200	>200	>200
3c	100	200	>200	>200
3d	12.5	25	>200	>200
3e	6.25	2.5	>200	>200
3f	6.25	2.5	>200	>200
4a	>200	>200	>200	>200
4b	>200	>200	>200	>200
4c	100	100	>200	>200
4d	12.5	12.5	>200	>200
4e	6.25	3.125	>200	>200
4f	200	12.5	>200	>200
Ampicillin[a]	0.15	0.15	-	-
Kanamycin[a]	-	-	1.56	1.56

[a]Positive control

2.3   Antibacterial activities of 4b and its analogs

In contrast to the previous report[33], **4b** was detected as non-active compound against *S. aureus* in the assay (**Table 1**). In this study, different strains were used for the assay as compared with the previous study. Thus, the differences might lead different result. Furthermore, the assay revealed the same chain-length-dependent patterns of antibacterial activity of the **4b**-analogs with alkyl moieties ranging from *n*-propyl to *n*-undecyl corresponding to **4a**–**4e** against *S. aureus* as those of the **3**-series. However, **4f** was shown to be a significantly less antibacterial compound against *S. aureus*, with a MIC value of 200 μM, as compared with that of **4e**. Thus, the **4b**-analog with the *n*-undecyl moiety (**4e**) was the most potent against *S. aureus*, with a MIC value of 6.25 μM in the tested **4**-series, and its potency was consistent with those of

3e and **3f**. A similar chain-length-dependent pattern was also found in the antibacterial activities of the **4**-series against *B. subtilis*. Among the tested **4**-series, the highest activity against *B. subtilis* was shown in **4e** with the *n*-undecyl moiety. A MIC value of **4e** was 3.125 μM, which was slightly weaker than those of **3e** and **3f**. Presumably, due to the loss of the carboxylic group from the structure, compound **4f** showed lower activity, despite having the same alkyl side-chain length as **3f**. The lower activities of the **4**-series than the **3**-series against *B. subtilis* suggested that the carboxylate moiety could be an important functionality for enhancing the antibacterial activity against this bacterium. It is also noteworthy that the **4**-series achieved the optimum length at the *n*-undecyl moiety among the tested length. The previous studies reported that the *n*-octyl moiety was the best length for the activities of Δ^8-THC and Δ^9-THC at C-3, rather than longer ones.[36] In addition to this finding, the observed results in this study would suggest that the alkyl side-chain length is also one of the factors regulating the activities.

2.4　Antibacterial activities of 1b and its analogs

　　　Previously, only the antibacterial activities of **1b** and **2b** with an *n*-pentyl moiety have been reported. Thus, compound **1b** and its analogs were also synthesized from the respective **4** as the starting material, in order to determine whether the length of the alkyl side-chain influences the bioactivities of **1b** and **2b** (**Fig. 34**). The antibacterial assays showed the highest potencies of **1b** with the *n*-pentyl moiety (**1b**) and **1c** with *n*-heptyl moiety (**1c**) against *S. aureus* with MIC values of 2.5 μM (**Table 1**). Furthermore, **1b** also exhibited the highest activity against *B. subtilis* with a MIC value of 3.125 μM. Compound **1c** was a second highest compound among the **1**-series. In contrast, **1d** and **1e** exhibited MIC values of 6.25 μM and 25 μM against *S. aureus*, respectively, which indicated their decreased antibacterial properties. Furthermore, **1f** with the *n*-tridecyl moiety no longer showed the activity against *S. aureus*. In the case of *B. subtilis*, the loss of the activity against *B. subtilis* was started from **1d**. However, antibacterial properties of **1a** with the *n*-propyl moiety against *S. aureus* are different from the antibacterial properties of **3a** and **4a**. However, the observed property is quite similar to those of the cannabinoids Δ^9-THCV and CBDV, which are possessed the same *n*-propyl lipophilic side-chains at C-3 instead of *n*-pentyl moieties, and less

activity against methicillin-resistant *S. aureus* (MRSA) than Δ^9-THC and CBD, respectively, were shown to these compounds.[37] Overall, the optimum chain-lengths on the **1**-skeleton for the antibacterial activities were *n*-pentyl and *n*-heptyl moieties against *S. aureus* and the *n*-pentyl moiety against *B. subtilis*, respectively, in sharp contrast to those of the **3**- and **4**-series. It should be noted that **1b** and **1c** showed higher antibacterial activities against *S. aureus* than the **3**- and **4**-series. However, the antibacterial activities of **1b** and **1c** against *B. subtilis* were slightly lower than those against *S. aureus*. This observation is different from the **3**- and **4**-series, in which **3e** and **3f** with long *n*-undecyl and *n*-tridecyl moieties and **4e** with an *n*-undecyl moiety showed more potent activities.
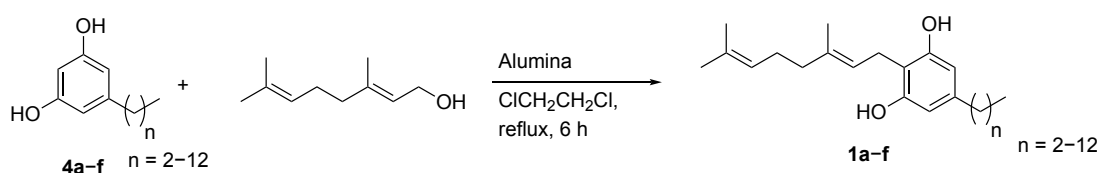
Fig. 34 Synthesis scheme of **1a–f**.

2.5   Antibacterial activities of 2b and its analogs

In order to further clarify the effect of the alkyl chain length of the related compounds on the activity, synthesis of **2a–f** was carried out, by using the same methods as the **1**–series. However, **2a–f** was not successfully obtained by the methods. Presumably, as previously reported for the synthesis of cajaninstilbene acid (Cajanine), the carboxylate and hydroxy group were protected by methyl group to generate the respective prenylated compounds (**Fig. 35**)[38]. Further protection and deprotection steps are expected to be required for the synthesis of **2a–f**. However, a recent study reported direct regiospecific prenylations of **3a** and **3b** to yield **2a** and **2b** by exploiting the NphB G286S/Y288N mutant, respectively.[39] Therefore, the direct incorporation of the geranyl moiety into **3** with the NphB G286S/Y288N mutant were performed in this study, to synthesize **2b** and its analogs (**Fig. 36**). The study revealed that the mutant enzyme can also produce **2c–f** from **3c–f** (**Figs. 37–42**), respectively, and the chemosynthesized **2a–f** were used for the antibacterial activities against *S. aureus* and *B. subtilis*.
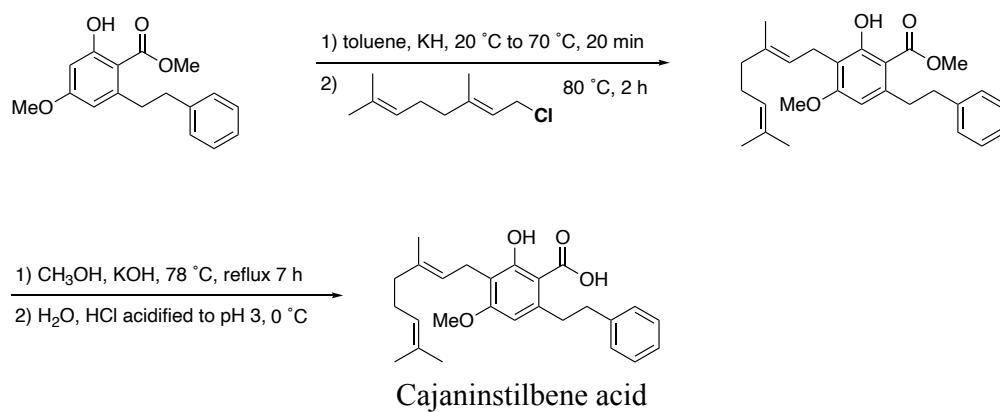
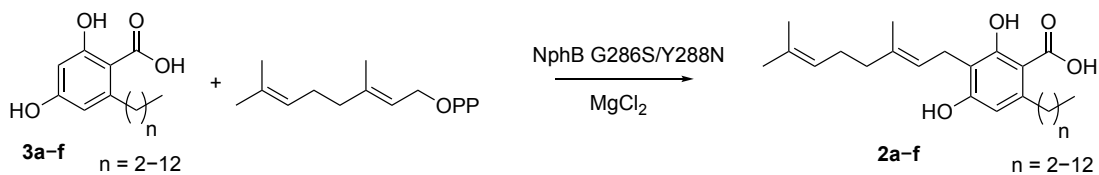**Fig. 35** Synthesis scheme of cajaninstilbene acid (Cajanine).
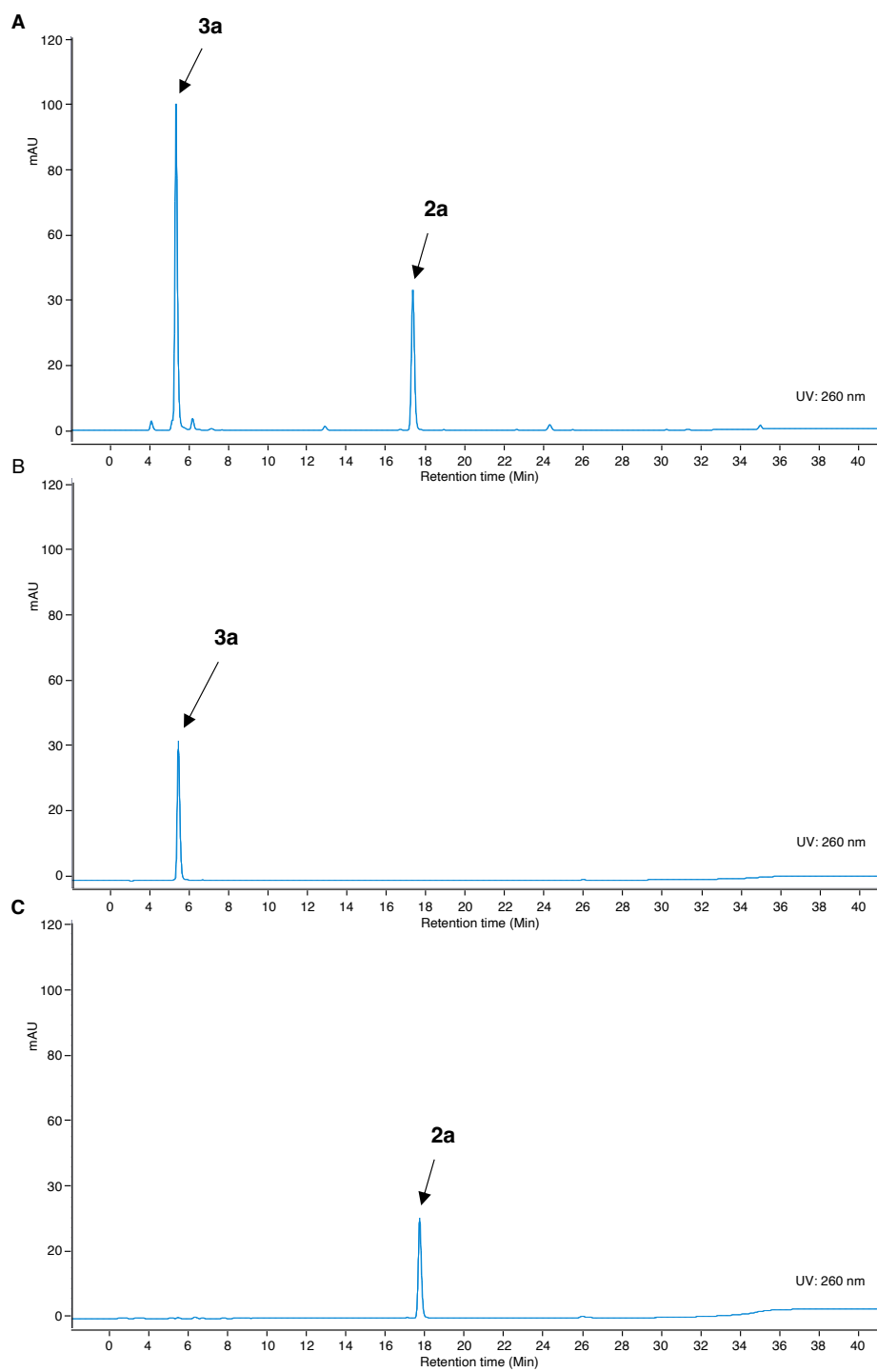

Fig. 36 Synthesis scheme of **2a–f**.

55

Fig. 37 HPLC chromatograms of (**A**) NphB G286S/Y288N reaction products by using **3a** as substrate, (**B**) authentic standard **3a**, and (**C**) authentic standard of **2a**.
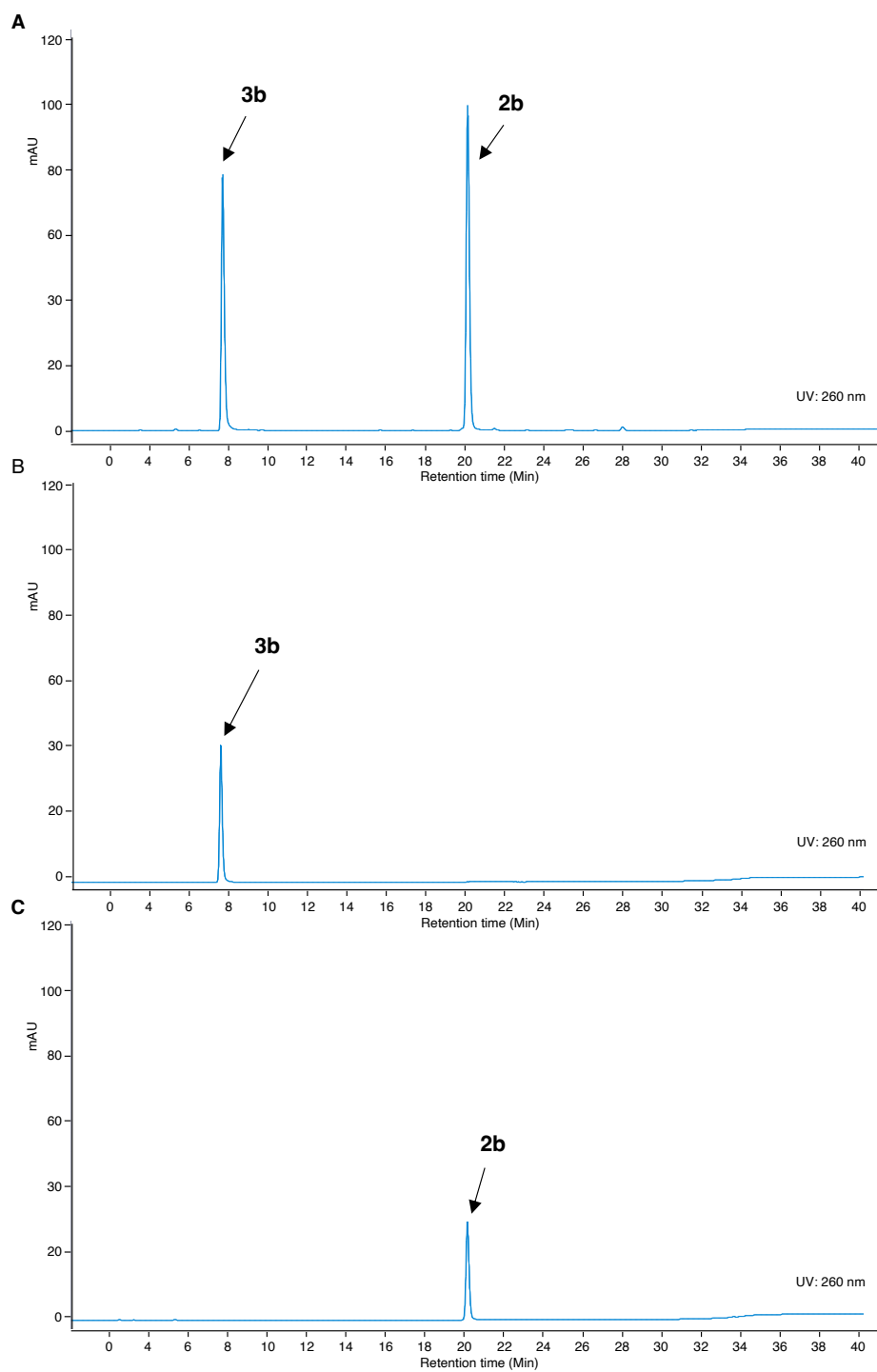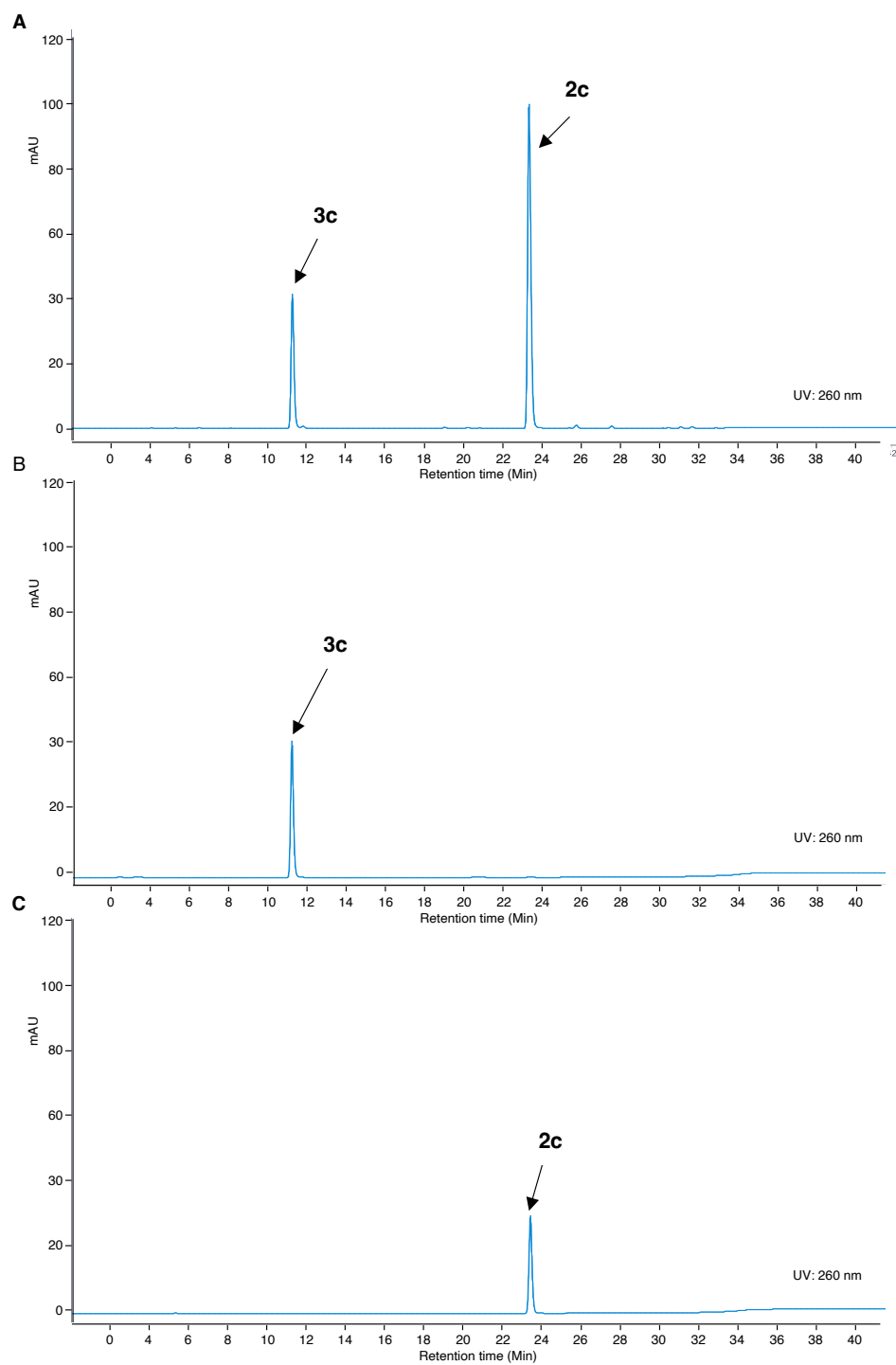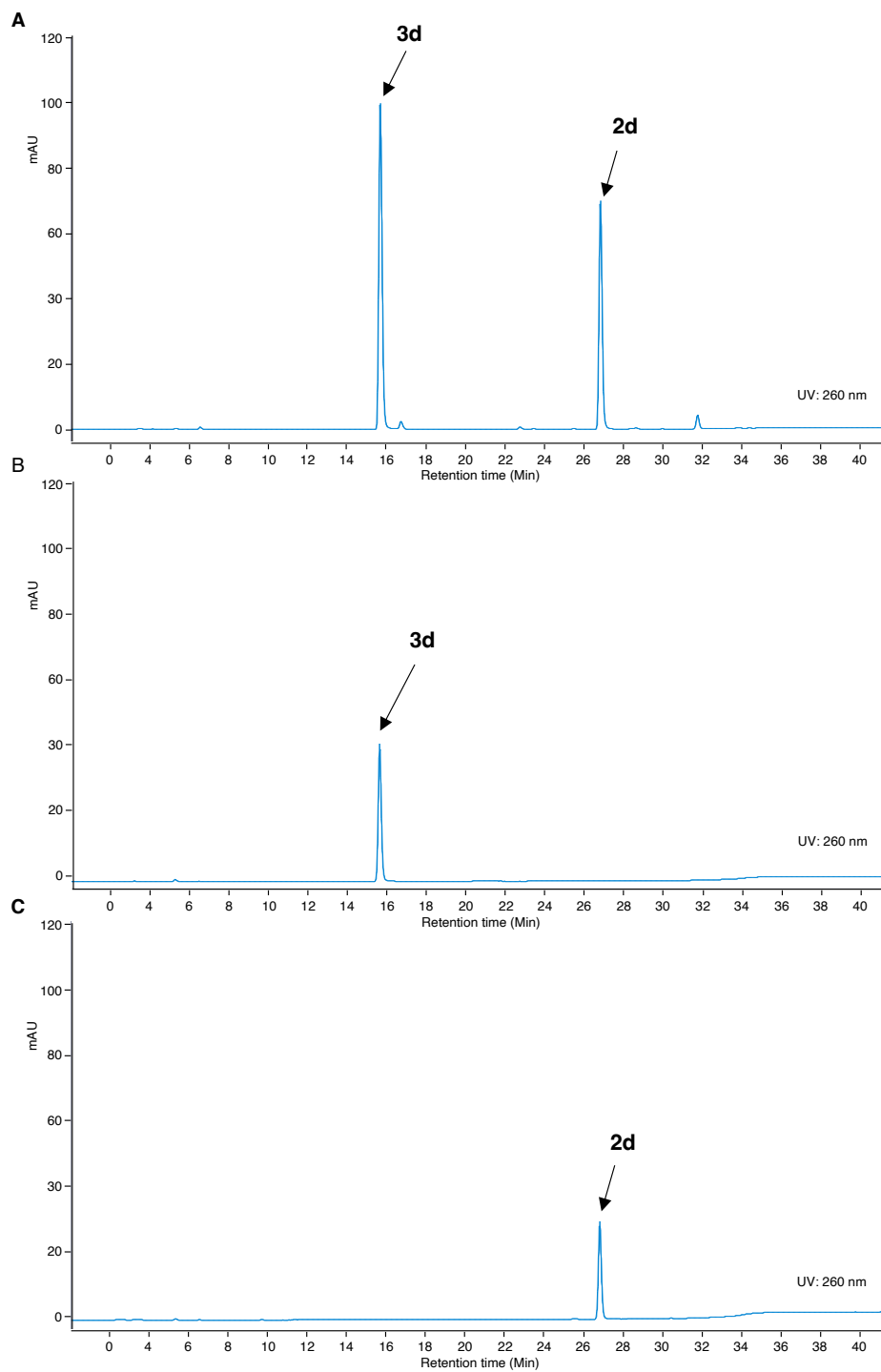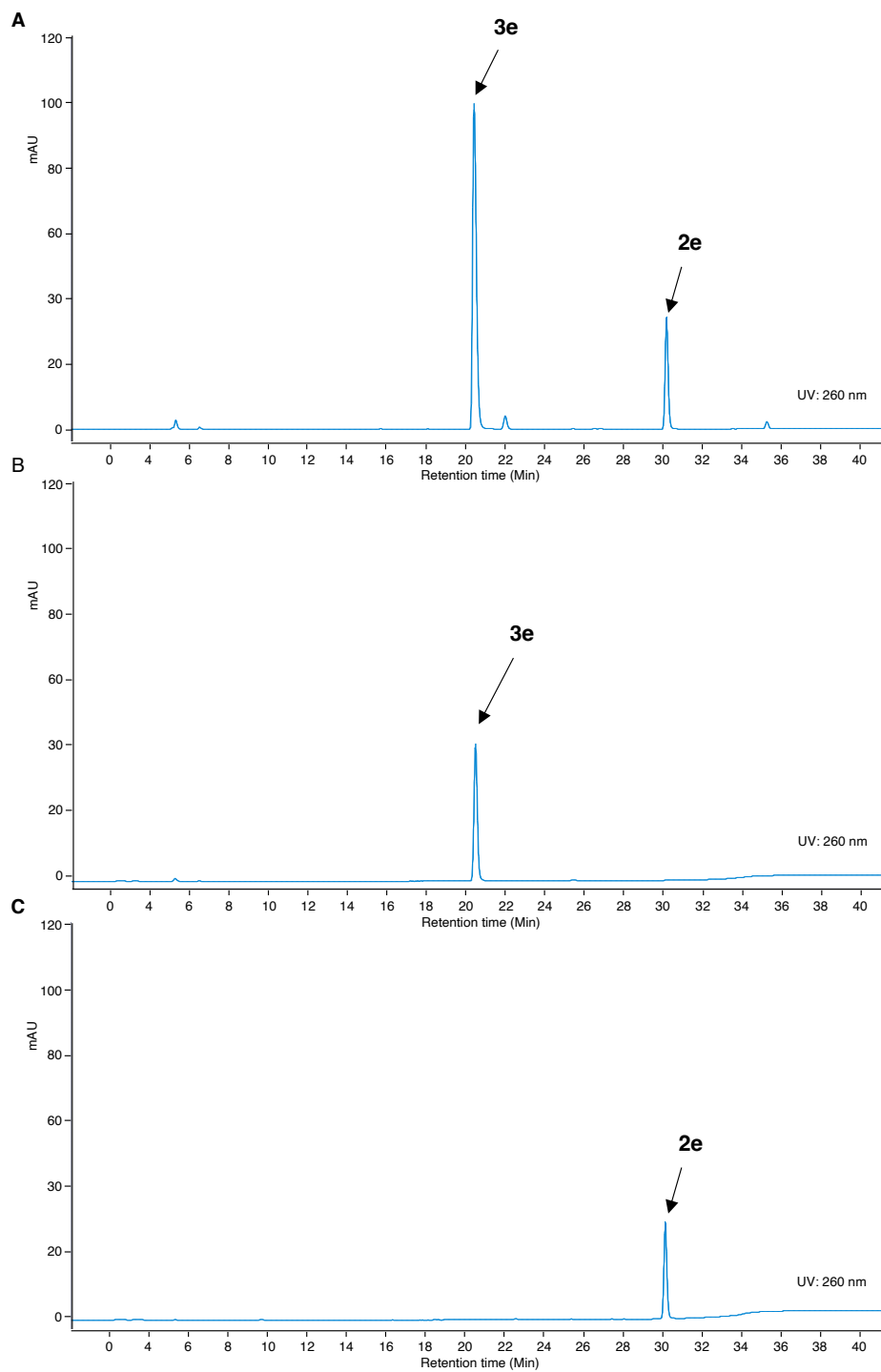
Fig. 38 HPLC chromatograms of (**A**) NphB G286S/Y288N reaction products by using **3b** as substrate, (**B**) authentic standard **3b**, and (**C**) authentic standard of **2b**.

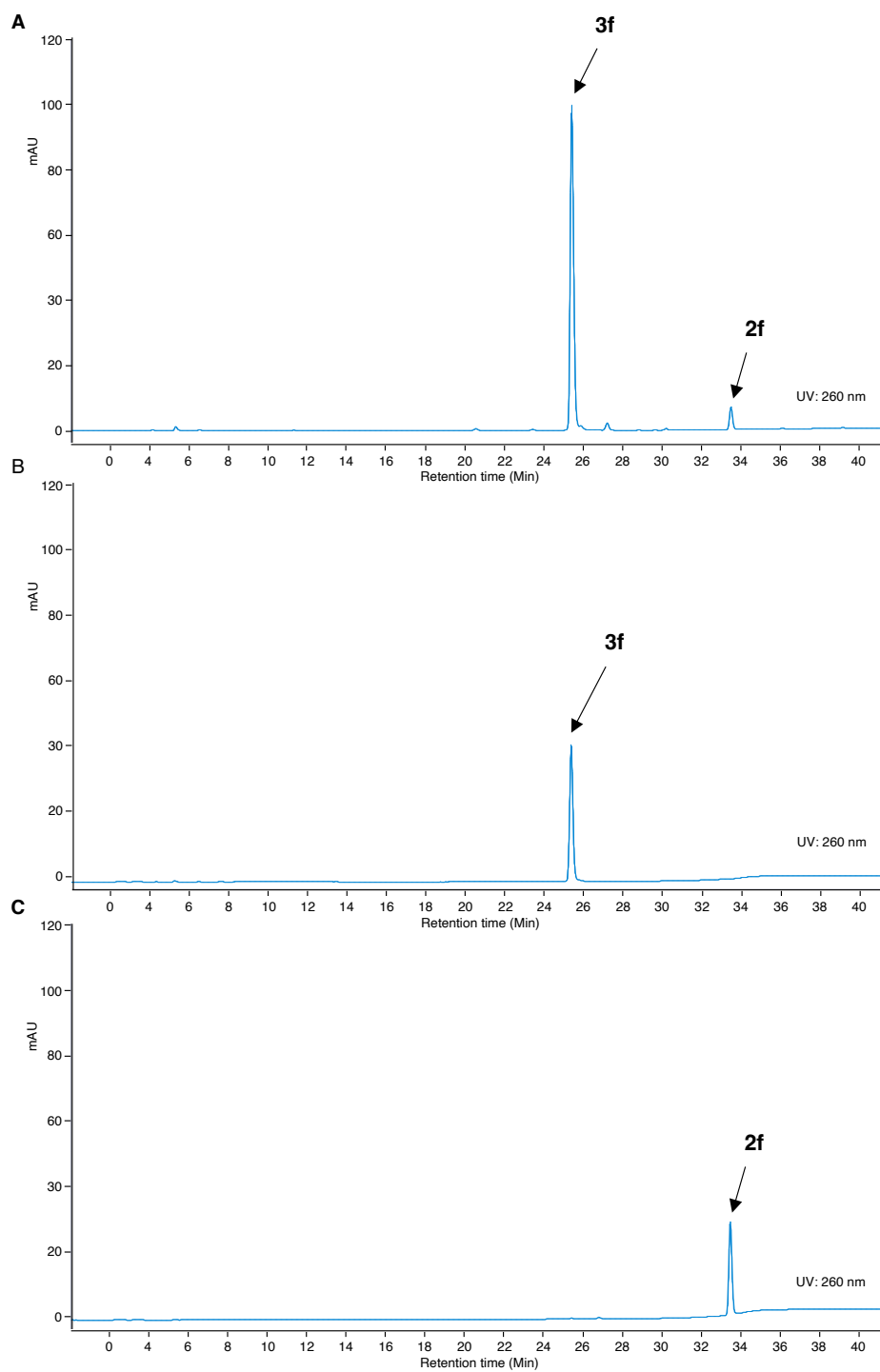**Fig. 39** HPLC chromatograms of (**A**) NphB G286S/Y288N reaction products by using **3c** as substrate, (**B**) authentic standard **3c**, and (**C**) authentic standard of **2c**.

Fig. 40 HPLC chromatograms of (**A**) NphB G286S/Y288N reaction products by using **3d** as substrate, (**B**) authentic standard **3d**, and (**C**) authentic standard of **2d**.

Fig. 41 HPLC chromatograms of (**A**) NphB G286S/Y288N reaction products by using **3e** as substrate, (**B**) authentic standard **3e**, and (**C**) authentic standard of **2e**.

Fig. 42 HPLC chromatograms of (**A**) NphB G286S/Y288N reaction products by using **3f** as substrate, (**B**) authentic standard **3f**, and (**C**) authentic standard of **2f**.

Compound **2b** and its analogs also demonstrated an optimum antibacterial activity with *n*-pentyl and *n*-heptyl moieties against *S. aureus* and *n*-heptyl moiety against *B. subtilis* which is in similar trend with the antibacterial activity of **1b** (**Table 1**). Compound **2f** with *n*-tridecyl moiety showed decreased activity against *B. subtilis* which was similar to the antibacterial results of the **1**-series. The antibacterial potential of **2** decreased with the increased chain-length and this phenomenon was observed from the *n*-nonyl moiety against both Gram-positive bacteria, in a manner similar to those of **1**. It can be postulated that the resorcinol core has gained excessive increased hydrophobicity with the elongated alkyl-side chain could result in lower intracellular concentration due to poor aqueous solubility, thus the antibacterial potential dropped significantly, as observed in **1f**, **2f**, and **4f** (**Table 1**). Finally, comparisons of the activities of all tested compounds demonstrated that **1b/1c** and **2b/2c** are the most and second-most potent cannabinoids as antibacterial agents against *S. aureus*, while **2c** and **3e/3f** are the most and second-most potent compounds as antibacterial agents against *B. subtilis*. The observation in these results suggest that the modulation of the hydrophobic balance of the C-6 alkyl side-chain in combination with the C-3 position could be one of the strategies to enhance the bioactivities of these **3b**-derivatives.

2.6   Summary of Chapter 2

The antibacterial activities described in this study demonstrated the potential of the resultant **3b** derivatives in which the incorporation of a longer alkyl chain at the C-6 position in the resorcylic acid structure newly confers antibacterial properties against *S. aureus* and *B. subtilis*, even if the hydrophobic geranyl moiety was absent from the C-3 position. In particular, the results suggested that the longer *n*-undecyl and *n*-tridecyl alkyl-chains were most effective for enhancing the activities of **3b**-type compounds against *B. subtilis*. The study also demonstrated that the *n*-heptyl modification at C-6 of **2b** effectively enhanced the activity against *B. subtilis*. However, simultaneously, the study also indicated that further elongation of the alkyl moieties decreased the activities of the **2b**-series. Similar cases were also observed in the antibacterial assays for the **1**- and **4**-series, suggesting the importance of the balance between the membrane permeability and the intracellular solubility of the compounds for the activity. Thus, further evaluations of the antibacterial activities, as well as other

various biological activities of **2b** and **3b** derivatives, especially with optimized hydrophobicities at both the alkyl and prenyl side-chain positions of the core skeleton, would provide useful insights into the development of new medicines.

Conclusion

This study demonstrated that longer alkyl-chain up to *n*-undecyl can be generated by exploiting dual engineering of OAC and TKS. The substitution of residue F24 lining the bottom of the active-site cavity of OAC with Ile caused expansion of the pentyl-binding pocket from 9 Å to 12 Å. When TKS L190 was replaced with a smaller amino acid, glycine, the active-site cavity was expanded by opening the space to a hidden pocket in which this L190 residue acts as a gate and protrude into the cavity. This study is for the first time that wild-type OAC naturally possesses the ability to **3b**-analog with *n*-undecyl moiety. In addition, it is also noteworthy that a new compound has been detected in the enzyme assays in the combinatorial use of TKS L190G and OAC mutant enzymes. This new compound is proposed to be an alkyl-oxopropanoic acid. The discovery of this new compound may suggest that OAC catalyzes the C-4/C-9 aldol cyclization to form this novel product, considering the significantly expanded cavity of TKS L190G mutant as well as the catalytic property of OAC.

Apart from the newly obtained enzyme properties, it is also particularly interesting that the **3**-series showed antibacterial activity in a chain-length dependent manner with potency comparable to **1b**, even in the absence of the geranyl moiety. Further evaluation of antibacterial activities of the **4**-series showed antibacterial properties in a chain-length dependent manner, but the activity dropped at *n*-tridecyl moiety. The prenylated homologs for both **3b** and **4b**, compound **1b** and **2b** showed highest antibacterial activity at shorter chain length, which is in an opposite trend from the **3**-series. This implies that it is vital to maintain both the membrane permeability and the intracellular solubility of the compounds for the activity.

This study thus provided novel insights into the versatilities of OAC and TKS to create longer alkyl-chain analogs. It is hope that the introduction of these engineered biosynthetic enzymes into the synthetic biological system produces pharmaceutically important cannabinoids, which can be further developed into useful medicine. The use of biological system to produce cannabinoid analogs with tailored C3 side chains might somehow provide solution to the complexity of obtaining various cannabinoids with unique side-chain by chemical synthesis. In addition, the antibacterial results in this study also proved that despite being the intermediate in the biosynthesis of cannabinoids and has simple structure, the long alkyl-chain of **3b** indeed possesses

some biological activity. It is of particular interest to further evaluate these created compounds with various alkyl-chain length on their neuron-related therapeutic potential, since the final cannabinoid products have been proven to induce various biological action in the central nervous system. Thus, the results obtained in this study also provided insight the biological activities of **3b** or other analogs in the molecular level, which might lead to ultimately the development of pharmaceutical products responsible for treating or relieving some medical symptoms.

Materials and methods

General Experimental Materials

All chemical reagents, including **3b**, were purchased from Fujifilm Wako Pure Chemical Corporation unless otherwise specified. Malonyl-CoA and **4b** were purchased from Sigma-Aldrich. Compounds 5**b-f** were synthesized as previously reported.[40, 41] The COSMOGEL® GST-Accept resin was purchased from Nacalai Tesque. LC-MS (ESI) were measured with a 6420 Triple Quad LC/MS spectrometer (Agilent Technologies) coupled to a 1260 Infinity LC system (Agilent Technologies). HRMS (ESI) data were obtained in the positive and negative modes on a SHIMADZU LC-MS-IT-TOF spectrometer. NMR spectra were recorded on an ECA500II and ECX 400P spectrometer (JEOL). Compounds **3a**–**f** were dissolved in dimethyl sulfoxide-d_6 (DMSO-d_6) and compound **1a**–**f**, **2a**–**f**, and **4a**–**f** were dissolved in chloroform-d (CDCl$_3$), and are expressed in δ (ppm) based on the δ residuals of these solvents, at 2.49 and 7.26 for ^{1}H NMR and 39.5 and 77.0 for ^{13}C NMR, respectively.

General Procedure

Construction of OAC mutants

Each full-length cDNA of the OAC mutants was amplified from the previously reported pQE80L expression plasmid encoding wild-type OAC as the template[28] with the PCR method, using KOD-Plus-Neo (TOYOBO) and the pairs of primers listed in **Table 2**. The cDNAs were inserted into the *Sma*I/*Sal*I sites of the modified pQE-80L vector for expression as *N*-terminal GST-tag fusion proteins with a PreScission Protease (PSP) (Amersham Biosciences) cleavage site (LEVLFQGP), using an In-Fusion cloning kit (Takara Bio) according to the manufacturer's protocol. After sequence confirmation, the plasmids were transformed into *E. coli* M15 (pREP$_4$).

Table 2. Oligonucleotides used for construction of OAC and TKS mutant enzymes.

Mutant Name	Oligonucleotide sequence
OAC F24A	F: 5'-GCACAGAAAGAGGAGTTC**GCC**AAAACCTACGTGAATTTGGTGAAC-3'
	R: 5'-GTTCACCAAATTCACGTAGGTTTT**GGC**GAACTCCTCTTTCTGTGC-3'
OAC F24I	F: 5'-GCACAGAAAGAGGAGTTC**ATC**AAAACCTACGTGAATTTGGTGAAC-3'
	R: 5'-GTTCACCAAATTCACGTAGGTTTT**GAT**GAACTCCTCTTTCTGTGC-3'
OAC F24L	F: 5'-GCACAGAAAGAGGAGTTC**CTC**AAAACCTACGTGAATTTGGTGAAC-3'
	R: 5'-GTTCACCAAATTCACGTAGGTTTT**GAG**GAACTCCTCTTTCTGTGC-3'
OAC F24V	F: 5'-GCACAGAAAGAGGAGTTC**GTC**AAAACCTACGTGAATTTGGTGAAC-3'
	R: 5'-GTTCACCAAATTCACGTAGGTTTT**GAC**GAACTCCTCTTTCTGTGC-3'
OAC Y27A	F: 5'-GAGGAGTTCTTCAAAACC**GCC**GTGAATTTGGTGAACATCATTCC-3'
	R: 5'-GGAATGATGTTCACCAAATTCAC**GGC**GGTTTTGAAGAACTCCTC-3'
OAC Y27F	F: 5'-GAGGAGTTCTTCAAAACC**TTC**GTGAATTTGGTGAACATCATTCC-3'
	R: 5'-GGAATGATGTTCACCAAATTCAC**GAA**GGTTTTGAAGAACTCCTC-3'
OAC Y27L	F: 5'-GAGGAGTTCTTCAAAACC**CTC**GTGAATTTGGTGAACATCATTCC-3'
	R: 5'-GGAATGATGTTCACCAAATTCAC**GAG**GGTTTTGAAGAACTCCTC-3'
OAC Y27M	F: 5'-TGGAATGATGTTCACCAAATTCAC**CAT**GGTTTTGAAGAACTCCTCTTTCTG-3'
	R: 5'-CAGAAAGAGGAGTTCTTCAAAACC**ATG**GTGAATTTGGTGAACATCATTCCA-3'
OAC Y27W	F: 5'-GGAATGATGTTCACCAAATTCAC**CCA**GGTTTTGAAGAACTCCTCTTTC-3'
	R: 5'-GAAAGAGGAGTTCTTCAAAACC**TGG**GTGAATTTGGTGAACATCATTCC-3'
OAC V59A	F: 5'-GAAGGGTATACCCACATT**GCA**GAGGTAACGTTTGAAAGC-3'
	R: 5'-GCTTTCAAACGTTACCTC**TGC**AATGTGGGTATACCCTTC-3'
OAC V59F	F: 5'-GAAGAAGGGTATACCCACATT**TTT**GAGGTAACGTTTGAAAGCG-3'
	R: 5'-CGCTTTCAAACGTTACCTC**AAA**AATGTGGGTATACCCTTCTTC-3'
OAC V59I	F: 5'- GAAGAAGGGTATACCCACATT**ATC**GAGGTAACGTTTGAAAGCG-3'
	R: 5'-CGCTTTCAAACGTTACCTC**GAT**AATGTGGGTATACCCTTCTTC-3'
OAC V59L	F: 5'- GAAGGGTATACCCACATT**CTG**GAGGTAACGTTTGAAAGC-3'
	R: 5'- GCTTTCAAACGTTACCTC**GAC**AATGTGGGTATACCCTTC-3'
OAC V59M	F: 5'- GAAGGGTATACCCACATT**CAT**GAGGTAACGTTTGAAAGC-3'
	R: 5'- GCTTTCAAACGTTACCTC**ATG**AATGTGGGTATACCCTTC-3'
TKS L190G	F: 5' – TGCGACATTATGGCCTGC**GGA**TTTCGTGGCCCATCAGAG-3'
	R: 5'- CTCTGATGGGCCACGAAA**TCC**GCAGGCCATAATGTCGCA-3'

F, forward primer; R, reverse primer.
Mutated codons and overlapping sequences between each primer set are underlined and in bold font, respectively.

Expression and purification of OAC and its mutants

The *N*-terminally GST-tagged wild-type OAC and its mutants were expressed, extracted, and purified by the same procedure as used for the wild-type OAC for its crystallization[28], with some modifications. The *E. coli* M15 (pREP$_4$) cells harboring the wild-type OAC or its mutants with an *N*-terminal GST-tag were grown at 37 °C in LB medium, supplemented with 100 μg/mL ampicillin and 25 μg/mL kanamycin. When the OD$_{600}$ reached 0.6, the culture was cooled down to 17 °C. Isopropyl β-D-thiogalactopyranoside (IPTG) was added to each culture at a final concentration of 1 mM to express the GST-tagged wild-type OAC or its mutants, and the cultures were continued at 17 °C overnight. The cells were centrifuged at 5,000x *g* for 15 min at 4 °C, and the resulting cell pellets were stored at -80 °C. All the following procedures were performed at 4 °C. The cell pellets were suspended in buffer A [50 mM Tris-HCl (pH 8.0), 5%$_{v/v}$ glycerol, 2 mM DTT] containing 200 mM NaCl, and disrupted by ultrasonication. The resultant lysate was centrifugated at 12,000x *g* for 15 min, and the supernatant was loaded onto a COSMOGEL GST-Accept Resin column equilibrated with buffer A containing 50 mM NaCl. After the column was washed with buffer A containing 50 mM NaCl, the GST-tag was cleaved on the column by PSP (GE Healthcare) overnight, and then wild-type OAC or its mutants was eluted with buffer A containing 50 mM NaCl. The resultant protein thus contains three additional *N*-terminal residues (G-P-G) derived from the PSP recognition sequence. The eluted OAC was further purified by size-exclusion chromatography on a HiLoad 16/60 Superdex 200 pg column (Cytiva), eluted with buffer A containing 25 mM NaCl. Fractions containing wild-type OAC or its mutants were pooled and concentrated to 4.2 mg/mL. The purified OAC proteins were stored at -80 °C, and fresh aliquots were used for all OAC assays. The purities of the recombinant OAC and its mutants were estimated to be more than 95% by SDS-PAGE.

Crystallization of OAC F24I with 3b-analogs binary complex

The purified OAC F24I mutant (10 mg/mL) was mixed with 2 mM product (**3b**, **3c**, and **3d**). Crystals were grown using the vapor diffusion method at 4 °C in 1 μL sitting drops with 1:1 = sample:well solution ratios. Precipitants are listed in **Table 3**.

Data collection and structure refinement of OAC F24I with 3b-analogs binary complex

Crystals were cryo-protected using mother liquor supplemented with 30%$_{v/v}$ glycerol before cryo-cooling in liquid N_2. Data were collected at 100 K using synchrotron radiation at the Photon Factory (PF) beamlines BL-1A and BKL-17A. Data were indexed, integrated, and scaled using the XDS package[42] and AIMLESS[43] from the CCP4 program suite[44]. The OAC F24I crystal structures were determined by molecular replacement (MR), using the AutoMR (PHASER[45]) subroutine in PHENIX[46]. The search model used for MR was based on the OAC:**3b** structure (PDB ID 5B08[28]). The structural model was improved by iterative cycles of manual re-building in COOT[47] and crystallographic refinement in phenix.refine[48] (refinement details are summarized in Table 3). The crystal structure data of OAC-F24I:**3b**, OAC-F24I:**3c**, and OAC-F24I:**3d** have been deposited in the Protein Data Bank with the PDB accession codes 7W6D, 7W6E, and 7W6F, respectively. PyMOL[49] was used for the generation of graphical representations. Polder omit maps were calculated using Polder Maps[50] in PHENIX[46].

Table 3. Crystallization conditions, data collection, and refinement statistics for the OAC F24I complexes and TKS-L190G:**5e**.[a]

	OAC-F24I:**3b**	OAC-F24I:**3c**	OAC-F24I:**3d**	TKS-L190G:**5e**
PDB ID	7W6D	7W6E	7W6F	7W6G
Crystallization				
Precipitation conditions	0.1 M MES-NaOH (pH 6.5), 30%$_{w/v}$ PEG3350, 1.2%$_{v/v}$ (±)–1,3-butanediol	0.1 M HEPES (pH 7.5), 35%$_{w/v}$ PEG3350	0.1 M MES-NaOH (pH 6.5), 25%$_{w/v}$ PEG3350	0.2 M ammonium acetate, 20%$_{w/v}$ PEG3350
Data collection				
Space group	$P1$	$P1$	$P1$	$P1$
Symmetry	triclinic	triclinic	triclinic	triclinic
Cell dimensions:				
a, b, c (Å)	32.79, 39.43, 43.41	32.57, 39.45, 43.08	32.85, 39.32, 43.01	58.02, 66.93, 95.09
α, β, γ (°)	70.38, 75.48, 67.78	71.14, 76.50, 67.51	70.91, 76.38, 67.38	93.45, 102.11, 100.20
X-Ray source[b]	Synchrotron (PF BL-17A)	Synchrotron (PF BL-1A)	Synchrotron (PF BL-1A)	Synchrotron (PF BL-1A)
Resolution (Å)[c]	40.48-1.54 (1.57-1.54)	40.45-1.38 (1.40-1.38)	40.32-1.58 (1.61-1.58)	47.18-2.10 (2.14-2.10)
R_{merge}	0.059 (0.148)	0.042 (0.263)	0.048 (0.304)	0.112 (0.807)
$I / \sigma I$	10.0 (7.0)	14.3 (4.1)	9.4 (2.5)	4.8 (1.1)
CC (1/2)	0.996 (0.975)	0.999 (0.936)	0.998 (0.884)	0.993 (0.684)
Total number of reflections	105546 (5096)	147444 (7367)	89619 (4406)	273969 (16071)
Total number of unique reflections	26520 (1259)	36332 (1781)	24486 (1188)	78075 (4413)
Completeness (%)	95.4 (90.6)	94.8 (92.5)	96.0 (93.8)	97.6 (96.4)
Multiplicity	4.0 (4.0)	4.1 (4.1)	3.7 (3.7)	3.5 (3.6)
Refinement				
R_{work} / R_{free}	0.152 / 0.176	0.136 / 0.162	0.148 / 0.169	0.194 / 0.236
No. atoms:	4172	4276	3953	25007
B-factors:	19.0	17.0	19.0	23.2
R.m.s. deviations:				
Bond lengths (Å)	0.006	0.011	0.006	0.004
Bond angles (°)	0.918	1.125	1.007	0.617

[a]Experimental details are specified in the Supplementary Information (Experimental procedures);

[b]PF: Photon Factory; [c]Values in parentheses are for highest-resolution shell.

Construction of TKS and its L190G mutant

Each full-length cDNA of wild-type TKS was amplified from the previously reported pET22b expression plasmid encoding wild-type TKS as the template with the PCR method, using KOD-Plus-Neo (TOYOBO) and the pair of primers: TKS-F: 5'-TTCCAGGGCCCGGGAATGAACCACCTTCGTGCAGAAGGTCCAGCA-3' and TKS-R: 5'-GATTACCTATCTAGATCAATATTTGATCGGTACGGAGCGGACCAC-3' (*Sma*I and *Xba*I sites are underlined, respectively) and inserted into the *Sma*I/*Xba*I sites of the modified pCold II vector for expression as *N*-terminal GST-tag fusion proteins with a PSP (Amersham Biosciences) cleavage site (LEVLFQGP), using an In-Fusion cloning kit (Takara Bio) according to the manufacturer's protocol. After confirmation of the sequences, the plasmids were transformed into *E. coli* C43(DE3). The expression plasmid of the TKS L190G mutant was constructed with the QuickChange site-directed mutagenesis kit, using the aforementioned pCold II expression plasmid encoding wild-type TKS as the template and the pairs of primers listed in **Table 2**, according to the manufacturer's protocol.

Expression and purification of TKS and its L190G mutant

Each *N*-terminally GST-tagged wild-type TKS and its L190G mutant protein was expressed in *E. coli* C43(DE3) cells according to the same procedure as that for OAC, except for the use of an induction temperature of 15 °C and a final IPTG concentration of 0.5 mM. Cells were centrifuged at 6,500 rpm for 15 min, and the resulting cell pellets were stored at -80 °C. The purification of the wild-type TKS and its L190G mutant enzymes was performed according to the same procedure as that for the OAC. Purified TKS was stored at a concentration of 5 mg/mL in buffer A containing 25 mM NaCl at -80 °C, and fresh aliquots were used for all enzyme reactions. The purities of the recombinant TKS and its L190G mutant were estimated to be greater than 95% by SDS-PAGE.

Standard enzyme reaction and OACs and TKS or TKS L190G co-incubation assay

Stock solutions of hexanoyl-CoA (**5b**) and malonyl-CoA were prepared at 10 mM in water. Stock solutions of octanoyl-CoA (**5c**), decanoyl-CoA (**5d**), lauroyl-CoA (**5e**), and myristoyl-CoA (**5f**) were prepared at 10 mM in analytical-grade dimethyl sulfoxide (DMSO). The OAC and TKS enzyme assays were performed as previously described[6] with slight modifications. OAC or its mutants (30 μg) and 10 μg of TKS or its L190G mutant were co-incubated at 20 °C in a final volume of 500 μL reaction buffer (100 mM potassium phosphate buffer, pH 7.0) containing 100 μM malonyl-CoA and 60 μM fatty acyl-CoA (**5b**–**f**). After an incubation for 16 hours, the enzyme reaction was stopped by the addition of 50 μL of 20%$_{v/v}$ aqueous hydrochloric acid. The enzyme mixtures were extracted three times with 1.0 mL ethyl acetate, and the combined ethyl acetate layer was concentrated under reduced pressure. The residue was dissolved in 100 μL methanol and then subjected to the LC-ESI-MS analysis using a TSK-gel ODS-80Ts column (4.6 x 150 mm, TOSOH) at flow rate of 0.6 mL/min. Gradient elution was performed with water and methanol, both containing 0.1%$_{v/v}$ formic acid: 0–5 min, 60%; 5–7 min, 60-70%; 7–15 min, 70%; 15–70 min, 70–80%$_{v/v}$ methanol for enzyme reaction products from **5b**–**e**; 0-5 min, 60% methanol; 5–35 min, 60–100%; 35–45 min, 100%$_{v/v}$ methanol for enzyme reaction products from **5f**. Elutions were monitored with a 1260 Infinity II multichannel UV detector (Agilent), and UV spectra (190–400 nm) were recorded every 0.5 s. The ESI capillary temperature was 350 °C. The ESI capillary voltages were 3.5 kV and 1.5 kV for the positive and negative modes, respectively. All spectra were obtained in the positive mode over a mass range m/z of 50–500 and at a range of one scan every 0.1 s. The collision gas was nitrogen, and the relative collision energy scale was set at 10 eV. Each reaction was performed independently in triplicate. The boiled TKS and OAC enzymes were used as controls. The peak area data of **3** at 260 nm on the HPLC elution profile obtained from each enzyme reaction was employed to quantify the production of **3**, using standard curves of authentic **3b**–**e**. Each sample was analyzed independently in triplicate. The enzyme reaction products **3**, **4**, **6**, and **7** observed in the reaction mixture were identified by comparing their ESI-MS, MS/MS, UV spectra data, and retention time on HLPC with those of the authentic compounds (**Figs. 20–**

23). Authentic compounds **3c**–**e** and **4c** were synthesized as previously described. Authentic compounds **6b**–**e** and **7b**–**e** were prepared by using *Arabidopsis thaliana* PKS-A, the type III PKS that has been reported to produce **6b**–**e** and **7b**–**e** pyrones. *A. thaliana* PKS-A was prepared as described below.

LCMS data of 9

Compound 9b

HRMS (ESI) *m/z*: [M - H]⁻ Calcd for $C_{14}H_{17}O_5$ 265.1081; Found 265.1079. HRMS/MS (ESI) *m/z*: [M - H - CO_2]⁻ Calcd for $C_{13}H_{17}O_3$ 221.1178; Found 221.1178, [M - $C_7H_{11}O_3$]⁻ Calcd for $C_7H_7O_2$ 123.0446; Found 123.0443.

Compound 9c

HRMS (ESI) *m/z*: [M - H]⁻ Calcd for $C_{16}H_{21}O_5$ 294.1394; Found 293.1388. HRMS/MS (ESI) *m/z*: [M - H - CO_2]⁻ Calcd for $C_{15}H_{21}O_3$ 249.1491; Found 249.1498, [M - $C_9H_{15}O_3$]⁻ Calcd for $C_7H_7O_2$ 123.0446; Found 123.0450.

Compound 9d

HRMS (ESI) *m/z*: [M - H]⁻ Calcd for $C_{18}H_{25}O_5$ 321.1707; Found 321.1708. HRMS/MS (ESI) *m/z*: [M - H - CO_2]⁻ Calcd for $C_{17}H_{25}O_3$ 277.1804; Found 277.1817, [M - $C_{11}H_{19}O_3$]⁻ Calcd for $C_7H_7O_2$ 123.0446; Found 123.0437.

Compound 9e

HRMS (ESI) *m/z*: [M - H]⁻ Calcd for $C_{20}H_{29}O_5$ 349.2020; Found 349.2002. HRMS/MS (ESI) *m/z*: [M - H - CO_2]⁻ Calcd for $C_{19}H_{29}O_3$ 305.2117; Found 305.2115, [M - $C_{13}H_{23}O_3$]⁻ Calcd for $C_7H_7O_2$ 123.0446; Found 123.0446.

Crystallization analyses of TKS L190G

The purified TKS L190G mutant (20 mg/mL) was mixed with 2 mM lauroyl-CoA (**5e**). Crystals were grown using the vapor diffusion method at 4 °C in 1 μL sitting drops with 1:1 = sample:well solution ratios. Precipitants are listed in Table 3. Crystals were cryo-protected using mother liquor supplemented with 20%$_{v/v}$ glycerol before cryo-cooling in liquid N_2. Data were collected at 100 K using synchrotron radiation at the PF beamline BL-1A. Data were indexed, integrated, and scaled using the XDS package[42] and AIMLESS[43] from the CCP4 program suite[44]. The TKS L190G crystal structures were determined by MR, using the AutoMR (PHASER[45]) subroutine in PHENIX[46]. The search model used for MR was based on the TKS:CoA-SH structure (PDB ID 6GW3[31]). The structural model was improved by iterative cycles of manual re-building in COOT[47] and crystallographic refinement in phenix.refine[48] (refinement details are summarized in Table 3). The crystal structure data of the TKS-L190G:**5e** complex have been deposited in the Protein Data Bank with the PDB accession code 7W6G. PyMOL[49] was used for the generation of graphical representations, and polder omit maps were calculated using Polder Maps[50] in PHENIX[46].

Construction of PKS-A plasmid and the expression and purification of PKS-A

The full-length *Atlg02050* cDNA was amplified from an *A. thaliana* cDNA library (Invitrogen) using the following pair of primers: PKS-A-F: 5'-TTCCAGGG<u>CCCGGG</u>AATGTCGAATTCTAGGATGAATGGTGTTGAG-3' and PKS-A-R: 5'-TGGCTGCAG<u>GTCGAC</u>TTAGGAAGAGGTGAGGCTGCGGATGA GAAG-3' (*Sma*I and *Sal*I sites are underlined, respectively). The cDNA was inserted into the *Sma*I/*Sal*I sites of the modified pQE-80L vector for expression as an *N*-terminal GST-tag fusion protein, using an In-Fusion cloning kit (Takara Bio) according to the manufacturer's protocol. After sequence confirmation, the plasmid was transformed into *E. coli* M15 (pREP4). The *N*-terminally GST-tagged PKS-A was expressed in *E. coli* M15 (pREP4) cells and purified according to the same procedure as that for TKS. Purified PKS-A was stored at a concentration of 4.2 mg/mL in buffer A containing 25 mM NaCl at -80 °C, and fresh aliquots were used for all enzyme

reactions. The purity of the recombinant PKS-A was estimated to be greater than 95% by SDS-PAGE.

Construction of NphB G286S/Y288A mutant plasmid

A modified pQE80L vector (Qiagen) for expression as an *N*-terminal glutathione *S*-transferase (GST) fusion protein with a PSP (Amersham Biosciences) cleavage site (LEVLFQGP) was linearized by PCR, using KOD-Plus-Neo DNA Polymerase (Toyobo) and the pair of primers: 5′-<u>GTCGACCTGCAGCCA</u> AGCTTAATTAGCTGC-3′ as the sense primer, and 5′-<u>TCCCGGGCCCTGGAA</u> CAGAACTTCCAGAT-3′ as the antisense primer (the 15 bp sequences overlapping with those of primers used for the amplification of the NphB G286S/Y288A DNA fragment are underlined). The full-length cDNA encoding the NphB G286S/Y288A mutant was synthesized by Integrated DNA Technologies, and served as a template to amplify the cDNA fragment of the mutant by PCR, using <u>TTCCAGGGCCCGGG</u> ATGAGCGAAGCGGCGGATGTGGAACGTGTG-3′ as the sense primer, and 5′-<u>TGGCTGCAGGTCGAC</u>TTAATCTTCCAGCGAATCAAAC GCTTTCAG-3′ as the antisense primer. The amplified mutant cDNA fragments were connected by using an In-Fusion HD cloning kit (Clontech), according to the manufacturer's protocol. After confirmation of the sequences, the resultant expression plasmid (pQE-GSTNphB G286S/Y288A) was transformed into *E. coli* M15 (pREP$_4$). The cells harboring the plasmid were cultured to an OD_{600} of 0.6 in LB medium, containing ampicillin (100 μg/mL) and kanamycin (25 mg/mL) at 25 °C. IPTG was then added to a final concentration of 0.5 mM to induce gene expression, and the culture was incubated further at 16 °C for 16 h.

Expression and purification of NphB G286S/Y288A mutant

All the following procedures were performed at 4 °C. In brief, the *E. coli* cells were harvested by centrifugation at 5,000x *g* and resuspended in 50 mM Tris-HCl buffer (pH 8.0), containing 0.2 M NaCl, 10%$_{v/v}$ glycerol and 2 mM DTT (buffer A). The cells were disrupted by sonication, and the lysate was centrifuged at 12,000x *g* for 30 min. The supernatant was loaded onto a Glutathione Sepharose 4B affinity column

(GE Healthcare) equilibrated with buffer A, and the column was then washed with buffer A. The GST-tag was cleaved on the column overnight by PSP, and then the recombinant NphB G286S/Y288A was eluted with buffer A. The resultant NphB G286S/Y288A thus contains three additional residues (G-P-G) at the *N*-terminal flanking region, derived from the PSP recognition sequence. After five-fold dilution of the protein solution with 20 mM Tris-HCl buffer (pH 8.0), containing 10%$_{v/v}$ glycerol, 25 mM NaCl, and 2 mM DTT, the protein solution containing the NphB G286S/Y288A mutant was further purified to homogeneity by chromatography on a HiLoad 16/60 Superdex 200 column (GE Healthcare). The peak fractions were concentrated to 10 mg/mL in 20 mM Tris-HCl buffer (pH 8.0) buffer, containing 25 mM NaCl and 2 mM DTT.

Preparation of 1a–f, 3a–f, and 4a–f

Compounds **1a–f**, **3a–f**, and **4a–f** were synthesized according to the published methods.[34, 35, 51]

Synthesis of 1a–f

To a solution of geraniol (**2**,173.5 µL, 1.0 mmol) and 1.5 mmol of 5-propylbenzene-1,3-diol (**4a**, 152.3 mg) or olivetol (**4b**, 270.4 mg) or spherophorol (**4c**, 312.5 mg) or 5-nonylbenzene-1,3-diol (**4d**, 354.5 mg) or 5-undecylbenzene-1,3-diol (**4e**, 396.6 mg) or grevillol (**4f**, 438.7 mg) in DCE (5 mL) was added acidic alumina (2.0 g). The heterogeneous mixture was stirred at reflux temperature for 6 h, then cooled to ambient temperature, and filtered through a Celite plug. The filter cake was rinsed with EtOAc (3 × 10 mL portions), and the filtrate was concentrated in vacuo to afford a yellow oil. This residue was purified via chromatography using silica gel eluted with hexanes and EtOAc. Product-rich fractions were pooled and evaporated to afford **1a–f**, respectively.

Cannabigerovarin (1a)

Yellow oil (2.1 mg, Yield 2.1%); ^{1}H NMR (400 MHz, CDCl$_3$): δ_H 6.25 (2H, s), 5.28 (1H, t, *J* = 6.9 Hz), 5.05 (1H, m), 5.01 (2H, br s), 3.38 (2H, d, *J* = 6.9 Hz), 2.44 (2H, t, *J* = 7.8 Hz), 2.12–2.01 (4H, m), 1.81 (3H, s), 1.67 (3H, s), 1.62–1.52 (2H, m), 1.59

(3H, s), 0.92 (3H, t, J = 7.3 Hz); ^{13}C NMR (100 MHz, CDCl$_3$) δ_C 154.8, 142.5, 139.0, 132.1, 123.7, 121.7, 110.6, 108.4, 39.7, 37.6, 26.4, 25.7, 24.2, 22.2, 17.7, 16.2, 13.8; HRMS (ESI) m/z: [M - H]$^-$ Calcd. for C$_{19}$H$_{27}$O$_2$ 287.2017; Found 287.2017.

Cannabigerol (1b)

Yellow oil (32.1 mg, Yield 12%) as yellow oil ; ^{1}H NMR (400 MHz, CDCl$_3$): δ_H 6.26 (2H, s), 5.28 (1H, t, J = 6.9 Hz), 5.07 (1H, t, J = 6.4 Hz), 3.40 (2H, d, J = 6.9 Hz), 2.45 (2H, t, J = 7.8 Hz), 2.12–2.01 (4H, m), 1.82 (3H, s), 1.69 (3H, s), 1.62–1.52 (2H, m), 1.60 (3H, s), 1.37–1.24 (4H, m), 0.92 (3H, t, J = 6.9 Hz); ^{13}C NMR (100 MHz, CDCl$_3$) δ_C 154.8, 142.7, 138.9, 132.0, 123.7, 121.7, 110.6, 108.3, 39.7, 35.5, 31.5, 30.8, 26.3, 25.6, 22.5, 22.2, 17.6, 16.1, 14.0; HRMS (ESI) m/z: [M - H]$^-$ Calcd. for C$_{21}$H$_{31}$O$_2$ 315.2330; Found 315.2302.

Cannabigerophorol (1c)

Yellow oil (2.4 mg, Yield 2%); ^{1}H NMR (400 MHz, CDCl$_3$): δ_H 6.25 (2H, s), 5.28 (1H, t, J = 6.9 Hz), 5.07 (1H, t, J = 6.9 Hz), 3.40 (2H, d, J = 6.9 Hz), 2.45 (2H, t, J = 7.4 Hz), 2.12–2.01 (4H, m), 1.81 (3H, s), 1.69 (3H, s), 1.62–1.52 (2H, m), 1.60 (3H, s), 1.37–1.24 (8H, m), 0.90 (3H, t, J = 6.9 Hz); ^{13}C NMR (100 MHz, CDCl$_3$) δ_C 154.8, 142.6, 138.8, 132.0, 123.7, 121.8, 110.7, 108.3, 39.6, 35.5, 31.8, 31.1, 29.3, 29.2, 26.3, 25.6, 22.6, 22.2, 17.6, 16.1, 14.1; HRMS (ESI) m/z: [M - H]$^-$ Calcd. for C$_{23}$H$_{35}$O$_2$ 343.2643; Found 343.2649.

(*E*)-2-(3,7-Dimethylocta-2,6-dien-1-yl)-5-nonylbenzene-1,3-diol (1d)

Yellow oil (30.5 mg, Yield 3%); ^{1}H NMR (400 MHz, CDCl$_3$): δ_H 6.25 (2H, s), 5.28 (1H, t, J = 7.3 Hz), 5.14 (2H, br s), 5.06 (1H, t, J = 6.9 Hz), 3.40 (2H, d, J = 6.9 Hz), 2.45 (2H, t, J = 7.8 Hz), 2.12–2.05 (4H, m), 1.82 (3H, s), 1.68 (3H, s), 1.62–1.52 (2H, m), 1.60 (3H, s), 1.37–1.24 (12H, m), 0.89 (3H, t, J = 6.9 Hz); ^{13}C NMR (100 MHz, CDCl$_3$) δ_C 154.8, 142.7, 138.9, 132.0, 123.7, 121.7, 110.6, 108.3, 39.7, 35.5, 31.9, 31.1, 29.5 29.3, 26.4, 25.6, 22.7, 22.2, 17.6, 16.2, 14.1; HRMS (ESI) m/z: [M - H]$^-$ Calcd. for C$_{25}$H$_{39}$O$_2$ 371.2956; Found 371.2942.

(*E*)-2-(3,7-Dimethylocta-2,6-dien-1-yl)-5-undecylbenzene-1,3-diol (1e)

Yellow solid (16.8 mg, Yield 3%); ^{1}H NMR (400 MHz, CDCl$_3$): δ_H 6.25 (2H, s), 5.28 (1H, t, *J* = 6.9 Hz), 5.09 (2H, br s), 5.06 (1H, t, *J* = 6.5 Hz), 3.39 (2H, d, *J* = 6.9 Hz), 2.45 (2H, t, *J* = 7.8 Hz), 2.12–2.05 (4H, m), 1.81 (3H, s), 1.68 (3H, s), 1.62–1.52 (2H, m), 1.59 (3H, s), 1.37–1.24 (16H, m), 0.89 (3H, t, *J* = 6.9 Hz); ^{13}C NMR (100 MHz, CDCl$_3$) δ_C 154.8, 142.7, 138.9, 132.0, 123.7, 121.7, 110.6, 108.3, 39.7, 35.5, 31.9, 31.1, 29.7, 29.62, 29.58, 29.5, 29.3, 26.4, 25.6, 22.7, 22.2, 17.7, 16.2, 14.1; HRMS (ESI) *m/z*: [M - H]$^-$ Calcd. for C$_{27}$H$_{43}$O$_2$ 399.3269; Found 399.3266.

(*E*)-2-(3,7-Dimethylocta-2,6-dien-1-yl)-5-tridecylbenzene-1,3-diol (1f)

Yellow solid (28.3 mg, Yield 5.7%); ^{1}H NMR (400 MHz, CDCl$_3$): δ_H 6.25 (2H, s), 5.28 (1H, t, *J* = 6.9 Hz), 5.11 (2H, br s), 5.06 (1H, t, *J* = 6.9 Hz), 3.39 (2H, d, *J* = 6.9 Hz), 2.45 (2H, t, *J* = 7.8 Hz), 2.12–2.05 (4H, m), 1.81 (3H, s), 1.68 (3H, s), 1.62–1.52 (2H, m), 1.60 (3H, s), 1.37–1.24 (20H, m), 0.89 (3H, t, *J* = 6.9 Hz); ^{13}C NMR (100 MHz, CDCl$_3$) δ_C 154.8, 142.7, 139.0, 132.0, 123.7, 121.7, 110.6, 108.3, 39.7, 35.5, 31.9, 31.1, 29.7, 29.6, 29.5, 29.3, 26.4, 25.7, 22.7, 22.2, 17.7, 16.2, 14.1; HRMS (ESI) *m/z*: [M - H]$^-$ Calcd. for C$_{29}$H$_{47}$O$_2$ 427.3582; Found 427.3583.

Synthesis of 3a–f

Briefly, 10 mL of dry THF was added and cooled to 0 °C over an ice bath and kept under argon condition. To this chilled solvent, (i-Pr)$_2$NH (0.07 mL, 7.14 mmol) and 2.5 M *n*-BuLi (2.85 mL, 7.14 mmol) was added. The mixture was then cooled to -78 °C. 2,4-dimethoxy-6-methylbenzoic acid (0.35 g, 1.78 mmol) dissolved in 5 mL of THF was then added and stirred for 30 min. Long-chain alkyl bromides (7.14 mmol) were then added and stirred at r.t. for 2 hr. The reaction mixture was then acidified with HCl to pH 1 and extracted with EtOAc. The organic phase was combined and dried for the next step. The product from previous step was dissolved in 10 mL DCM and cooled to -78 °C. 1 M BBr$_3$ (11.3 mL, 11.3 mmol) was added dropwise and stirred at r.t overnight. The reaction mixture was then extracted with DCM and washed with sodium bicarbonate. The sodium bicarbonate layer was then acidified to pH 1 and further extracted with DCM. The organic phases were then pooled and subjected to

silica gel column chromatography eluted with hexanes and EtOAc. Product-rich fractions were pooled and evaporated to afford **3a–f**, respectively.

Divaric acid (3a)

White solid (10.4 mg, yield 8.7%); ^{1}H NMR (500 MHz, DMSO-d_6): δ_H 10.03 (1H, br s), 6.14 (1H, d, J = 2.3 Hz), 6.11 (1H, d, J = 2.3 Hz), 2.71 (2H, t, J = 7.5 Hz), 1.48 (2H, m), 0.87 (3H, t, J = 7.5 Hz); ^{13}C NMR (125 MHz, DMSO-d_6): δ_C 172.7, 163.5, 161.5, 146.8, 110.0, 105.3, 100.6, 37.4, 24.4, 14.1; HRMS (ESI) m/z: [M - H]$^-$ Calcd. for $C_{10}H_{11}O_4$ 195.0663; Found 195.0666.

Phorolic acid (3c)

White solid (62 mg, yield 48%); ^{1}H NMR (500 MHz, DMSO-d_6) δ_H 10.01 (1H, br s), 6.15 (1H, d, J = 2.3 Hz), 6.12 (1H, d, J = 2.3 Hz), 2.74 (2H, t, J = 7.4 Hz), 1.47 (2H, m), 1.30–1.18 (8H, m), 0.85 (3H, t, J = 6.9 Hz); ^{13}C NMR (125 MHz, DMSO-d_6) δ_C 172.7, 163.5, 161.5, 147.1, 110.0, 105.2, 100.5, 35.3, 31.3, 31.2, 29.1, 28.5, 22.1, 13.9; HRMS (ESI) m/z: [M - H]$^-$ Calcd for $C_{14}H_{19}O_4$ 251.1289; Found 251.1284.

2,4-Dihydroxy-6-heptylbenzoic acid (3d)

White solid (51 mg, yield 36%); ^{1}H NMR (500 MHz, DMSO-d_6) δ_H 10.02 (1H, br s), 6.15 (1H, d, J = 2.0 Hz), 6.12 (1H, d, J = 2.0 Hz), 2.74 (2H, t, J = 7.6 Hz), 1.49 (2H, m), 1.30–1.18 (12H, m), 0.85 (3H, t, J = 7.6 Hz); ^{13}C NMR (125 MHz, DMSO-d_6) δ_C 172.8, 163.6, 161.6, 147.2, 110.0, 105.2, 100.5, 35.4, 31.4, 31.3, 29.2, 29.0, 28.9, 28.7, 22.1, 14.0; HRMS (ESI) m/z: [M - H]$^-$ Calcd for $C_{16}H_{23}O_4$ 279.1602; Found 279.1601.

2,4-Dihydroxy-6-undecylbenzoic acid (3e)

White solid (31 mg, yield 20%); ^{1}H NMR (500 MHz, DMSO-d_6) δ_H 10.03 (1H, br s), 6.14 (1H, d, J = 2.1 Hz), 6.11 (1H, d, J = 2.1 Hz), 2.73 (2H, t, J = 7.5 Hz), 1.46 (2H, m), 1.30–1.18 (16H, m), 0.85 (3H, t, J = 8.7 Hz); ^{13}C NMR (125 MHz, DMSO-d_6) δ_C 172.7, 163.6, 161.6, 147.1, 110.0, 105.2, 100.5, 35.4, 31.35, 31.32, 29.2, 29.1, 29.0, 28.9, 28.7, 22.1, 14.0; HRMS (ESI) m/z: [M - H]$^-$ Calcd for $C_{16}H_{27}O_4$ 307.1915; Found 307.1917.

2,4-Dihydroxy-6-tridecylbenzoic acid (3f)

White solid (20.4 mg, yield 14%); ^{1}H NMR (500 MHz, DMSO-d_6): δ_H 9.99 (1H, br s), 6.13 (1H, d, J = 2.3 Hz), 6.10 (1H, d, J = 2.3 Hz), 2.72 (2H, t, J = 7.5 Hz), 1.46 (2H, m), 1.30–1.19 (20H, m), 0.84 (3H, t, J = 6.9 Hz); ^{13}C NMR (125 MHz, DMSO-d_6): δ_C 172.6, 163.5, 161.5, 147.1, 109.9, 105.3, 100.5, 35.3, 31.29, 31.26, 29.1, 29.00, 28.98, 28.8, 28.7, 22.1, 13.9; HRMS (ESI) m/z: [M - H]$^-$ Calcd. for $C_{20}H_{31}O_4$ 335.2228; Found 335.2255.

Synthesis of 4a–f

Briefly, a solution of PPh$_3$ (1.2 equiv) and long-chain alkyl bromides (1.0 equiv) in toluene (10 mL) was heated to reflux overnight. After being cooled to room temperature, hexane (10 mL) was added. The mixture was filtered, and the solid was washed with a mixture of hexane/ethyl acetate (10:1) three times. The solid was then dried in vacuo to give the alkyltriphenylphosphonium salts. To a solution of 3,5-dimethoxybenzaldehyde (1.0 equiv) and alkyltriphenylphosphonium salts (1.2 equiv) in DMSO/H$_2$O (10:1) at room temperature was added potassium carbonate (2.0 equiv). The mixture was heated to reflux overnight. After being cooled to room temperature, the mixture was poured into water, and extracted with EtOAc. The organic layers were combined, washed with water and brine, dried over Na$_2$SO$_4$, and filtered. The filtrate was concentrated under reduced pressure to give a red residue, which was subjected to column chromatography (CC) (hexane/ethyl acetate = 40:1) on silica gel to produce the **4a–f**.

5-Propylbenzene-1,3-diol (4a)

White solid (126.5 mg, yield 88.3%); ^{1}H NMR (500 MHz, CDCl$_3$): δ_H 6.25 (2H, d, J = 2.3 Hz), 6.18 (1H, t, J = 2.3 Hz), 2.45 (2H, t, J = 7.5 Hz), 1.57 (2H, td, J = 15.2, 7.5 Hz), 0.91 (3H, t, J = 7.5 Hz); ^{13}C NMR (125 MHz, CDCl$_3$): δ_C 156.4, 146.0, 108.2, 100.2, 37.9, 24.1, 13.8; HRMS (ESI) m/z: [M - H]$^-$ Calcd. for $C_{13}H_{19}O_2$ 151.0765; Found 151.0785.

Spherophorol (4c)

White solid (232 mg, yield 68%); ^{1}H NMR (500 MHz, CDCl$_3$) δ_H 7.07 (2H, br s,), 6.26 (2H, d, J = 2.3 Hz), 6.17 (1H, t, J = 2.3 Hz), 2.39 (2H, t, J = 8.0 Hz), 1.44 (2H, m), 1.28–1.18 (8H, m), 0.85 (3H, t, J = 8.0 Hz); ^{13}C NMR (125 MHz, CDCl$_3$) δ_C 155.8, 146.5, 108.4, 100.3, 35.8, 31.8, 31.0, 29.3, 29.2, 22.6, 14.0; HRMS (ESI) m/z: [M - H]$^-$ Calcd for C$_{13}$H$_{19}$O$_2$ 207.1391; Found 207.1378.

5-Nonylbenzene-1,3-diol (4d)

White solid (21.5 mg, yield 11%); ^{1}H-NMR (500 MHz, CDCl$_3$) δ_H 6.24 (2H, s), 6.17 (1H, s), 2.50-2.47 (2H, m), 1.28 (14H, m), 0.88 (3H, q, J = 3.4 Hz,); ^{13}C-NMR (125 MHz, CDCl$_3$) δ_C 156.7, 146.5, 108.2, 100.3, 36.0, 32.1, 31.3, 29.7, 29.5, 22.9, 14.3; HRMS (ESI) m/z: [M - H]$^-$ Calcd for C$_{15}$H$_{24}$O$_2$ 235.1776; Found 235.1721.

5-Undecylbenzene-1,3-diol (4e)

White solid (43.2 mg, yield 22%); ^{1}H NMR (500 MHz, CDCl$_3$) δ_H 6.24 (2H, d, J = 2.3 Hz), 6.17 (1H, t, J = 2.0 Hz), 2.48 (2H, t, J = 7.7 Hz), 1.27 (18H, m), 0.88 (3H, t, J = 6.9 Hz); ^{13}C-NMR (125 MHz, CDCl$_3$) δ_C 156.7, 146.4, 108.2, 100.3, 36.0, 32.1, 31.2, 29.9, 29.8, 29.8, 29.7, 29.5, 29.5, 22.9, 14.3; HRMS (ESI) m/z: [M - H]$^-$ Calcd for C$_{17}$H$_{28}$O$_2$ 263.2089; Found 263.2012.

Grevillol (4f)

White solid (176,1 mg, yield 38%); ^{1}H NMR (500 MHz, CDCl$_3$): δ_H 6.24 (2H, d, J = 1.7 Hz), 6.17 (1H, t, J = 2.3 Hz), 2.48 (2H, t, J = 7.5 Hz), 1.58 (2H, m), 1.30–1.23 (20H, m), 0.88 (3H, t, J = 7.5 Hz); ^{13}C NMR (125 MHz, CDCl$_3$): δ_C 156.5, 146.2, 108.0, 100.1, 35.8, 31.9, 31.1, 29.7, 29.6, 29.5, 29.4, 29.3, 22.7, 14.1; HRMS (ESI) m/z: [M - H]$^-$ Calcd. for C$_{19}$H$_{31}$O$_2$ 291.2330; Found 291.2318.

Synthesis of 2a–f using NphB G286S/Y288A

In a final volume of 20 mL, 2 mM **3a**–**f** were incubated in an enzyme reaction mixture containing 50 mM HEPES (pH 7.5), with 5 mM MgCl$_2$, 2 mM GPP, and 0.5 mg/mL purified NphB G286S/Y288A, according to the previously reported method

with some modifications.[39] The reaction mixtures were then incubated at 25 °C and extracted with ethyl acetate for three times. The organic layers were pooled and evaporated to yield **2a–f**. The compounds were further purified using an Agilent Infinity II 1260 HPLC system coupled with a TSK-gel ODS-80Ts column (4.6 x 150 mm, TOSOH) (flow rate: 0.6 mL/min; mobile phase, water and acetonitrile, both containing $0.1\%_{v/v}$ trifluoracetic acid; 0–1 min: 50%, 1–30 min: 50 to $100\%_{v/v}$ acetonitrile; UV: 260 nm or 280 nm). The purity of all the compounds used for the antibacterial assay were estimated based on their peak areas on the HPLC chromatograms, using a Agilent Infinity II 1260 HPLC system coupled with a TSK-gel ODS-80Ts column (4.6 x 150 mm, TOSOH) (Flow rate, 0.6 mL/min; mobile phase, water and acetonitrile, both containing 0.1% trifluoracetic acid; 0–1 min: 50%, 1–30 min: 50 to 100% acetonitrile; UV: 260 nm or 280 nm).

Cannabigerovarinic acid (2a)

White solid (2.2 mg, yield 13%); ^{1}H NMR (400 MHz, CDCl$_3$): δ_H 6.27 (1H, s), 5.28 (1H, t, J = 7.0 Hz), 5.05 (1H, t, J = 6.4 Hz), 3.43 (2H, d, J = 6.9 Hz), 2.87 (2H, t, J = 7.8 Hz), 2.12–2.04 (4H, m), 1.81 (3H, s), 1.67 (3H, s), 1.66–1.56 (2H, m), 1.59 (3H, s), 0.96 (3H, t, J = 7.3 Hz); ^{13}C NMR (100 MHz, CDCl$_3$) δ_C 175.0, 163.6, 160.4, 146.9, 139.2, 132.0, 123.7, 121.3, 111.5, 111.3, 103.1, 39.7, 38.6, 26.3, 25.7, 24.8, 22.1, 17.7, 16.2, 14.3; HRMS (ESI) m/z: [M - H]$^-$ Calcd. for C$_{20}$H$_{27}$O$_4$ 331.1915; Found 331.1910.

Cannabigerolic acid (2b)

White solid (2.0 mg, yield 41%); ^{1}H NMR (400 MHz, CDCl$_3$) δ_H 6.28 (1H, s), 5.28 (1H, t, J = 7.3 Hz), 5.05 (1H, t, J = 6.4 Hz), 3.43 (2H, d, J = 7.3 Hz), 2.88 (2H, t, J = 7.8 Hz), 2.12–2.05 (4H, m), 1.81 (3H, s), 1.67 (3H, s), 1.66–1.56 (2H, m), 1.59 (3H, s), 1.35–1.25 (4H, m), 0.90 (3H, t, J = 6.9 Hz); ^{13}C NMR (100 MHz, CDCl$_3$) δ_C 174.6, 163.6, 160.5, 147.4, 139.2, 132.0, 123.7, 121.3, 111.5, 111.2, 103.1, 39.7, 36.5, 32.0, 31.4, 26.3, 25.7, 22.5, 22.1, 17.7, 16.2, 14.0; HRMS (ESI) m/z: [M - H]$^-$ Calcd. for C$_{22}$H$_{31}$O$_4$ 359.2228; Found 359.2229.

Cannabigerophorolic acid (2c)

White solid (7.3 mg, yield 35%); ^{1}H NMR (400 MHz, CDCl$_3$): δ_H 11.90 (1H, s), 6.28 (1H, s), 5.28 (1H, t, J = 6.0 Hz), 5.05 (1H, t, J = 6.9 Hz), 3.43 (2H, d, J = 6.9 Hz), 2.89 (2H, t, J = 7.8 Hz), 2.12–2.05 (4H, m), 1.82 (3H, s), 1.67 (3H, s), 1.66–1.56 (2H, m), 1.59 (3H, s), 1.39–1.20 (8H, m), 0.88 (3H, t, J = 6.9 Hz); ^{13}C NMR (100 MHz, CDCl$_3$) δ_C 175.9, 163.6, 160.6, 147.5, 139.2, 132.1, 123.7, 121.3, 111.5, 111.3, 103.1, 39.7, 36.6, 31.8, 31.7, 29.8, 29.1, 26.3, 25.7, 22.7, 22.1, 17.7, 16.2, 14.1; HRMS (ESI) m/z: [M - H]$^-$ Calcd. for C$_{24}$H$_{35}$O$_4$ 387.2541; Found 387.2549.

(*E*)-3-(3,7-Dimethylocta-2,6-dien-1-yl)-2,4-dihydroxy-6-nonylbenzoic acid (2d)

White solid (4.6 mg, yield 31%); ^{1}H NMR (400 MHz, CDCl$_3$): δ_H 11.95 (1H, s), 6.27 (1H, s), 5.28 (1H, t, J = 6.9 Hz), 5.05 (1H, t, J = 6.9 Hz), 3.43 (2H, d, J = 6.9 Hz), 2.88 (2H, t, J = 7.6 Hz), 2.12–2.05 (4H, m), 1.81 (3H, s), 1.67 (3H, s), 1.62–1.52 (2H, m), 1.59 (3H, s), 1.39–1.20 (12H, m), 0.88 (3H, t, J = 6.9 Hz); ^{13}C NMR (100 MHz, CDCl$_3$) δ_C 175.9, 163.6, 160.5, 147.5, 139.2, 132.0, 123.7, 121.3, 111.5, 111.3, 103.1, 39.7, 36.6, 31.9, 31.7, 29.8, 29.6, 29.5, 29.3, 26.4, 25.7, 22.7, 22.1, 17.7, 16.2, 14.1; HRMS (ESI) m/z: [M - H]$^-$ Calcd. for C$_{26}$H$_{39}$O$_4$ 415.2854; Found 415.2867.

(*E*)-3-(3,7-Dimethylocta-2,6-dien-1-yl)-2,4-dihydroxy-6-undecylbenzoic acid (2e)

White solid (2 mg, yield 11%); ^{1}H NMR (400 MHz, CDCl$_3$): δ_H 11.92 (1H, s), 6.28 (1H, s), 5.28 (1H, t, J = 6.8 Hz), 5.05 (1H, t, J = 7.8 Hz), 3.43 (2H, d, J = 7.3 Hz), 2.88 (2H, t, J = 7.3 Hz), 2.12–2.05 (4H, m), 1.81 (3H, s), 1.67 (3H, s), 1.62–1.52 (2H, m), 1.59 (3H, s), 1.39–1.20 (16H, m), 0.87 (3H, t, J = 6.9 Hz); ^{13}C NMR (100 MHz, CDCl$_3$) δ_C 175.9, 163.6, 160.5, 147.8, 139.2, 132.1, 123.7, 121.3, 111.5, 111.3, 103.1, 39.7, 36.6, 31.9, 31.8, 29.8, 29.70, 29.66, 29.6, 29.5, 29.4, 26.4, 25.7, 22.7, 22.1, 17.7, 16.2, 14.1; HRMS (ESI) m/z: [M - H]$^-$ Calcd. for C$_{28}$H$_{43}$O$_2$ 443.3167; Found 443.3179.

(*E*)-3-(3,7-Dimethylocta-2,6-dien-1-yl)-2,4-dihydroxy-6-tridecylbenzoic acid (2f)

White solid (1.6 mg, yield 9%); ^{1}H NMR (400 MHz, CDCl$_3$) δ_H 6.27 (1H, s), 5.28 (1H, t, J = 6.4 Hz), 5.05 (1H, t, J = 6.9 Hz), 3.43 (2H, d, J = 7.3 Hz), 2.88 (2H, t, J = 7.8 Hz), 2.12–2.05 (4H, m), 1.81 (3H, s), 1.67 (3H, s), 1.62–1.52 (2H, m), 1.59 (3H, s), 1.39–1.20 (20H, m), 0.87 (3H, t, J = 7.3 Hz); ^{13}C NMR (100 MHz, CDCl$_3$) δ_C 175.2,

163.6, 160.5, 147.3, 139.2, 132.1, 123.7, 121.3, 111.4, 111.2, 103.1, 39.7, 36.6, 31.9, 31.8, 29.83, 29.77, 29.70, 29.66, 29.6, 29.5, 29.4, 26.3, 25.7, 22.7, 22.1, 17.7, 16.2, 14.1; HRMS (ESI) *m/z*: [M - H]$^-$ Calcd. for $C_{30}H_{47}O_4$ 471.3480; Found 471.3467.

Antibacterial assays

The antibacterial activities against Gram-positive bacteria (*S. aureus* NBRC 100910 and *B. subtilis* NBRC 13719) and Gram-negative bacteria: *K. pneumoniae* and *E. coli* were performed using an MTT assay according to the previously published protocol, with slight modifications.[52] The bacterial strains were inoculated on YP agar plates [1%$_{v/v}$ polypeptone (Nihon Pharmaceutical, Tokyo, Japan), 0.2%$_{w/v}$ yeast extract (Difco Laboratories, Franklin Lakes, NJ, USA), 0.1%$_{w/v}$ MgSO$_4$·7H$_2$O and 1.5%$_{w/v}$ agar (Fujifilm Wako Pure Chemical Corporation)] and incubated at 37 °C for 12 h. All the compounds were prepared in DMSO solution at a concentration of 10 mM. The samples were diluted to sixteen sample concentrations (0.078125, 0.15625, 0.3125, 0.625, 1.25, 1.5625 2.5, 3.125, 5, 6.25, 10, 12.5, 25, 50, 100, and 200 μM) in 96-well plates which contained the microbial strains incubated in YP medium. DMSO was also included as a control. The plates were then incubated further at 37 °C for 12 h. Ampicillin (Nacalai Tesque, Kyoto, Japan) and kanamycin (Nacalai) were used as reference reagents. Lastly, 10 μL of MTT solution (3-(4,5-dimethylthiazol-2-yl)-2,5-diphenyl-2H-tetrazolium bromide (0.5 mg/mL in iPrOH-HCl) was added into each well and incubated at 37 °C for another 1 h. All the antibacterial assays were performed in triplicate. The MIC values were defined as the lowest concentration at which no bacteria growth was observed.

References

1. Russo E and Guy GW (2006) A tale of two cannabinoids: the therapeutic rationale for combining tetrahydrocannabinol and cannabidiol. Medical Hypotheses, 66(2):234–46.

2. Howlett AC, Evans DM, and Houston DB (2009) The cannabinoid receptor. Marijuana/cannabinoids, 4:35–72.

3. Turner SE, Williams CM, Iversen L, and Whalley BJ (2017) Molecular pharmacology of phytocannabinoids. Phytocannabinoids, 61−101.

4. Hill KP, Palastro MD, Johnson B and Ditre JW (2017) Cannabis and pain: a clinical review. Cannabis and cannabinoid research, 2(1), 96–104.

5. Lakhan SE, and Rowland M (2009) Whole plant cannabis extracts in the treatment of spasticity in multiple sclerosis: a systematic review. BMC neurology, 9(1), 1–6.

6. Machado Rocha FC, Stefano SC, De Cassia Haiek R, Rosa Oliveira LMQ and Da Silveira DX (2008) Therapeutic use of *Cannabis sativa* on chemotherapy-induced nausea and vomiting among cancer patients: systematic review and meta-analysis. European journal of cancer care, 17(5), 431–443.

7. Stockings E, Zagic D, Campbell G, Weier M, Hall WD, Nielsen S, Herkes GK, Farrell M, and Degenhardt L (2018) Evidence for cannabis and cannabinoids for epilepsy: a systematic review of controlled and observational evidence. Journal of Neurology, Neurosurgery & Psychiatry, 89(7):741–53.

8. MacMillan K, Keddy A, and Furlong J (2019) Cannabis and glaucoma: A literature review. Dalhousie Medical Journal.

9. Citti C, Linciano P, Russo F, Luongo L, Iannotta M, Maione S, Lagana A, Capriotti AL, Forni F, Vandelli MA, and Cannazza G (2019) A novel phytocannabinoid isolated from *Cannabis sativa* L. with an in vivo cannabimimetic activity higher than Δ^9-tetrahydrocannabinol: Δ^9-Tetrahydrocannabiphorol. Scientific reports, *9*(1): 1−13.

10. Chicca A, Schafroth MA, Reynoso-Moreno I, Erni R, Petrucci V, Carreira EM, and Gertsch J (2018) Uncovering the psychoactivity of a cannabinoid from liverworts associated with a legal high. Science advances, 4(10).

11. Schafroth MA, Mazzoccanti G, Reynoso-Moreno I, Erni R, Pollastro F, Caprioglio D, Botta B, Allegrone G, Grassi G, Chicca A, and Gasparrini F (2021) Δ^9-*cis*-Tetrahydrocannabinol: natural occurrence, chirality, and pharmacology. Journal of natural products, 84(9):2502−10.

12. Luo XZ, Reiter MA, and Keasling JD (2019) Complete biosynthesis of cannabinoids and their unnatural analogues in yeast. Nature, 567: 123–126.

13. Taura F, Tanaka S, Taguchi C, Fukamizu T, Tanaka H, Shoyama Y, and Morimoto S (2009) Characterization of olivetol synthase, a polyketide synthase putatively involved in cannabinoid biosynthetic pathway. FEBS Letters, 583 (12): 2061–2066.

14. Gagne SJ, Stout JM, Liu E, Boubakir Z, Clark SM, and Page JE (2012) Identification of olivetolic acid cyclase from *Cannabis sativa* reveals a unique catalytic route to plant polyketides. Proceedings of the National Academy of Sciences, 109: 12811–12816.

15. Anderson LL, Udoh M, Everett-Morgan D, Heblinski M, McGregor IS, Banister SD, and Arnold JC (2022) Olivetolic acid, a cannabinoid precursor in *Cannabis sativa*, but not CBGA methyl ester exhibits a modest anticonvulsant effect in a mouse model of Dravet syndrome. Journal of Cannabis Research, 4:1−9.

16. Pollastro F, Taglialatela-Scafati O, Allara M, Munoz E, Di Marzo V, De Petrocellis L, and Appendino G (2011) Bioactive prenylogous cannabinoid from fiber hemp (*Cannabis sativa*). Journal of Natural Product, 74:2019−2022.

17. Izzo AA, Borrelli F, Capasso R, Di Marzo V, and Mechoulam R (2009) Non-psychotropic plant cannabinoids: new therapeutic opportunities from an ancient herb. Trends in pharmacological sciences, 30:515−527.

18. van Breemen RB, Muchiri RN, Bates TA, Weinstein JB, Leier HC, Farley S, and Tafesse FG (2022) Cannabinoids block cellular entry of SARS-CoV-2 and the emerging variants. Journal of Natural Products, 85:176−184.

19. Karas JA, Wong LJ, Paulin OK, Mazeh AC, Hussein MH, Li J, and Velkov T (2020) The antimicrobial activity of cannabinoids. Antibiotics, 9(7):406.

20. Kamanna K, Kamath A (2022) Prenylation of natural products: an overview. In: Zhan X, Jabbari A (eds) Modifications of biomolecules. IntechOpen,

London.

21. Lee YE, Nakashima Y, Kodama T, Chen X, and Morita H (2021) Dual engineering of olivetolic acid cyclase and tetraketide synthase to generate longer alkyl-chain olivetolic acid analogs. Organic Letters, 24: 410−414.

22. Lee YE, Kodama T, and Morita H (2022) Novel insights into the antibacterial activities of cannabinoid biosynthetic intermediate, olivetolic acid, and its alkyl-chain derivatives. Journal of Natural Medicines, 26:1−8.

23. Austin MB and Noel JP (2003) The Chalcone Synthase Superfamily of Type III Polyketide Synthases. Natural Product Reports, 20 (1), 79-110.

24. Abe I and Morita H (2010) Structure and function of the chalcone synthase superfamily of plant type III polyketide synthases. Natural Product Reports, 27 (6), 809−38.

25. Morita H, Abe I, and Noguchi H (2010) Plant type III polyketide synthases. In comprehensive natural products II: Chemistry and Biology. Liu, H.-W.; Mander, L., Eds; Elsevier, Oxford, UK, 171–225.

26. Morita H, Wong CP, and Abe I (2019) How structural subtleties lead to molecular diversity for the type III polyketide synthases. Journal of Biological Chemistry, 294 (41), 15121–15136.

27. Abe I (2020) Biosynthesis of medicinally important plant metabolites by unusual type III polyketide synthases. Journal of Natural Medicine, 74 (4), 639−646.

28. Yang X, Matsui T, Kodama T, Mori T, Zhou X, Taura F, Noguchi H, Abe I, and Morita H (2016) Structural basis for olivetolic acid formation by a polyketide cyclase from *Cannabis sativa*. The FEBS Journal, 283 (6), 1088−1106.

29. Mizuuchi Y, Shimokawa Y, Wanibuchi K, Noguchi H, and Abe, I. Structure function analysis of novel type III polyketide synthases from *Arabidopsis thaliana*. Biological and Pharmaceutical Bulletin, 2008, 31 (12), 2205−2210.

30. Abe I, Oguro S, Utsumi Y, Sano Y, and Noguchi H (2005) Engineered biosynthesis of plant polyketides: chain length control in an octaketide-producing plant type III polyketide synthase. Journal of the American Chemical Society, 127 (36), 12709−12716.

31. Kearsey LJ, Prandi N, Karuppiah V, Yan C, Leys D, Toogood H, Takano E, and Scrutton NS (2020) Structure of the *Cannabis sativa* olivetol-producing enzyme reveals cyclization plasticity in type III polyketide synthases. The FEBS Journal, 287 (8), 1511−1524.

32. Ju Y (2017) Combinatorial biosynthesis of aloesone analog by exploiting a type III polyketide synthase and olivetolic acid cyclase. Master text. Graduate School of Medicine and Pharmaceutical Sciences for Education University of Toyama.

33. Appendino G, Gibbons S, Giana A, Pagani A, Grassi G, Stavri M, Smith E, and Rahman MM (2008) Antibacterial cannabinoids from *Cannabis sativa*: a structure-activity study. Journal of Natural Products, 71:1427−1430.

34. Cochrane RV, Sanichar R, Lambkin GR, Reiz B, Xu W, Tang Y, and Vederas JC (2016) Production of new cladosporin analogues by reconstitution of the polyketide synthases responsible for the biosynthesis of this antimalarial agent. Angewandte Chemie, 128 (2), 674−678.

35. Zhu Y, Soroka DN, and Sang S (2012) Synthesis and inhibitory activities against colon cancer cell growth and proteasome of alkylresorcinols. Journal of Agricultural and Food Chemistry, 60 (35), 8624−8631.

36. Martin BR, Jefferson R, Winckler R, Wiley JL, Huffman JW, Crocker PJ, Saha B, and Razdan RK (1999) Manipulation of the tetrahydrocannabinol side chain delineates agonists, partial agonists, and antagonists. Journal of Pharmacology and Experimental Therapeutics, 290:1065−1079.

37. Farha MA, El-Halfawy OM, Gale RT, MacNair CR, Carfrae LA, Zhang X, Jantsch NG, Mogolan J, and Brown ED (2020) Uncovering the hidden antibiotic potential of cannabis. ACS Infectious Diseases, 6:338−346.

38. Ji XY, Chen JH, Zheng GH, Huang MH, Zhang L, Yi H, Jin J, Jiang JD, Peng ZG, Li ZR (2016) Design and synthesis of Cajanine analogues against hepatitis C virus through down-regulating host chondroitin sulfate N-acetylgalactosaminyltransferase 1. Journal of Medicinal Chemistry. 59:10268−84.

39. Valliere MA, Korman TP, Woodall NB, Khitrov GA, Taylor RE, Baker D, and Bowie JU (2019) A cell-free platform for the prenylation of natural products

and application to cannabinoid production. Nature Communication, 10:1−9.

40. Nevarez DM, Mengistu YA, Nawarathne IN, and Walker KD (2009) An *N*-aroyltransferase of the BAHD superfamily has broad aroyl CoA specificity *in vitro* with analogues of *N*-dearoylpaclitaxel. Journal of the American Chemical Society, 131 (16), 5994−6002.

41. Matsui T, Kodama T, Mori T, Tadakoshi T, Noguchi H, Abe I, and Morita H (2017) 2-Alkylquinolone alkaloid biosynthesis in the medicinal plant *Evodia rutaecarpa* involves collaboration of two novel type III polyketide synthases. Journal of Biological Chemistry, 292 (22), 9117−9135.

42. Kabsch W (2002) XDS. Acta Crystallographica Section D Biological Crystallography, 66 (2), 125−132.

43. Evans, P (2006) Scaling and assessment of data quality. Acta Crystallographica, 62 (1), 72−82.

44. Collaborative Computational Project, Number 4 (1994) The CCP4 suite: programs for protein crystallography. Acta Crystallographica Section D Biological Crystallography, 50 (Pt 5), 760−763.

45. McCoy AJ, Grosse-Kunstleve RW, Adams PD, Winn MD, Storoni LC, and Read RJ (2007) Phaser crystallographic software. Journal of Applied Crystallography, 40 (4), 658−674.

46. Adams PD, Afonine PV, Bunkoczi G, Chen VB, Davis IW, Echols N, Jeffry J, and Zwart PH (2010) PHENIX: a comprehensive python-based system for macromolecular structure solution. Acta Crystallographica Section D Biological Crystallography, 66 (2), 213−221.

47. Emsley P, Lohkamp B, Scott WG, Cowtan K (2010) Features and development of Coot. Acta Crystallographica Section D Biological Crystallography, 66 (4), 486−501.

48. Afonine PV, Grosse-Kunstleve RW, Echols N, Headd JJ, Moriarty NW, Mustyakimov M, Terwilliger TC, Urzhumtsev A, Zwart PH, and Adams PD (2012) Towards automated crystallographic structure refinement with phenix. refine. Acta Crystallographica Section D Biological Crystallography, 68 (4), 352−367.

49. DeLano WL (2002) The PyMOL user's manual. DeLano Scientific, San Carlos, CA, 452.

50. Liebschner D, Afonine PV, Moriarty NW, Poon BK, Sobolev OV, Terwilliger TC, and Adams PD (2017) Polder maps: improving OMIT maps by excluding bulk solvent. Acta Crystallographica Section D Biological Crystallography, 73 (2), 148−157.

51. Jentsch NG, Zhang X, and ,Magolan J (2020) Efficient synthesis of cannabigerol, grifolin, and piperogalin via alumina-promoted allylation. Journal of Natural Products, 83(9):2587−91.

52. Eloff JN (1998) A sensitive and quick microplate method to determine the minimal inhibitory concentration of plant extracts for bacteria. Planta Medica, 64:711−713.

List of publications

1. Lee YE, Nakashima Y, Kodama T, Chen X, Morita H (2021) Dual engineering of olivetolic acid cyclase and tetraketide synthase to generate longer alkyl-chain olivetolic acid analogs. Organic Letters, 24: 410−4.

2. Lee YE, Kodama T, Morita H (2022) Novel insights into the antibacterial activities of cannabinoid biosynthetic intermediate, olivetolic acid and its alkyl-chain derivatives. Journal of Natural Medicine, 77:298−305.

Acknowledgement

Appendices

Fig. S1 ^{1}H NMR (400 MHz) spectrum of cannabigerovarin (**1a**) in CDCl$_3$.
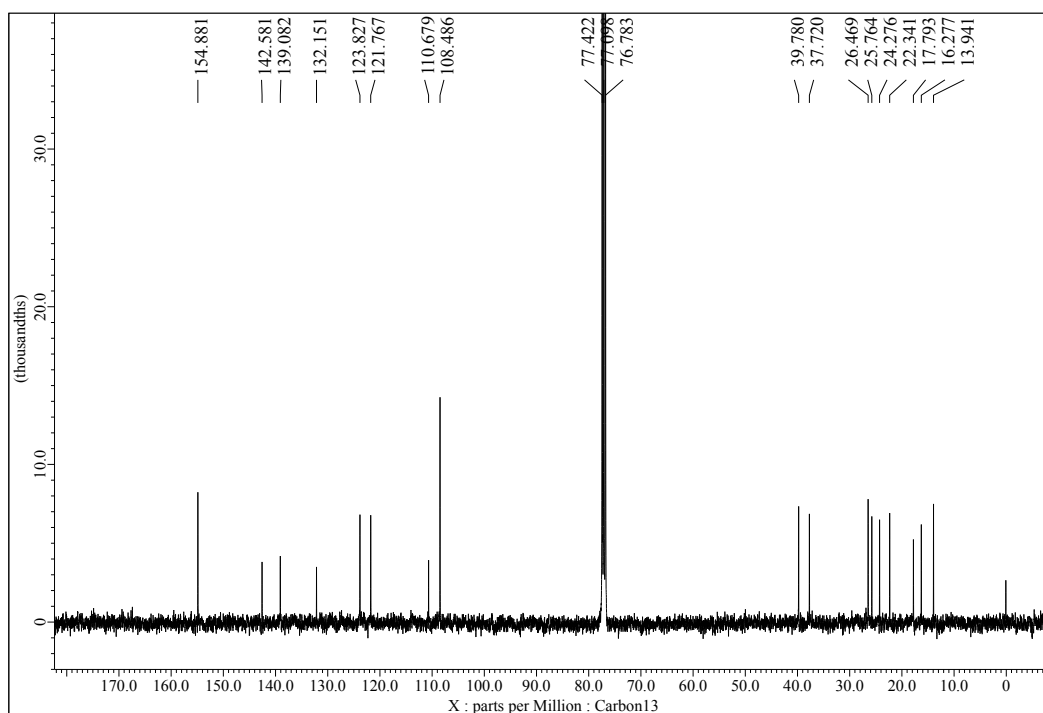
Fig. S2 ^{13}C NMR (125 MHz) spectrum of cannabigerovarin (**1a**) in CDCl$_3$.
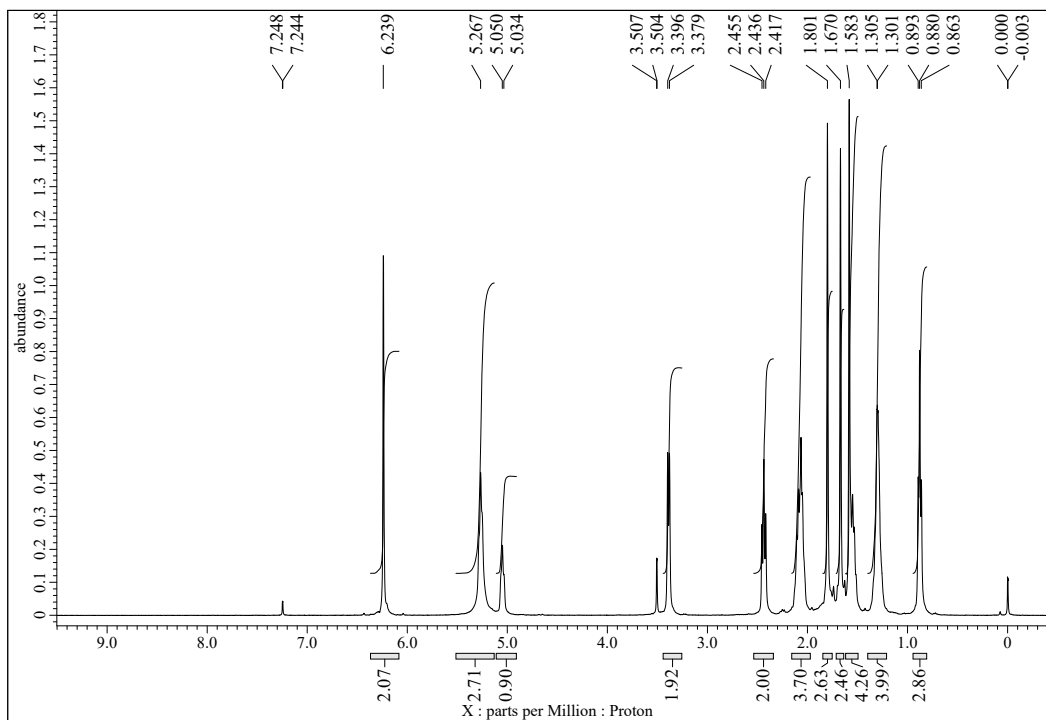
Fig. S3 ^{1}H NMR (400 MHz) spectrum of cannabigerol (CBG) (**1b**) in CDCl$_3$.
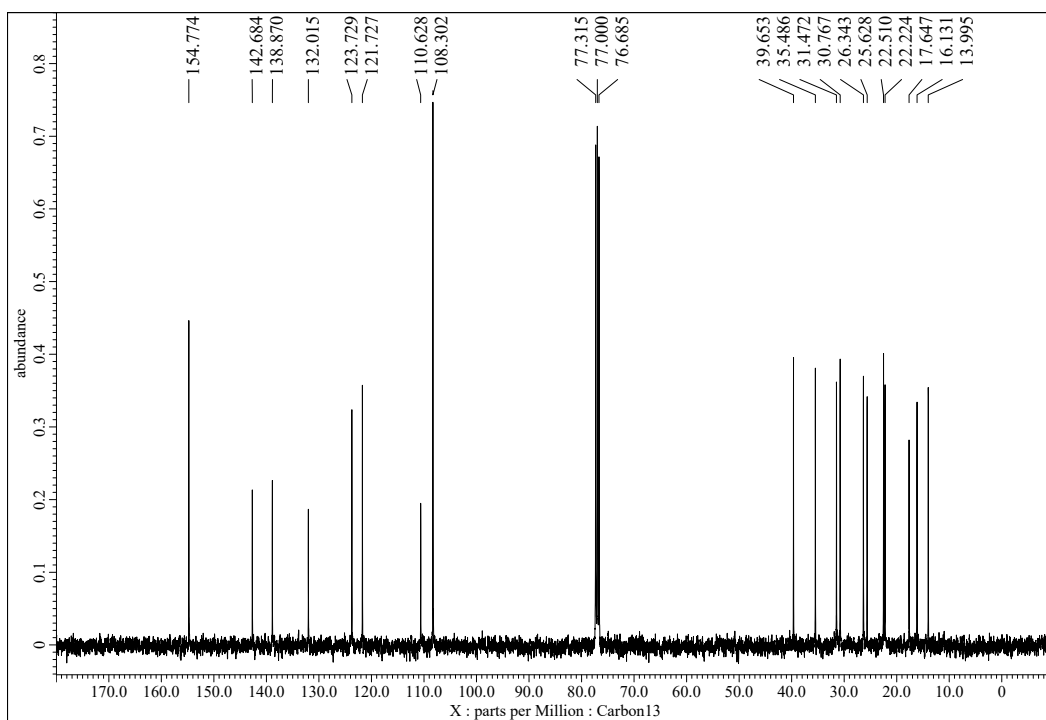
Fig. S4 ^{13}C NMR (125 MHz) spectrum of cannabigerol (CBG) (**1b**) in CDCl$_3$.
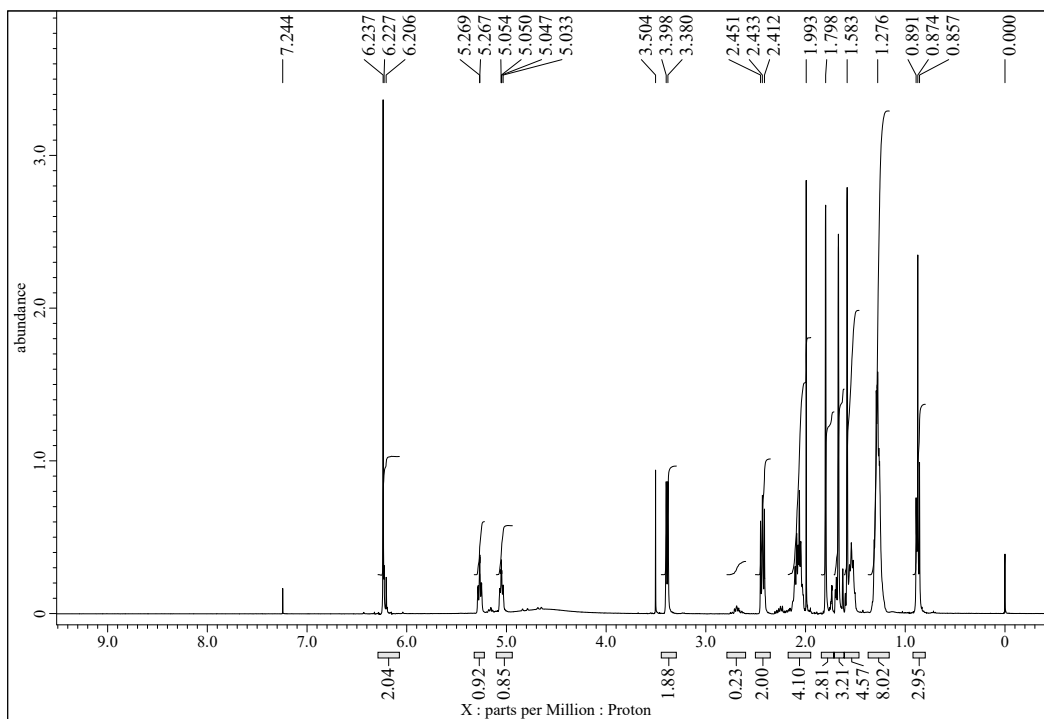
Fig. S5 ^{1}H NMR (400 MHz) spectrum of Cannabigerophorol (CBGP) (**1c**) in CDCl$_3$.
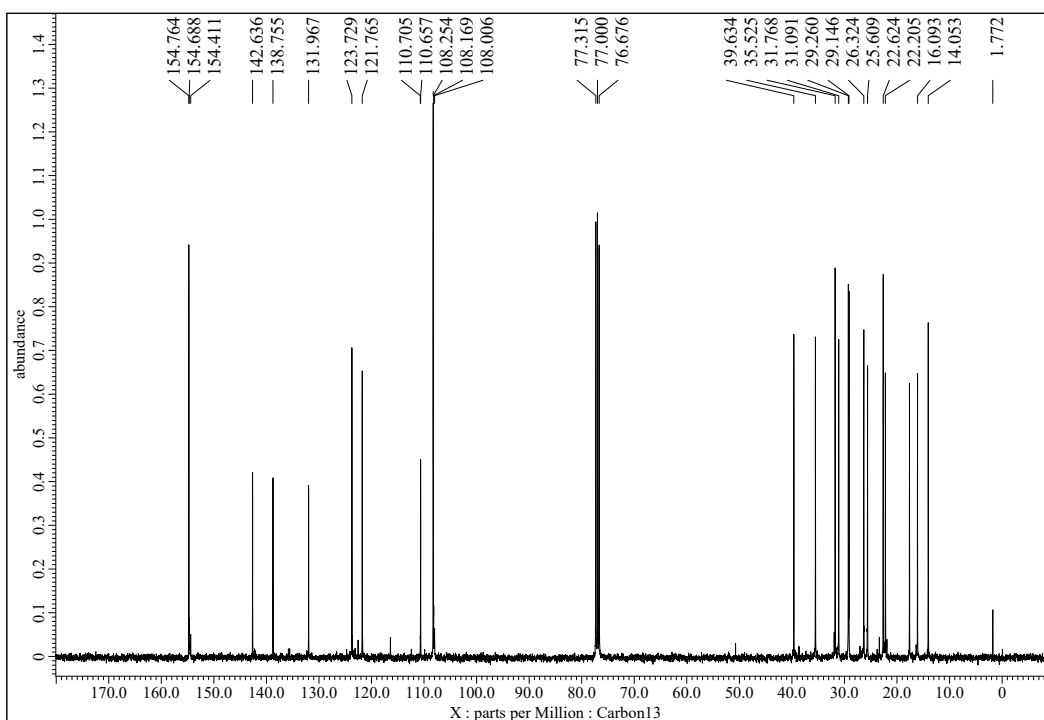
Fig. S6 ^{13}C NMR (125 MHz) spectrum of Cannabigerophorol (CBGP) (**1c**) in CDCl$_3$.
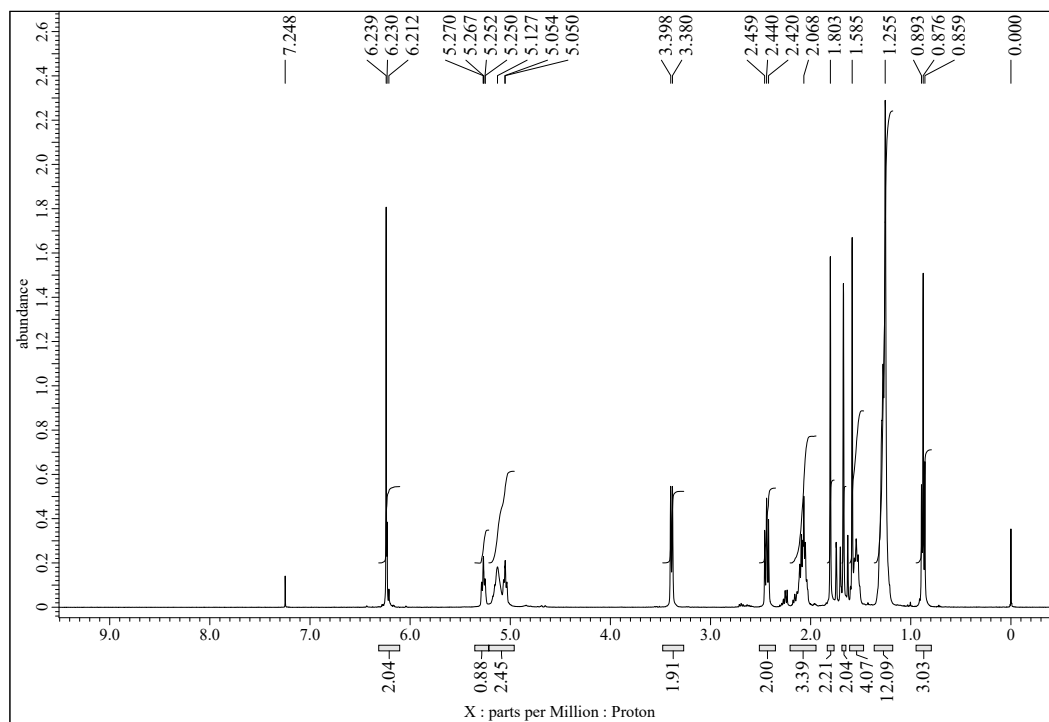
Fig. S7 ^{1}H NMR (400 MHz) spectrum of (*E*)-2-(3,7-dimethylocta-2,6-dien-1-yl)-5-nonylbenzene-1,3-diol (**1d**) in CDCl$_3$.
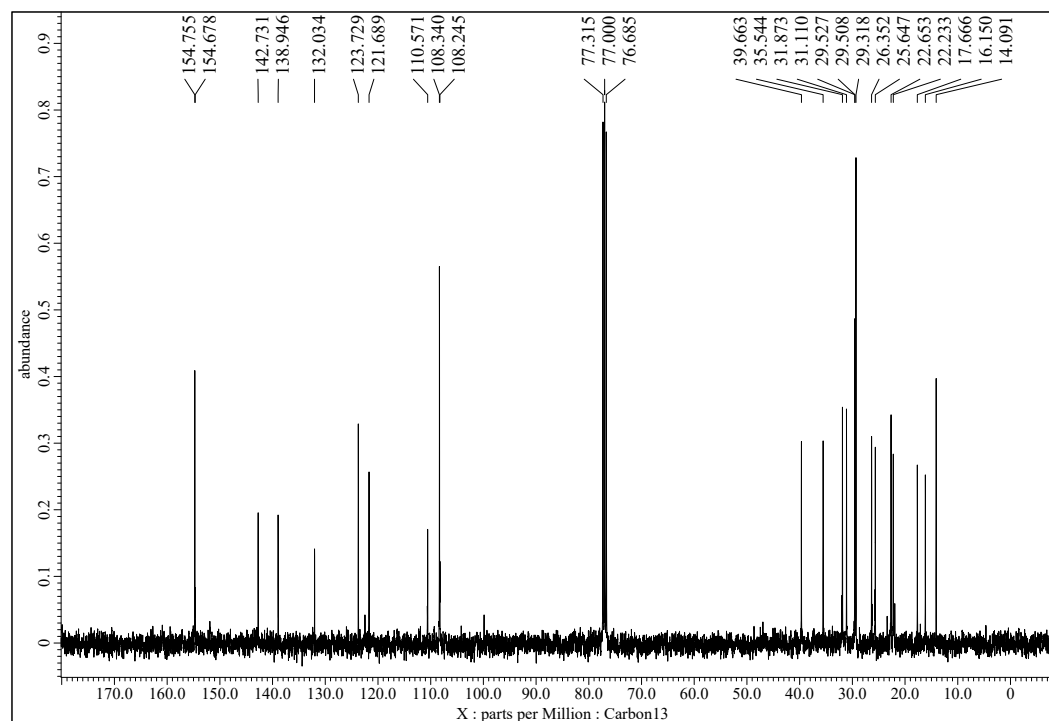
Fig. S8 ^{13}C NMR (125 MHz) spectrum of (*E*)-2-(3,7-dimethylocta-2,6-dien-1-yl)-5-nonylbenzene-1,3-diol (**1d**) in CDCl$_3$.

103
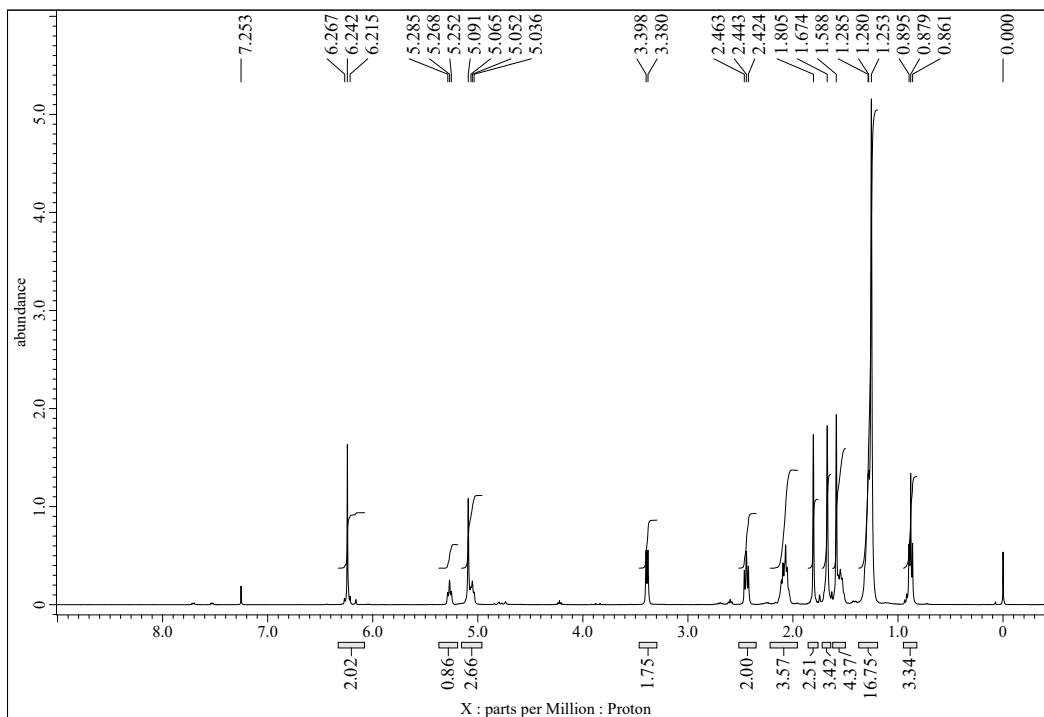
Fig. S9 ^{1}H NMR (400 MHz) spectrum of (*E*)-2-(3,7-dimethylocta-2,6-dien-1-yl)-5-undecylbenzene-1,3-diol (**1e**) in CDCl$_3$.
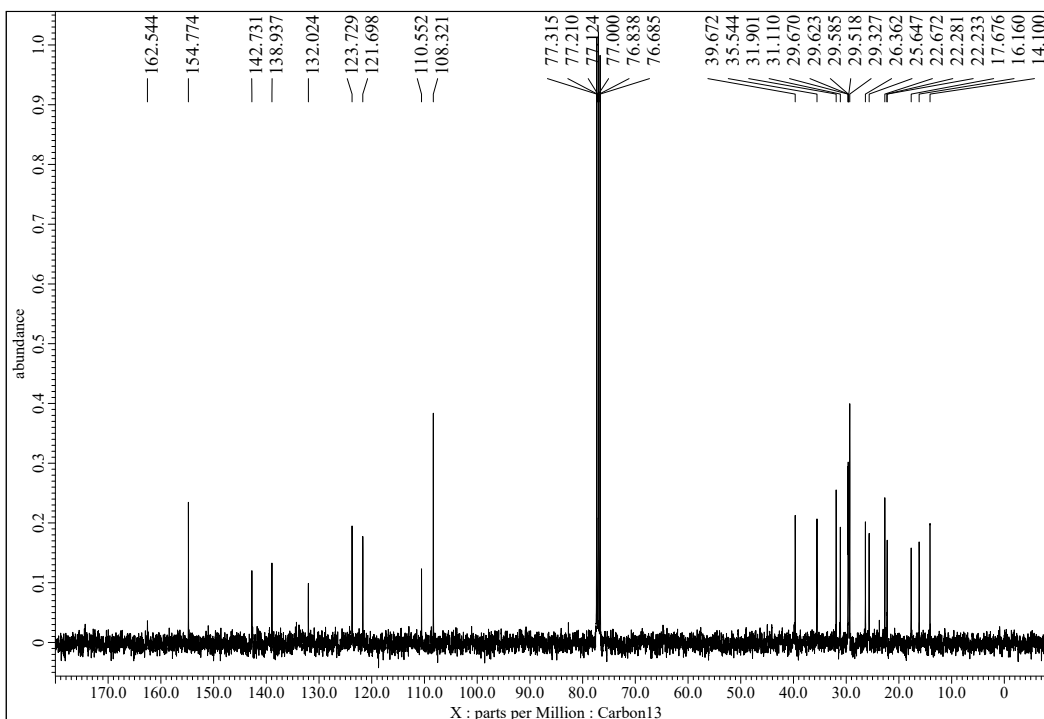
Fig. S10 ^{13}C NMR (125 MHz) spectrum of (*E*)-2-(3,7-dimethylocta-2,6-dien-1-yl)-5-undecylbenzene-1,3-diol (**1e**) in CDCl$_3$.
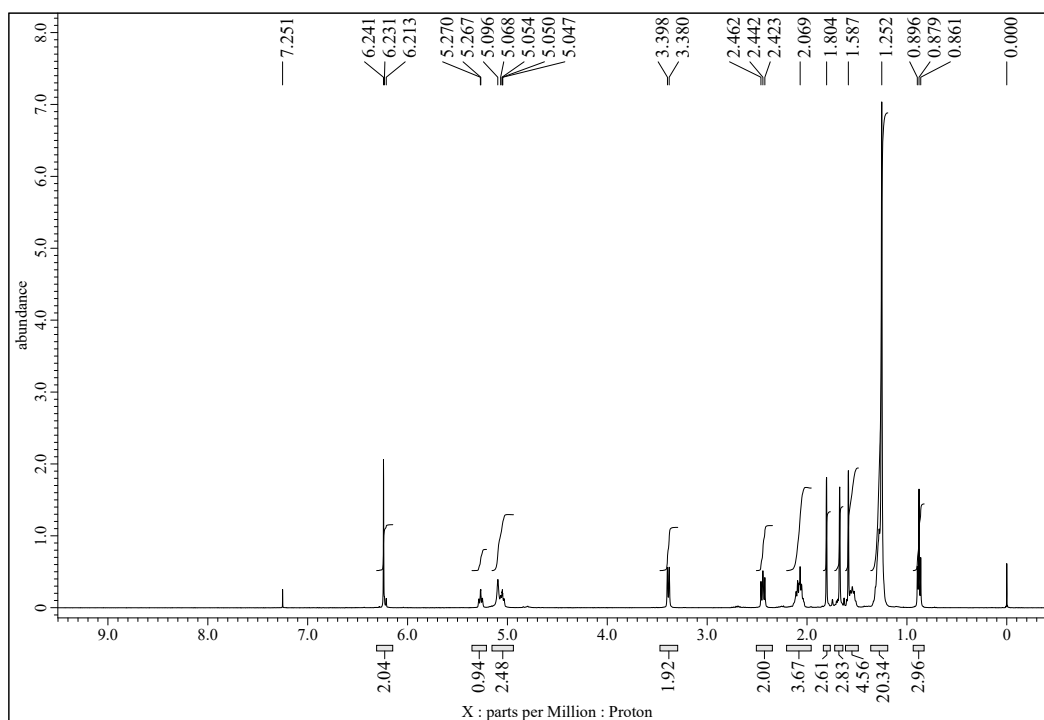
Fig. S11 ^{1}H NMR (400 MHz) spectrum of (*E*)-2-(3,7-dimethylocta-2,6-dien-1-yl)-5-tridecylbenzene-1,3-diol (**1f**) in CDCl$_3$.
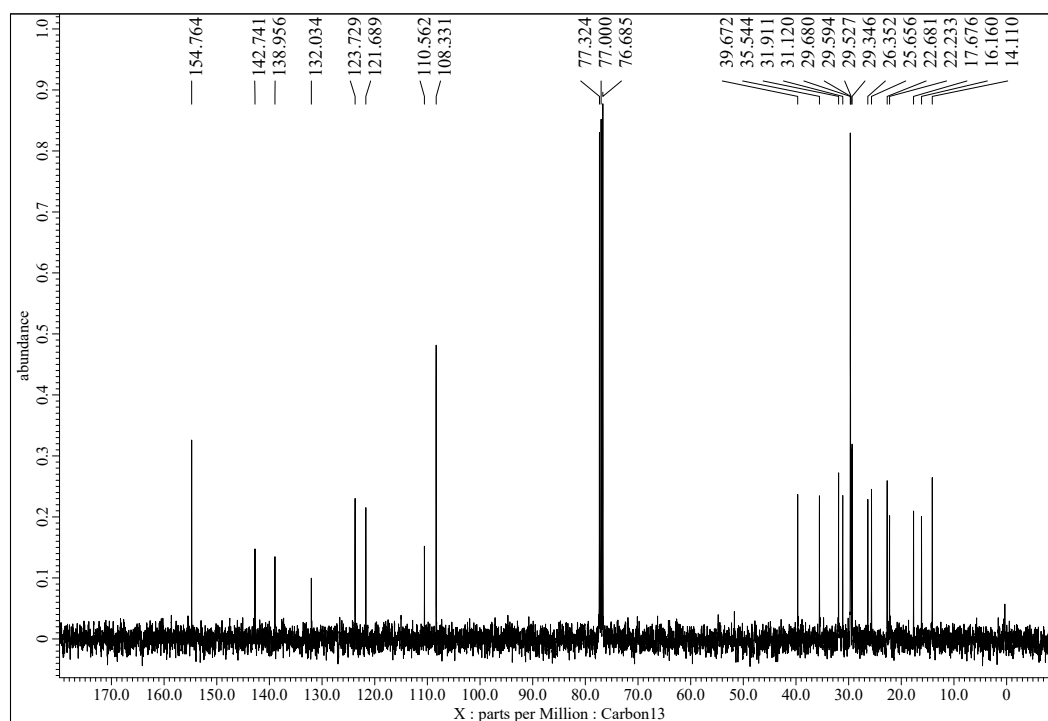
Fig. S12 ^{13}C NMR (125 MHz) spectrum of (*E*)-2-(3,7-dimethylocta-2,6-dien-1-yl)-5-tridecylbenzene-1,3-diol (**1f**) in CDCl$_3$.

105
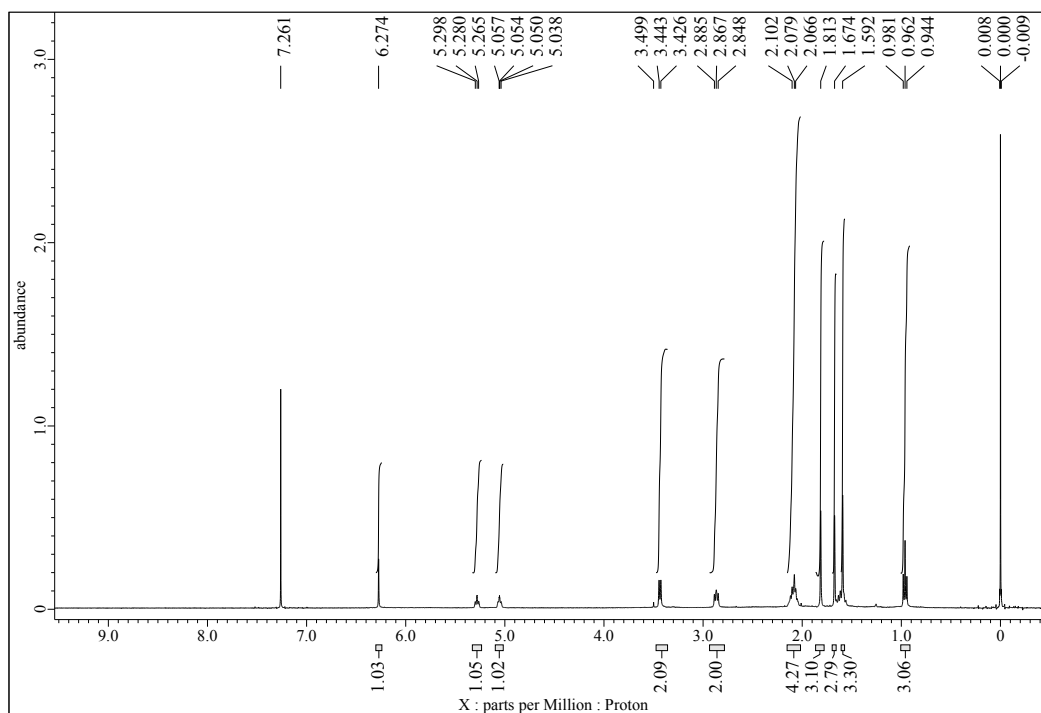
Fig. S13 ^{1}H NMR (400 MHz) spectrum of Cannabigerovarinic acid (CBGVA) (**2a**) in CDCl$_3$.
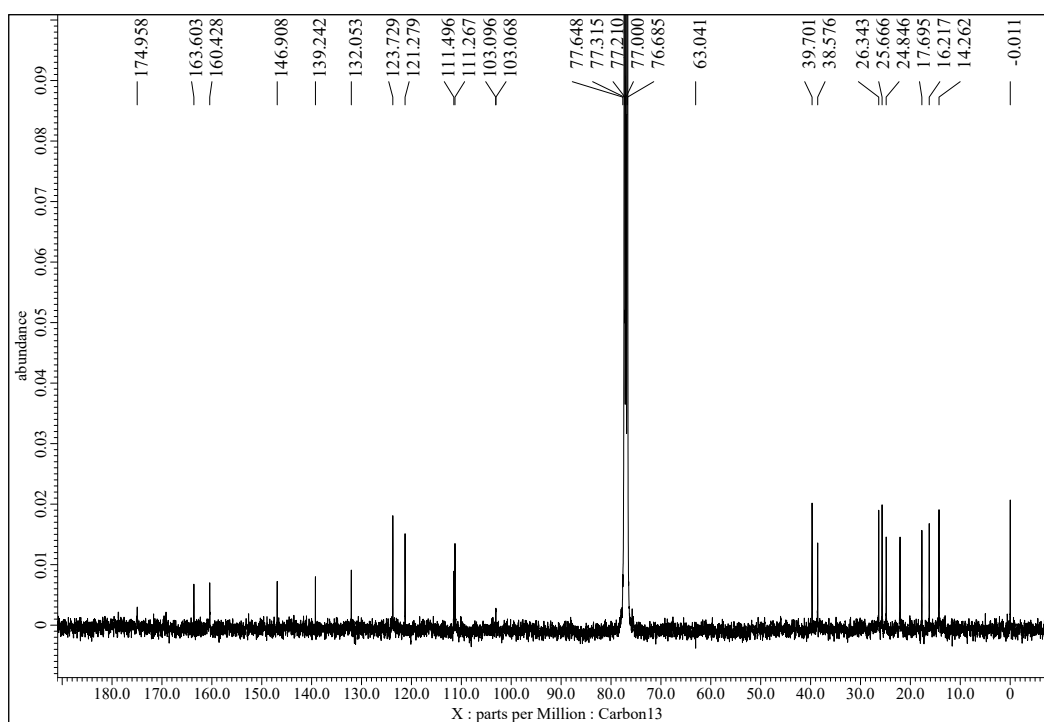
Fig. S14 ^{13}C NMR (125 MHz) spectrum of Cannabigerovarinic acid (CBGVA) (**2a**) in CDCl$_3$.
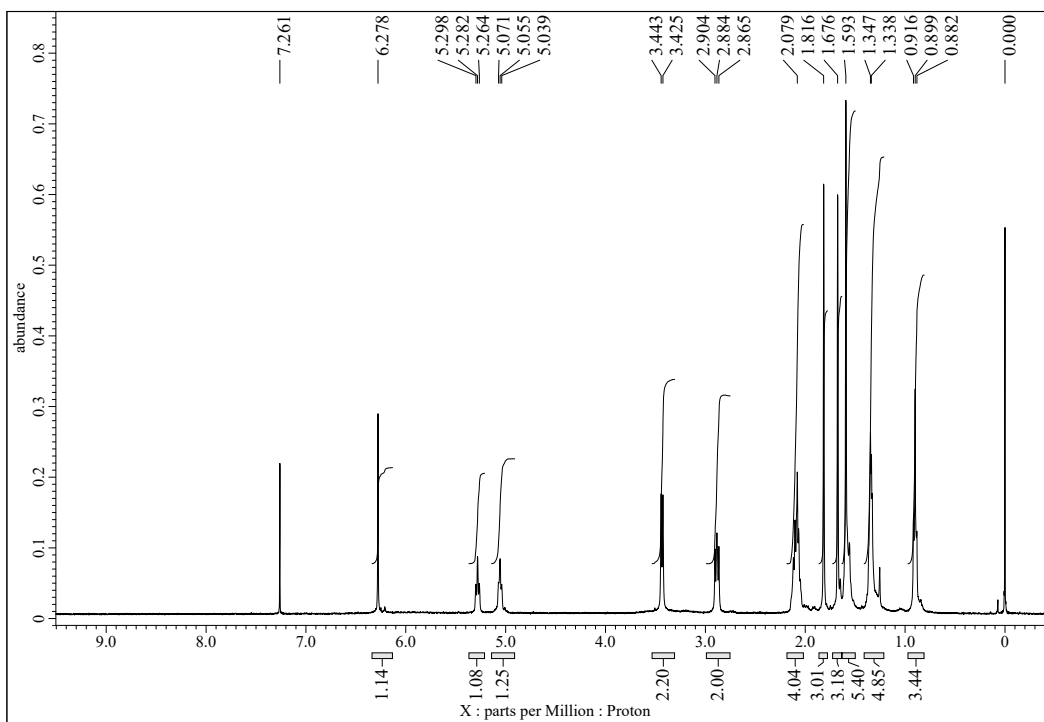
Fig. S15 ^{1}H NMR (400 MHz) spectrum of Cannabigerolic acid (CBGA) (**2b**) in CDCl$_3$.
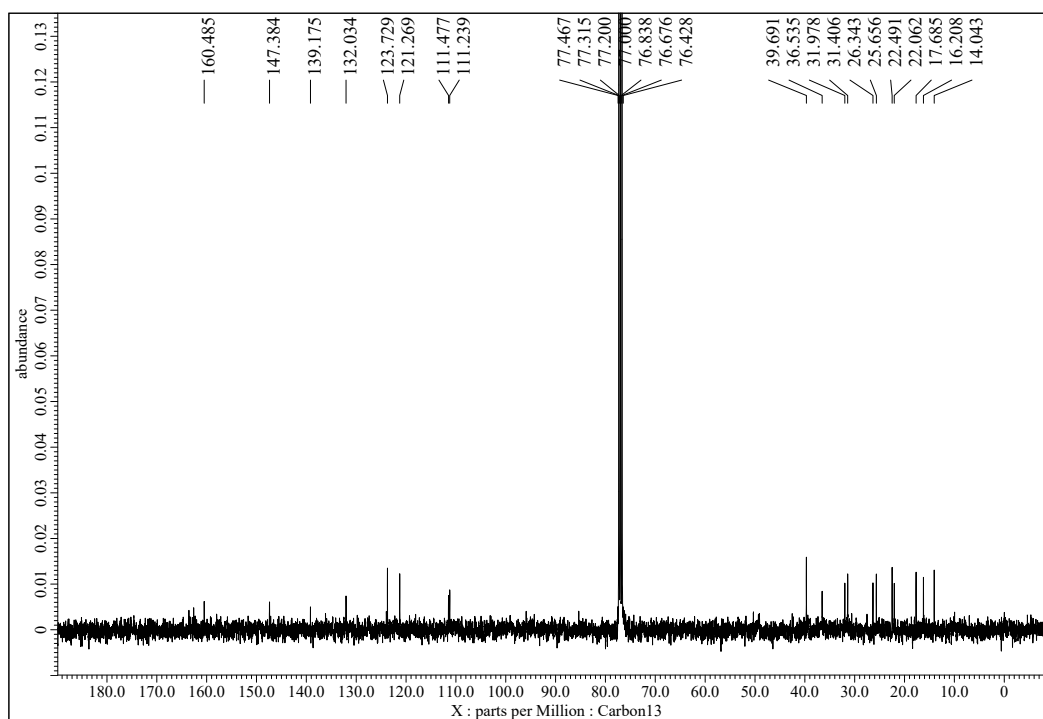
Fig. S16 ^{13}C NMR (125 MHz) spectrum of Cannabigerolic acid (CBGA) (**2b**) in CDCl$_3$.
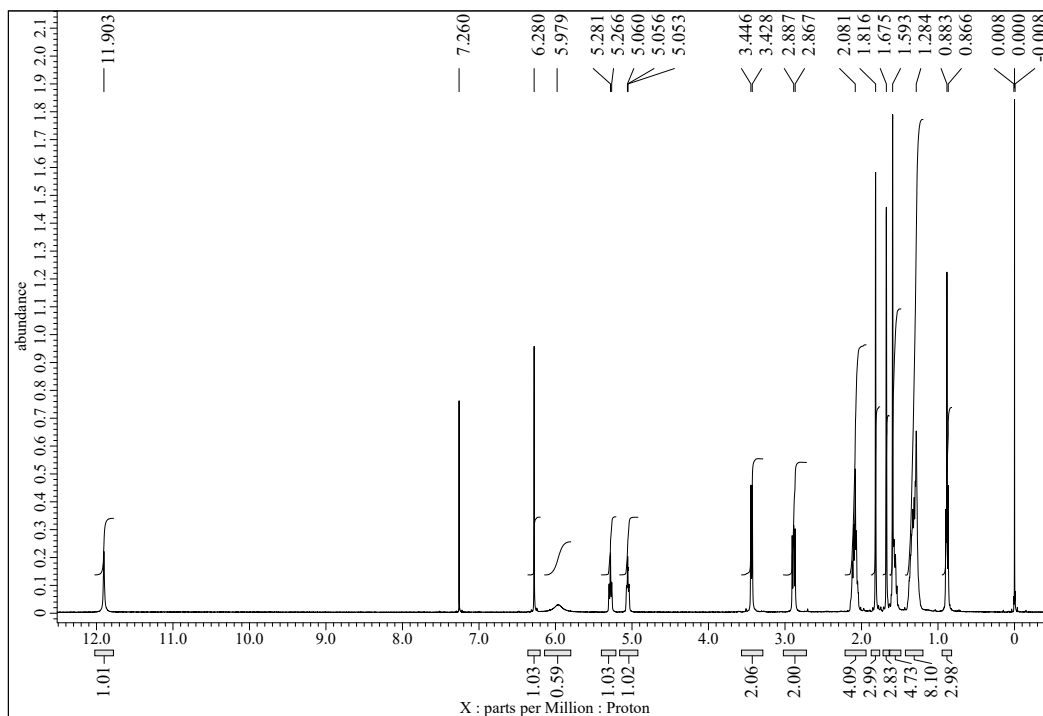
Fig. S17 ^{1}H NMR (400 MHz) spectrum of cannabigerophorolic acid (CBGPA) (**2c**) in CDCl$_3$.
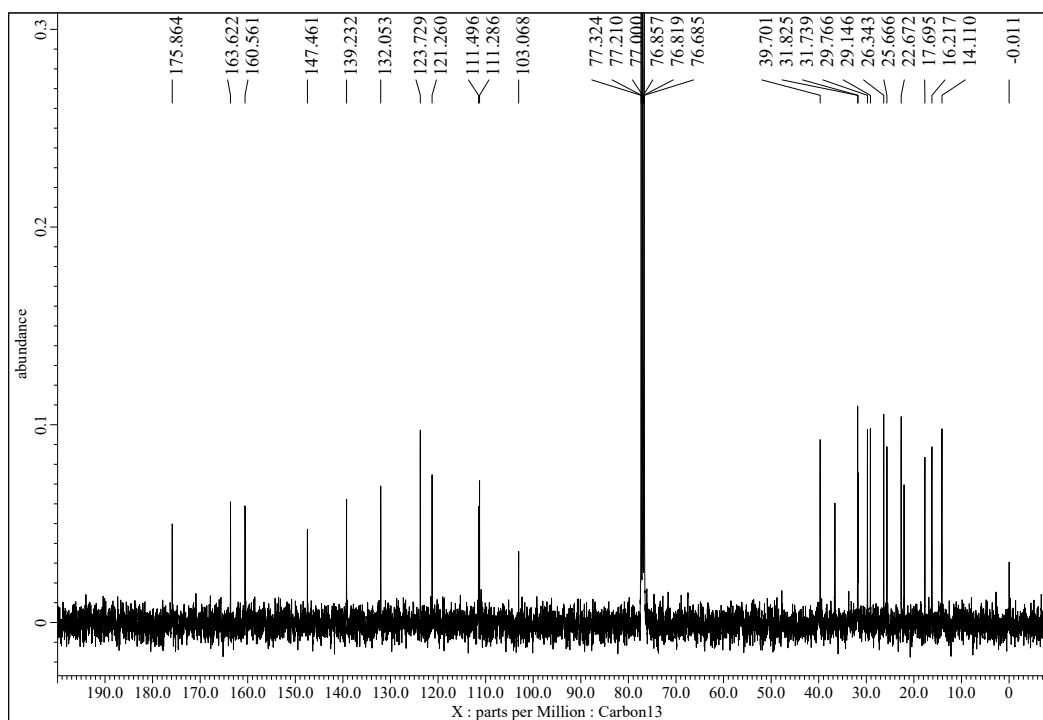
Fig. S18 ^{13}C NMR (125 MHz) spectrum of Cannabigerophorolic acid (CBGPA) (**2c**) in CDCl$_3$.
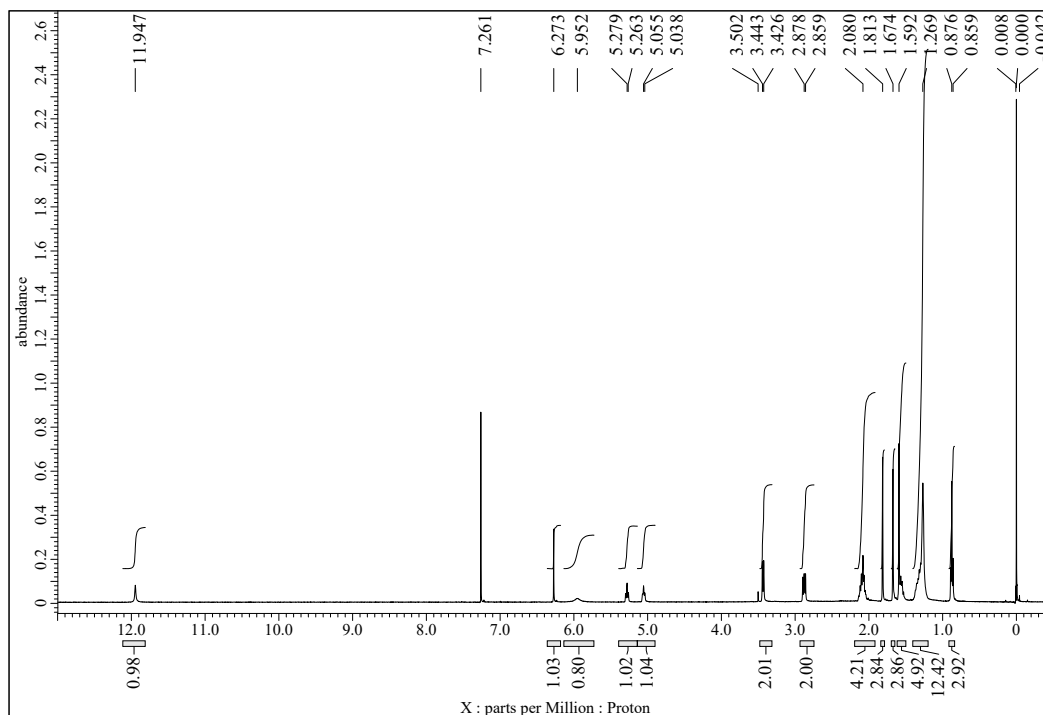
Fig. 19 ^{1}H NMR (400 MHz) spectrum of (*E*)-3-(3,7-dimethylocta-2,6-dien-1-yl)-2,4-dihydroxy-6-nonylbenzoic acid (**2d**) in CDCl₃.
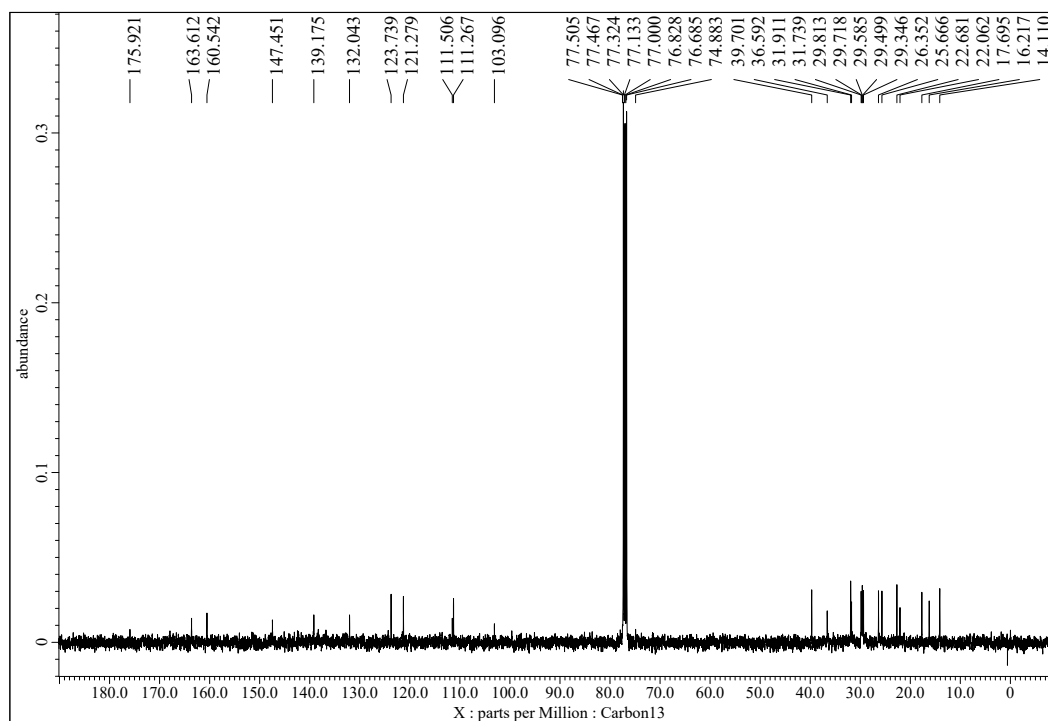
Fig. S20 ^{13}C NMR (125 MHz) spectrum of (*E*)-3-(3,7-dimethylocta-2,6-dien-1-yl)-2,4-dihydroxy-6-nonylbenzoic acid (**2d**) in CDCl₃.
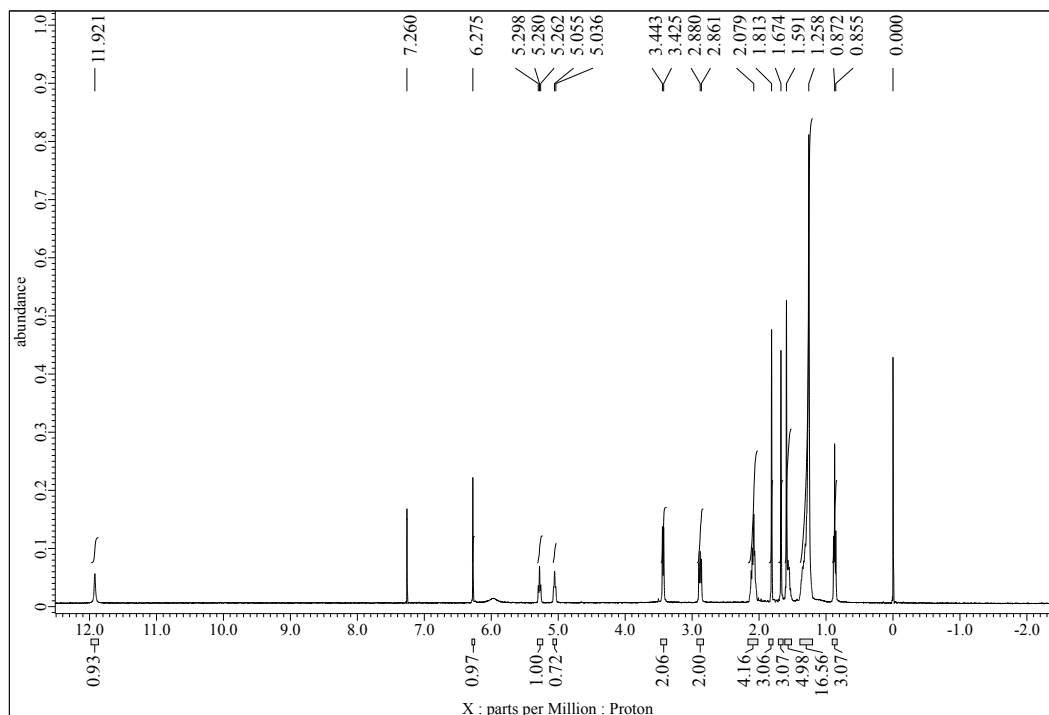
Fig. S21 ^{1}H NMR (400 MHz) spectrum of (*E*)-3-(3,7-dimethylocta-2,6-dien-1-yl)-2,4-dihydroxy-6-undecylbenzoic acid (**2e**) in CDCl$_3$.
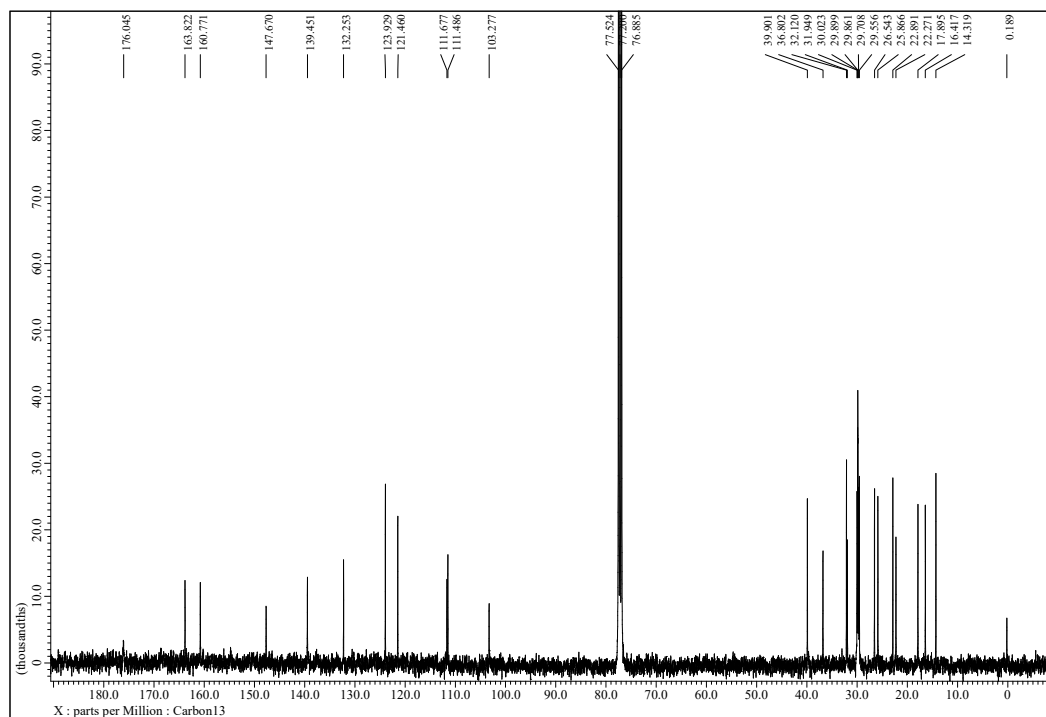
Fig. S22 ^{13}C NMR (125 MHz) spectrum of (*E*)-3-(3,7-dimethylocta-2,6-dien-1-yl)-2,4-dihydroxy-6-undecylbenzoic acid (**2e**) in CDCl$_3$.
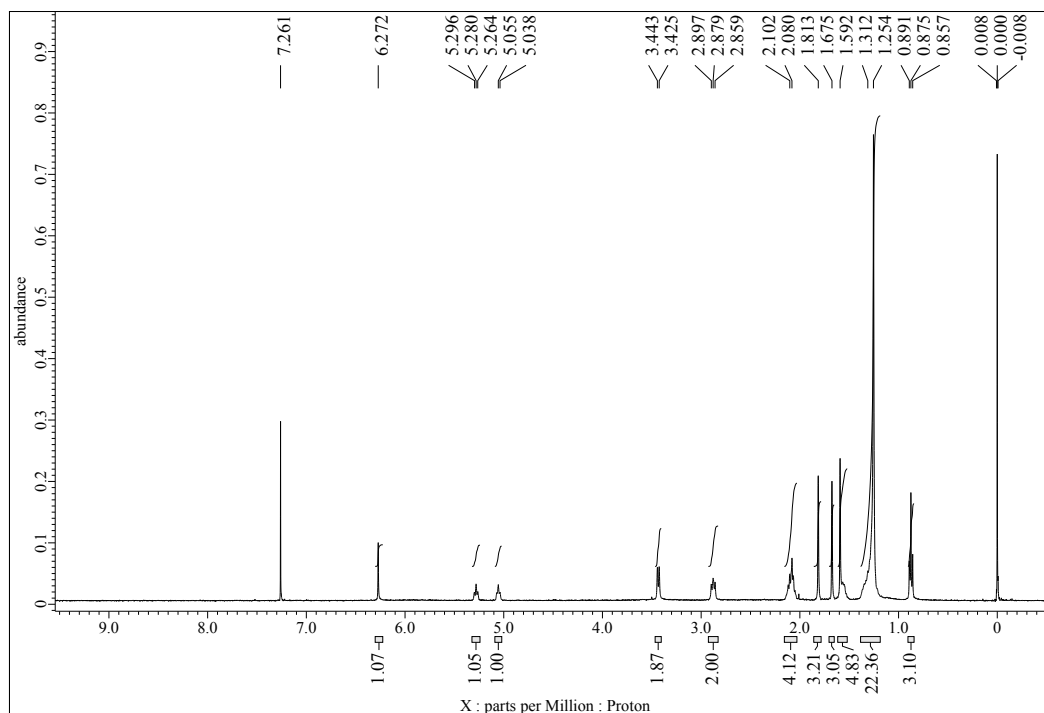
Fig. S23 ¹H NMR (400 MHz) spectrum of (*E*)-3-(3,7-dimethylocta-2,6-dien-1-yl)-2,4-dihydroxy-6-tridecylbenzoic acid (**2f**) in CDCl₃.
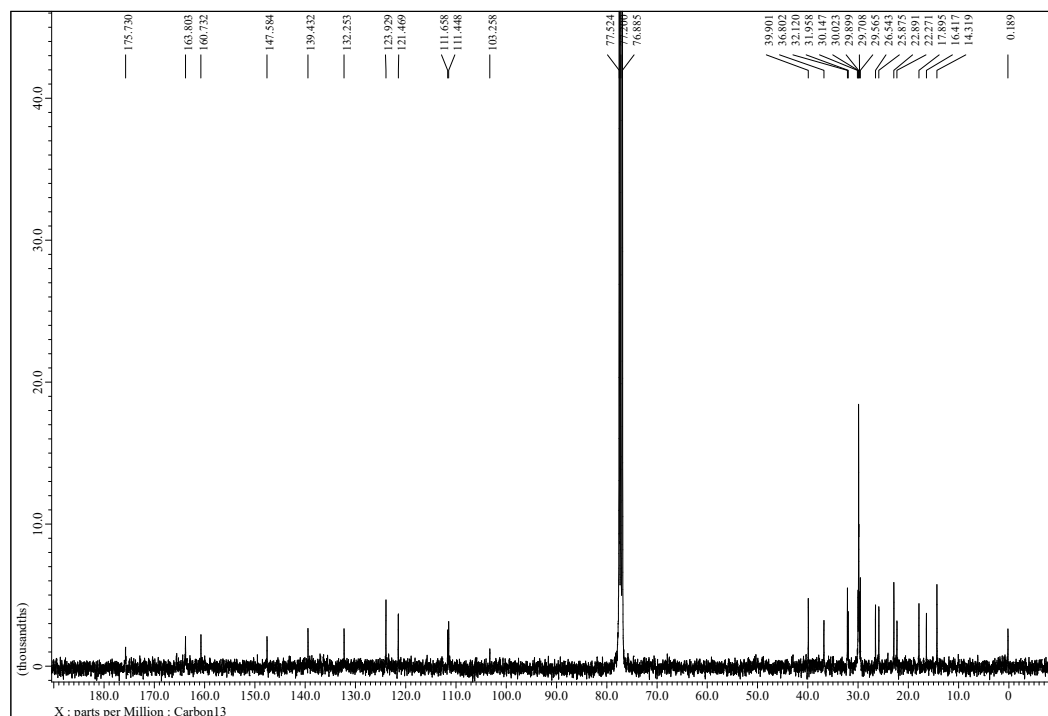
Fig. S24 ¹³C NMR (125 MHz) spectrum of (*E*)-3-(3,7-dimethylocta-2,6-dien-1-yl)-2,4-dihydroxy-6-tridecylbenzoic acid (**2f**) in CDCl₃.

111
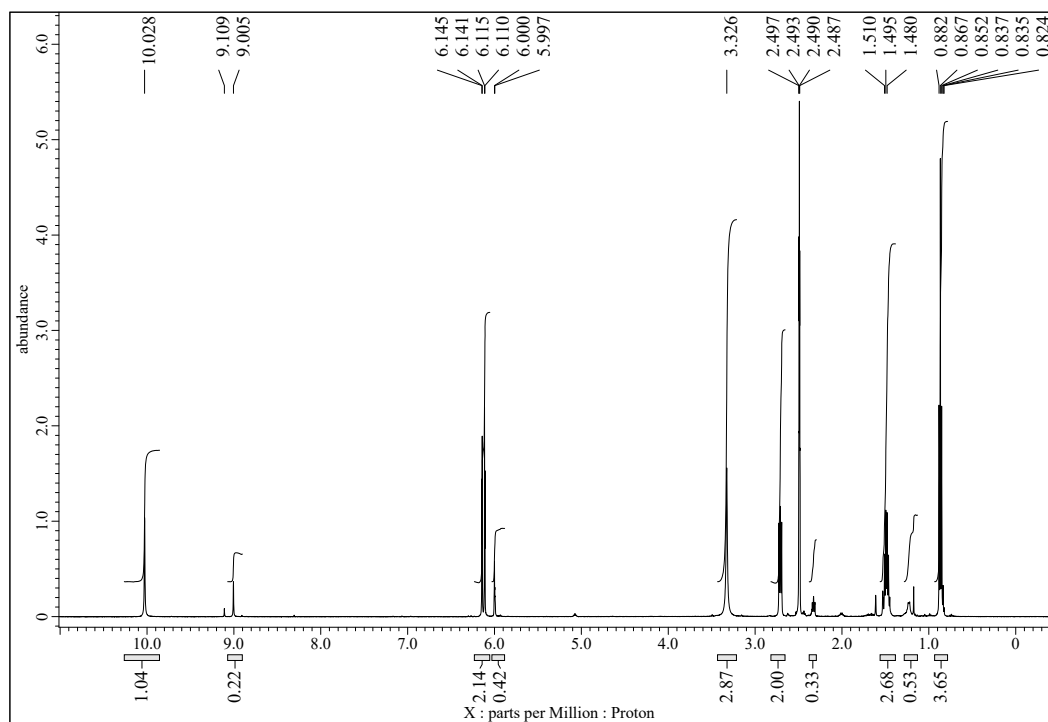
Fig. S25 ^{1}H NMR (500 MHz) spectrum of divaric acid (**3a**) in DMSO-d_6.
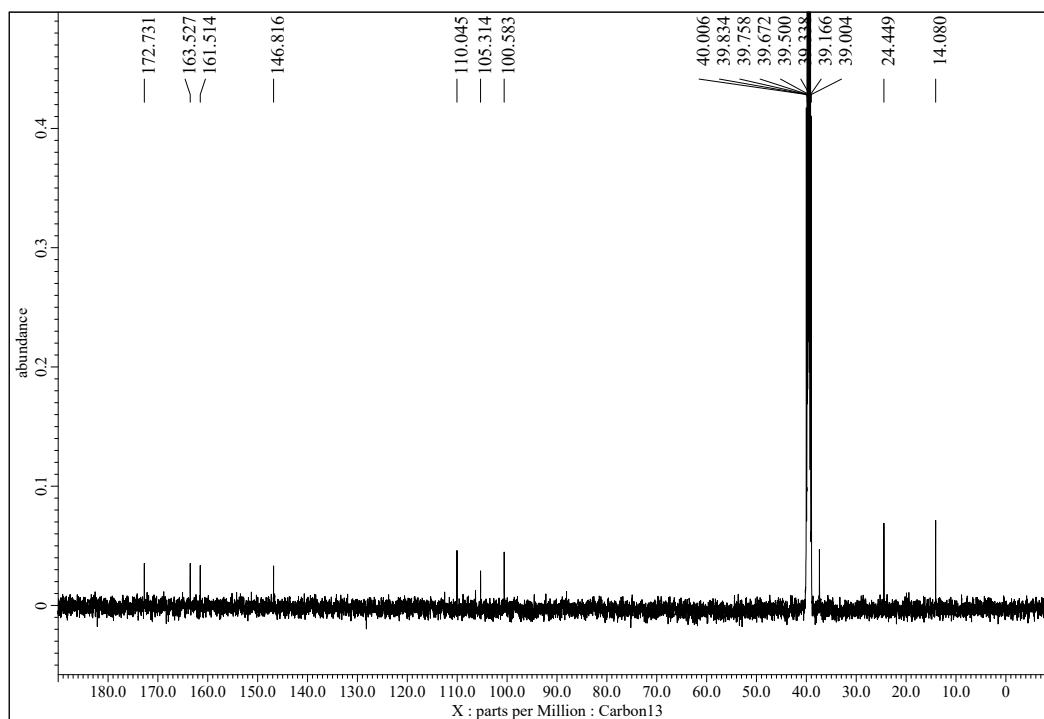
Fig. S26 ^{13}C NMR (125 MHz) spectrum of divaric acid (**3a**) in DMSO-d_6.
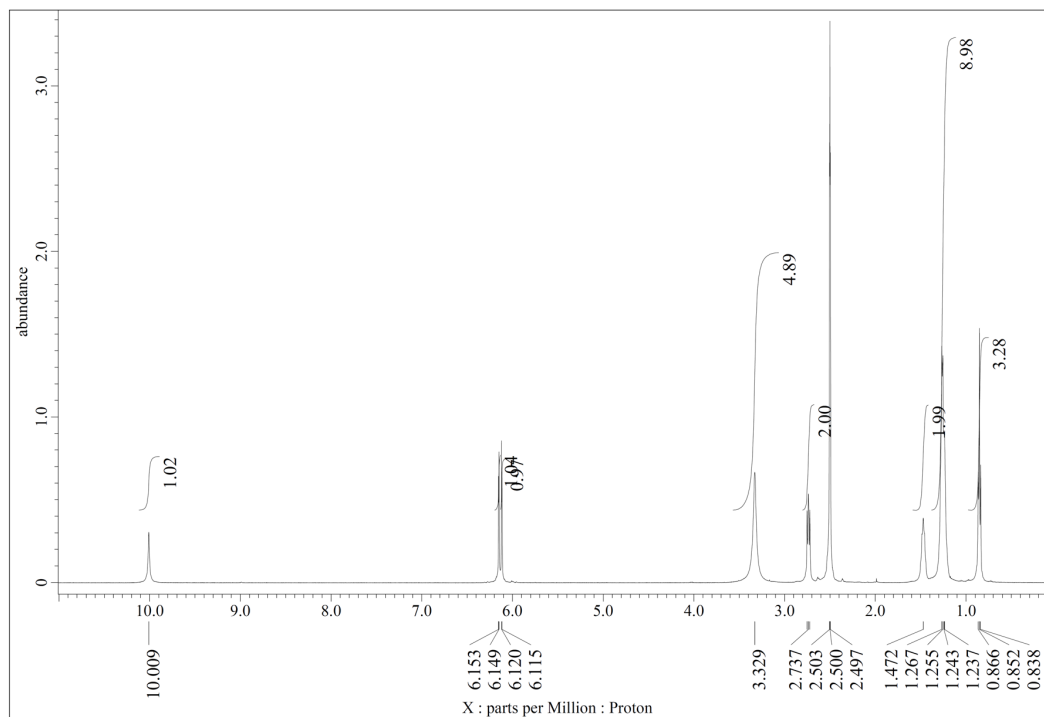
Fig. S27 ^{1}H NMR (500 MHz) spectrum of phorolic acid (**3c**) in DMSO-d_6.
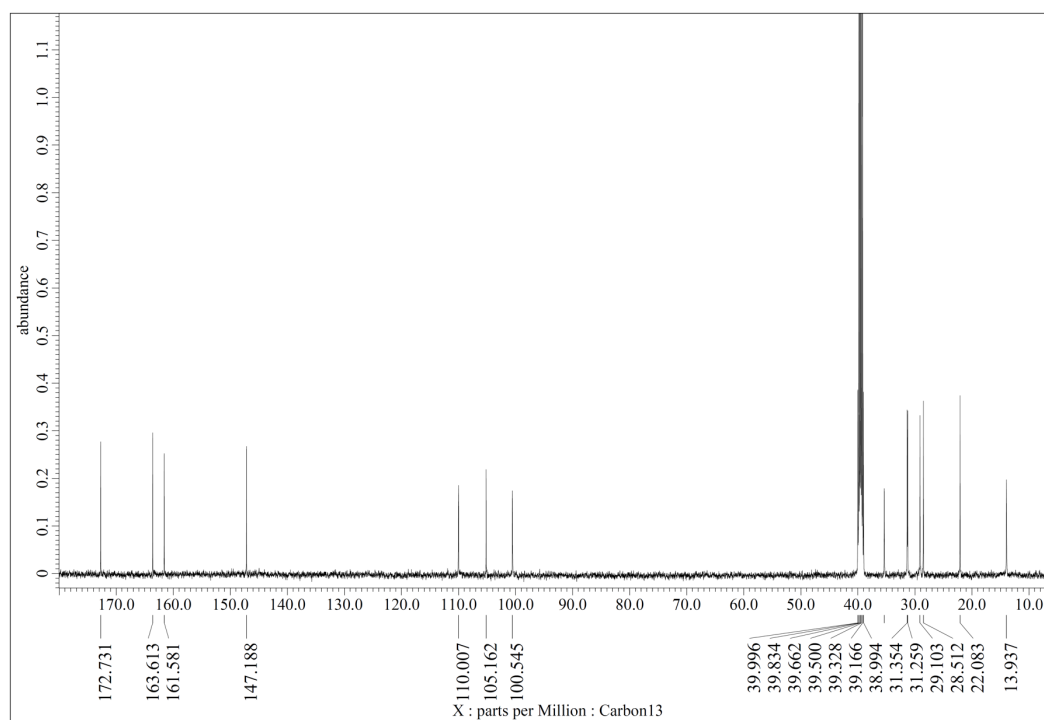
Fig. S28 ^{13}C NMR (125 MHz) spectrum of phorolic acid (**3c**) in DMSO-d_6.
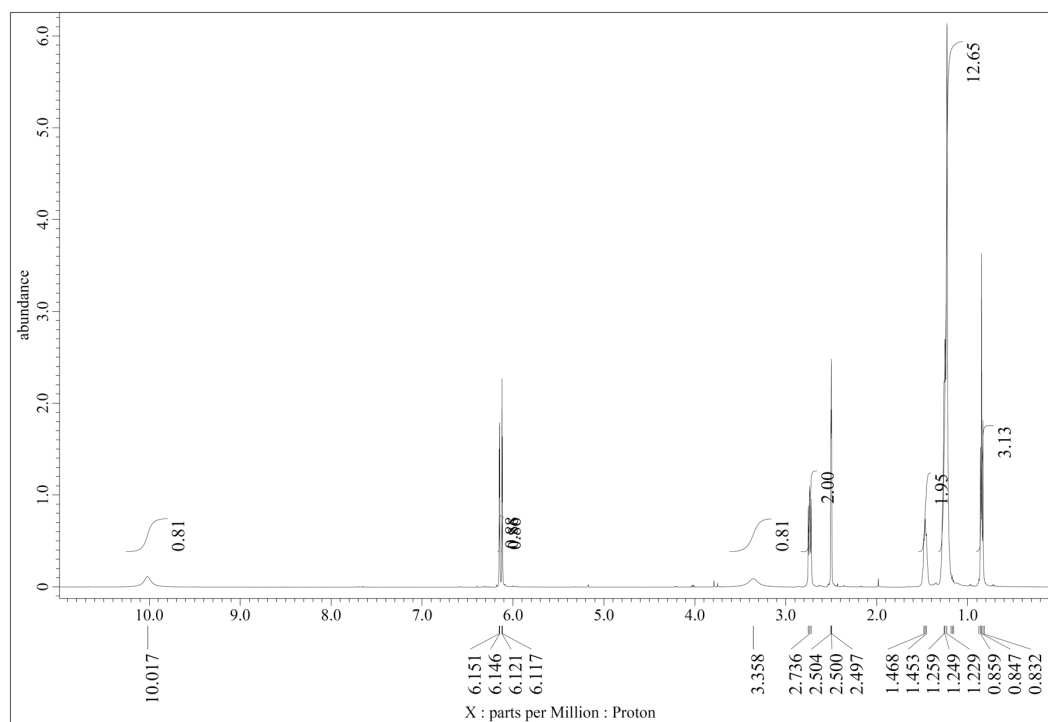
Fig. S29 ^{1}H NMR (500 MHz) spectrum of 2,4-dihydroxy-6-heptylbenzoic acid (**3d**) in DMSO-d_6.
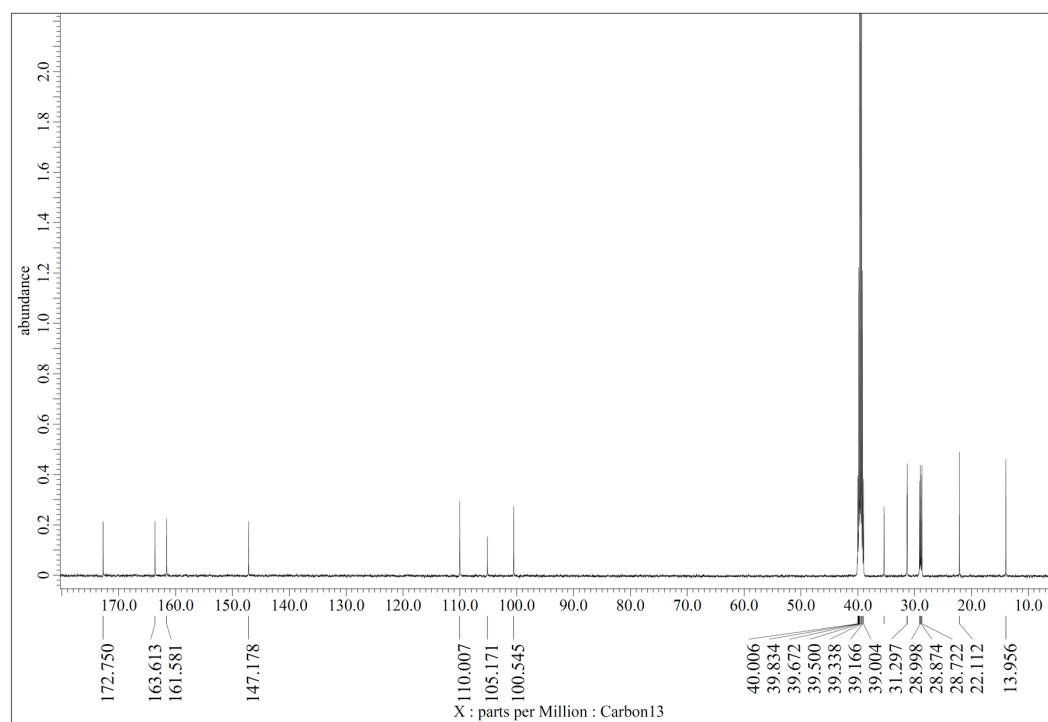
Fig. S30 ^{13}C NMR (125 MHz) spectrum of 2,4-dihydroxy-6-heptylbenzoic acid (**3d**) in DMSO-d_6.
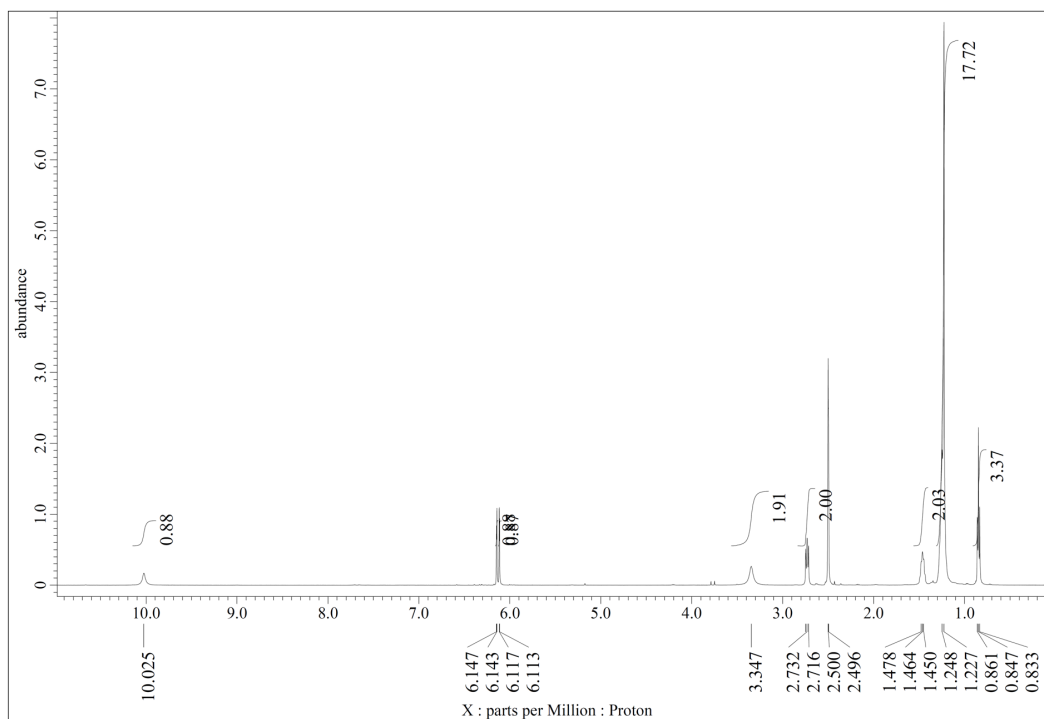
Fig. S31 ^{1}H NMR (500 MHz) spectrum of 2,4-dihydroxy-6-undecylbenzoic acid (**3e**) in DMSO-d_6.
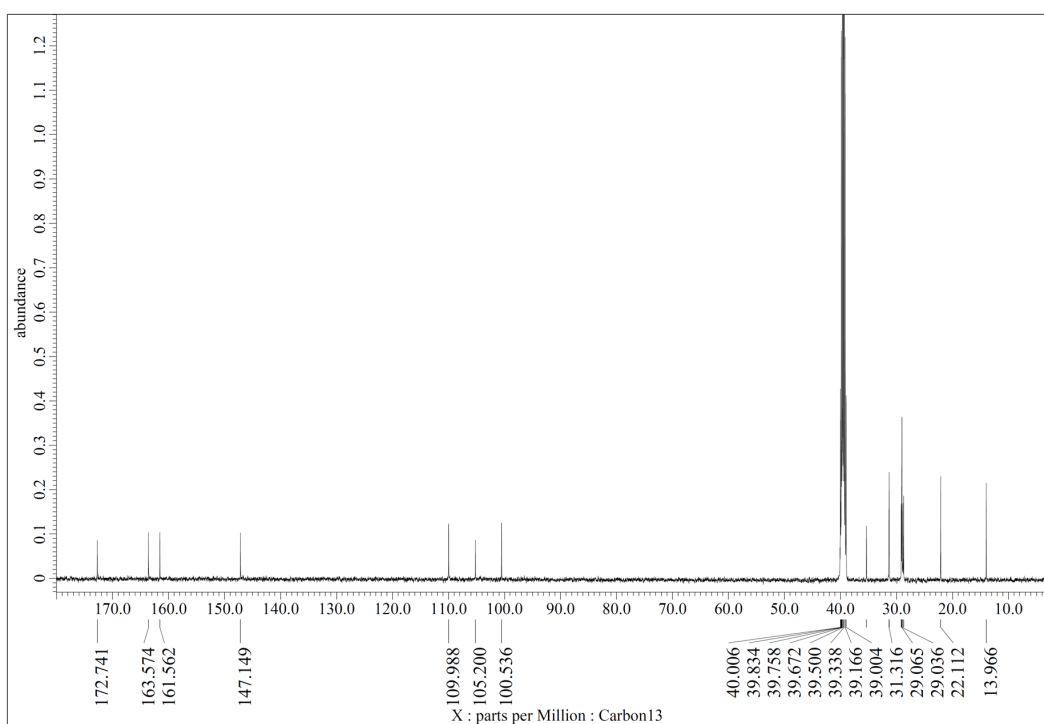
Fig. S32 ^{13}C NMR (125 MHz) spectrum of 2,4-dihydroxy-6-undecylbenzoic acid (**3e**) in DMSO-d_6.

115
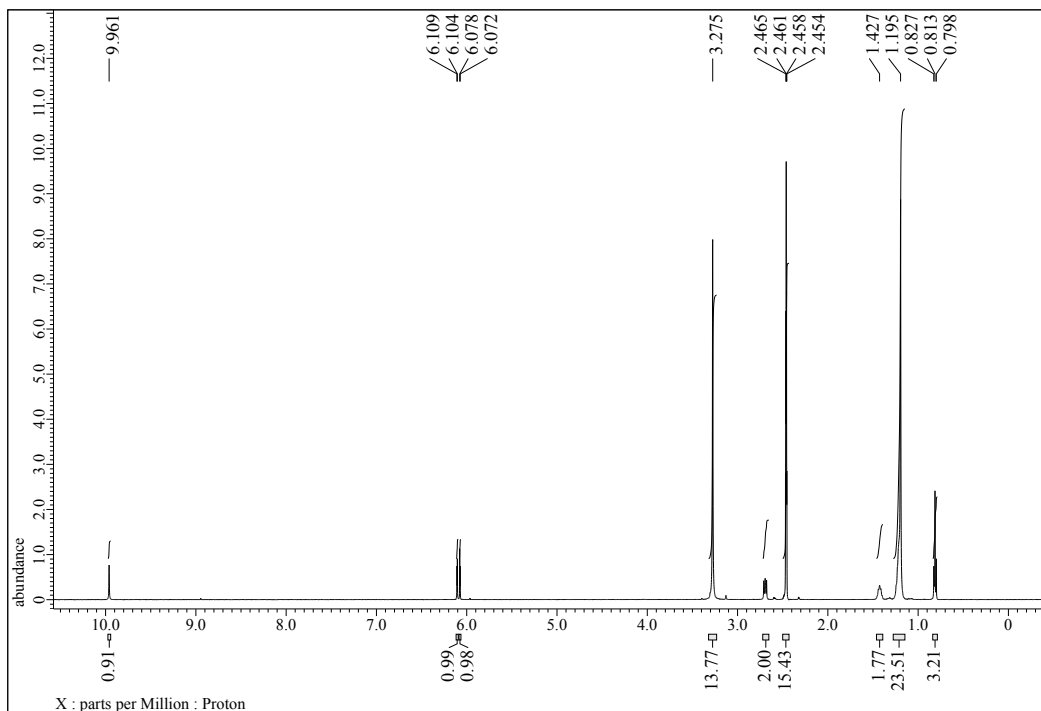
Fig. S33 ^{1}H NMR (500 MHz) spectrum of 2,4-dihydroxy-6-tridecylbenzoic acid (**3f**) in DMSO-d_6.
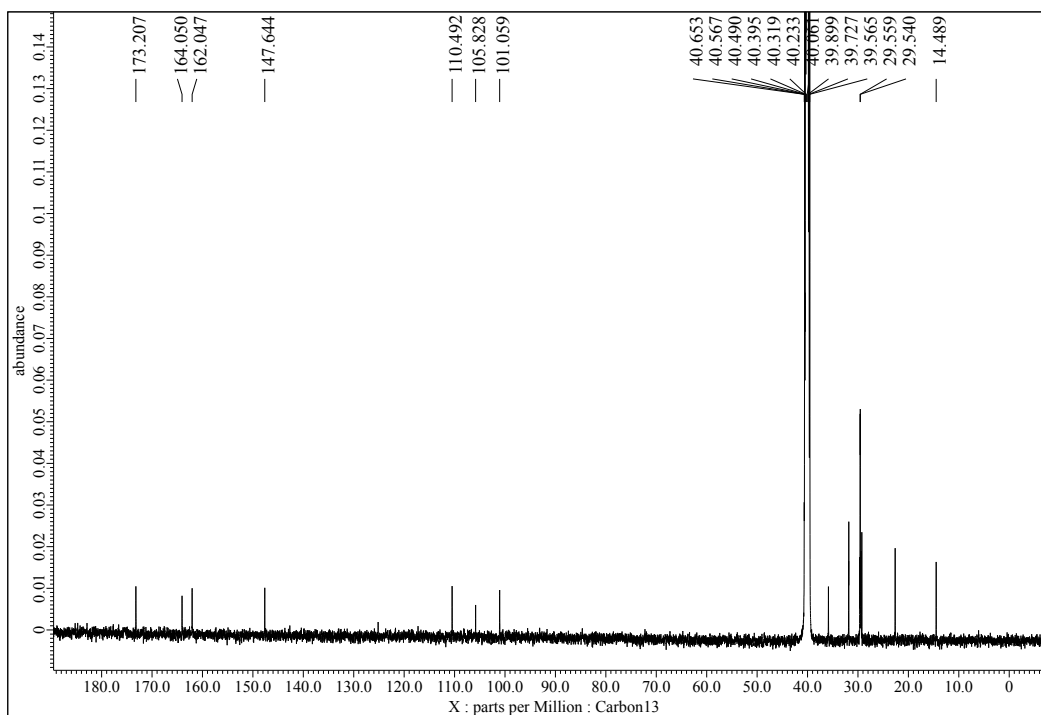
Fig. S34 ^{13}C NMR (125 MHz) spectrum of 2,4-dihydroxy-6-tridecylbenzoic acid (**3f**) in DMSO-d_6.
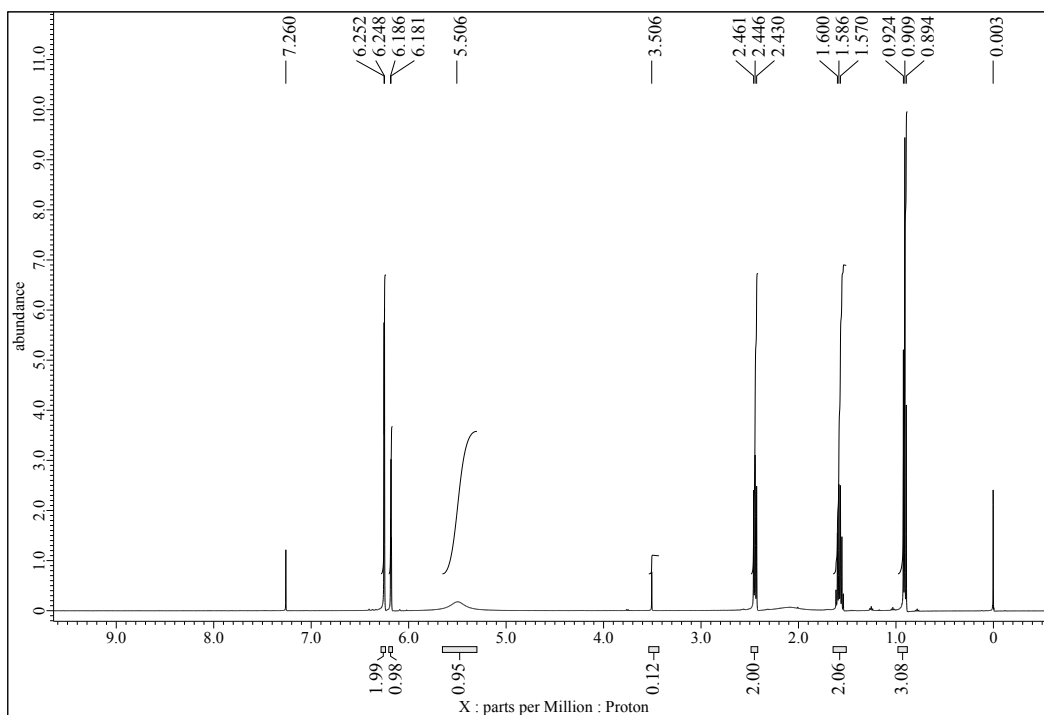
Fig. S35 ^{1}H NMR (500 MHz) spectrum of 5-propylbenzene-1,3-diol (**4a**) in DMSO-d_6.
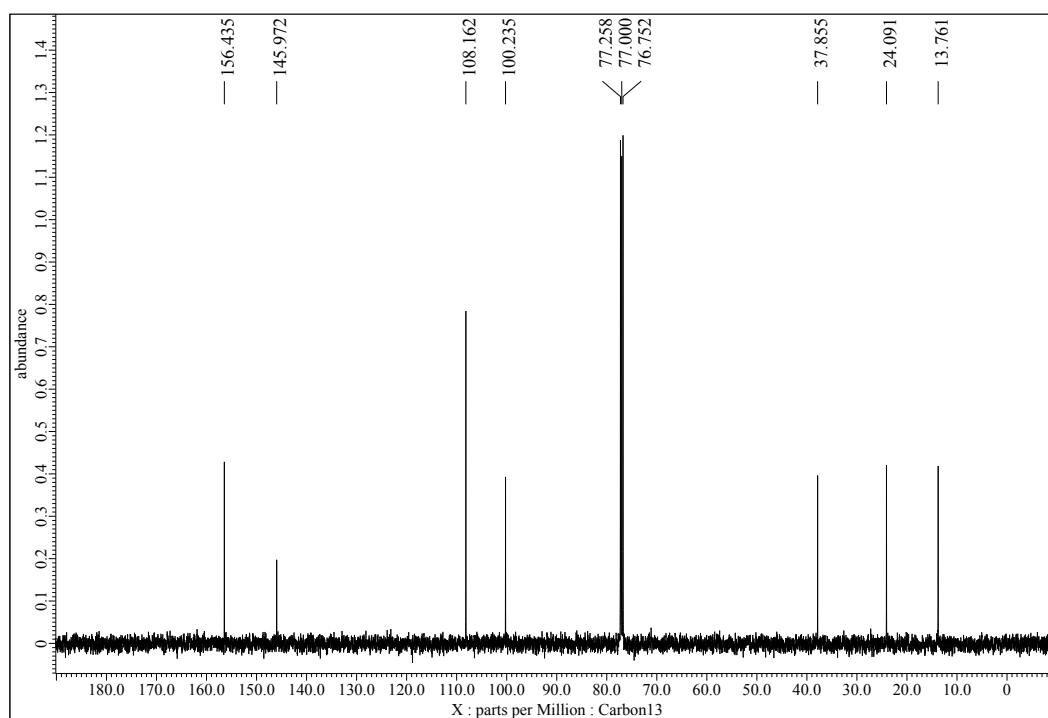
Fig. S36 ^{13}C NMR (125 MHz) spectrum of 5-propylbenzene-1,3-diol (**4a**) in DMSO-d_6.
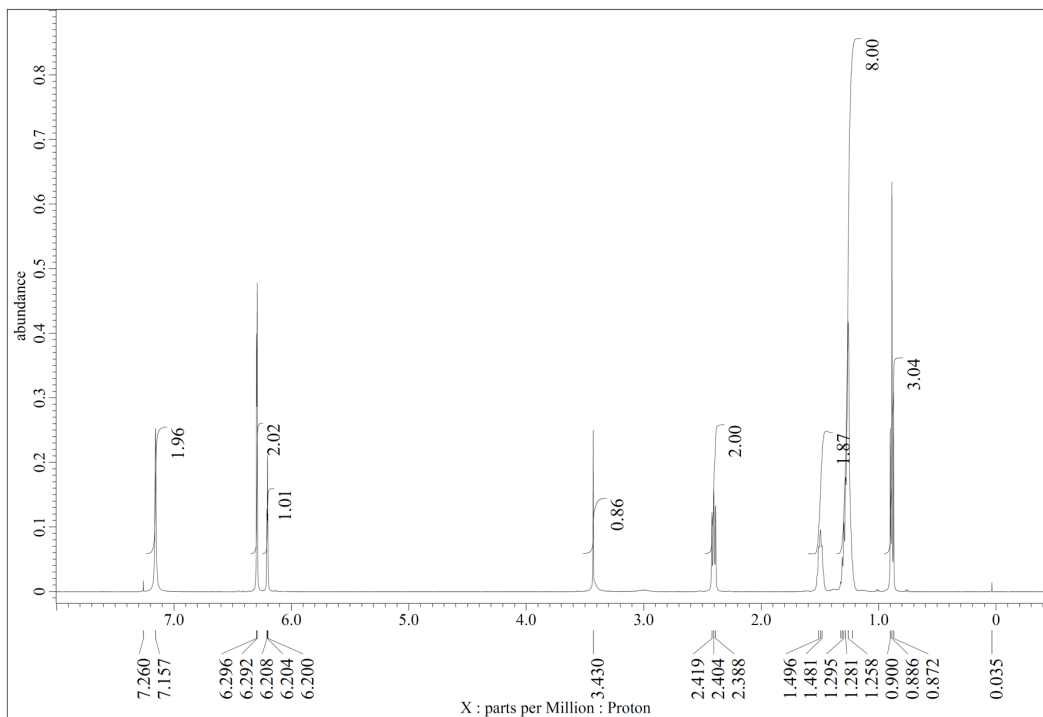
Fig. S37 ^{1}H NMR (500 MHz) spectrum of spherophorol (**4c**) in CDCl$_3$.
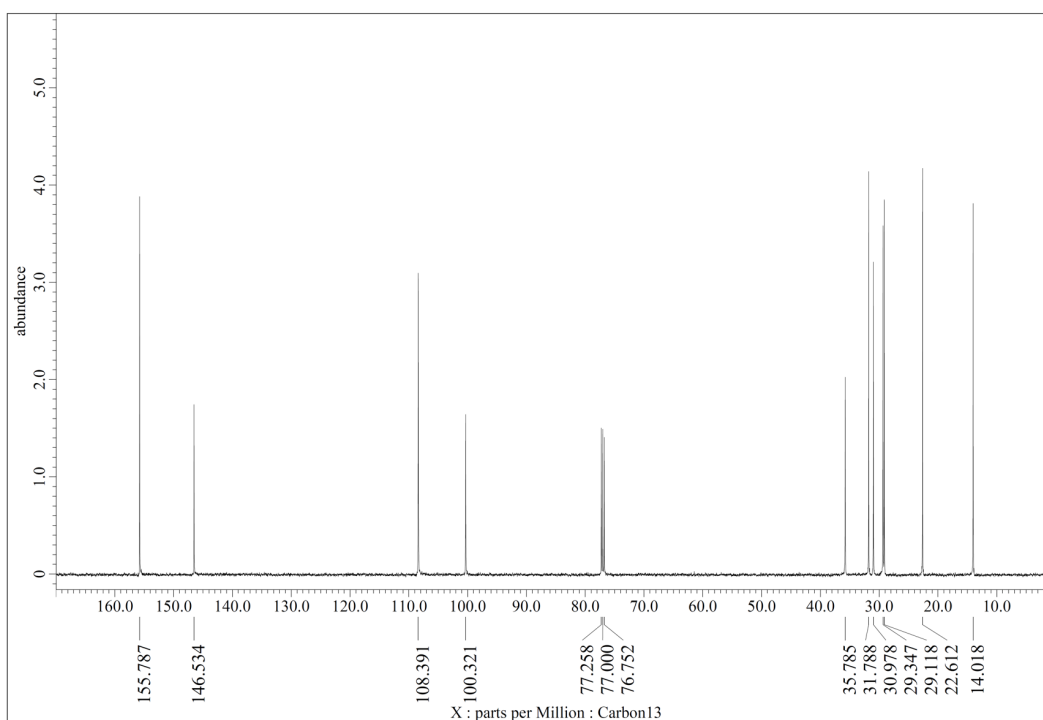
Fig. S38 ^{13}C NMR (125 MHz) spectrum of spherophorol (**4c**) in CDCl$_3$.

118
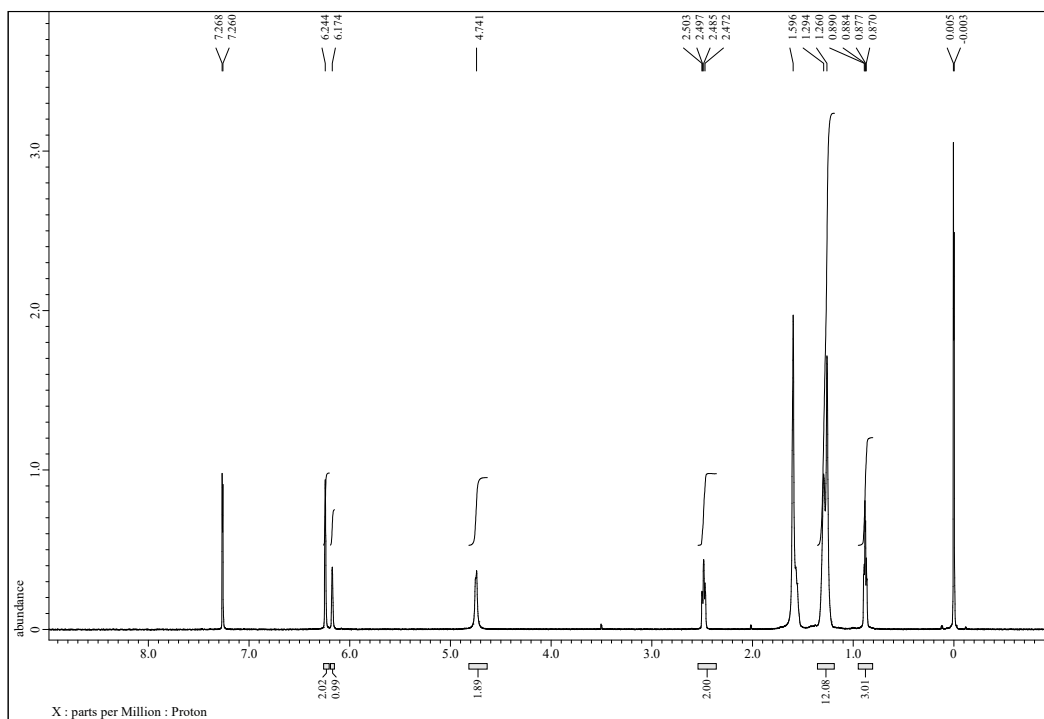
Fig. S39 ¹H NMR (500 MHz) spectrum of 5-nonylbenzene-1,3-diol (**4d**) in CDCl₃.
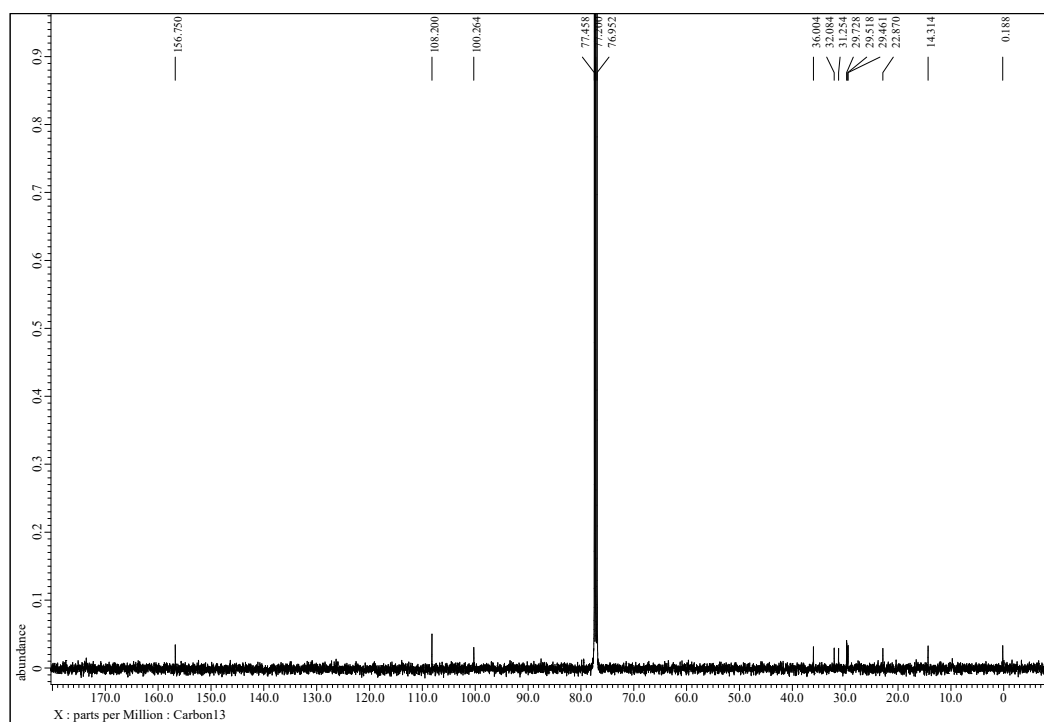
Fig. S40 ¹³C NMR (125 MHz) spectrum of 5-nonylbenzene-1,3-diol (**4d**) in CDCl₃.
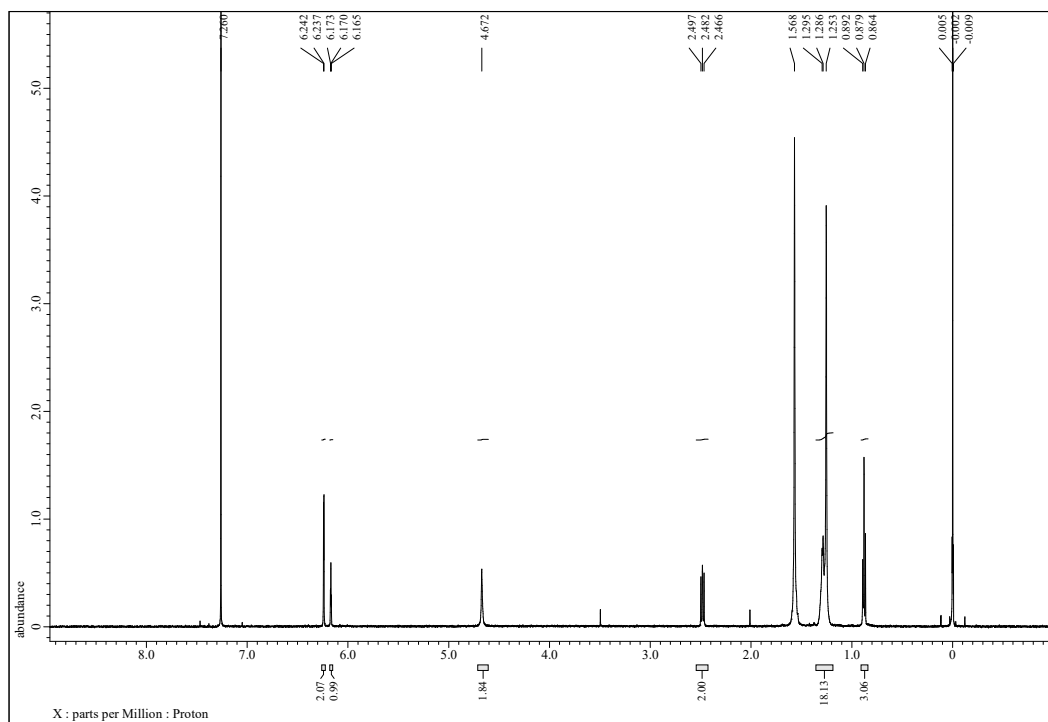
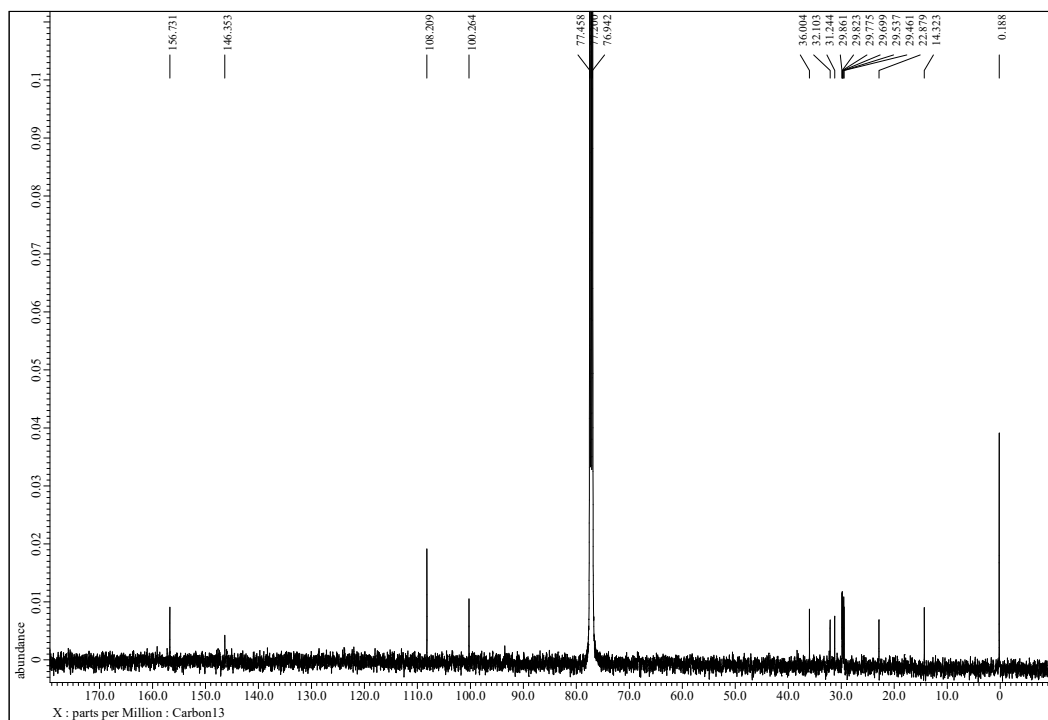**Fig. S41** ^{1}H NMR (500 MHz) spectrum of 5-undecylbenzene-1,3-diol (**4e**) in CDCl$_3$.

Fig. S42 ^{13}C NMR (125 MHz) spectrum of 5-undecylbenzene-1,3-diol (**4e**) in CDCl$_3$.
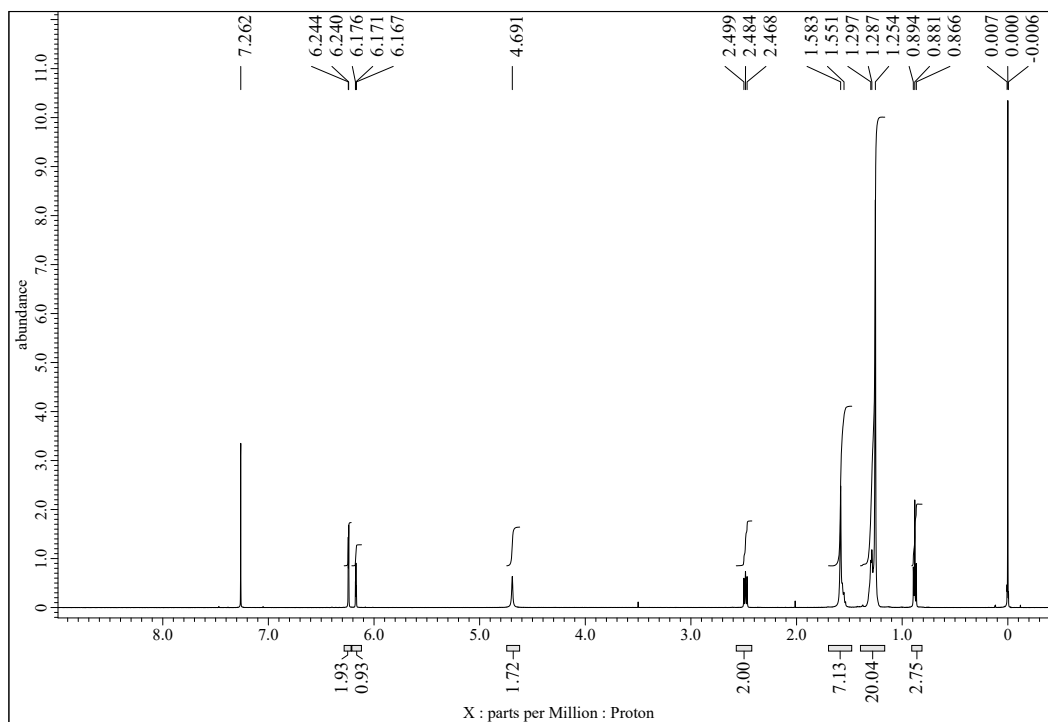
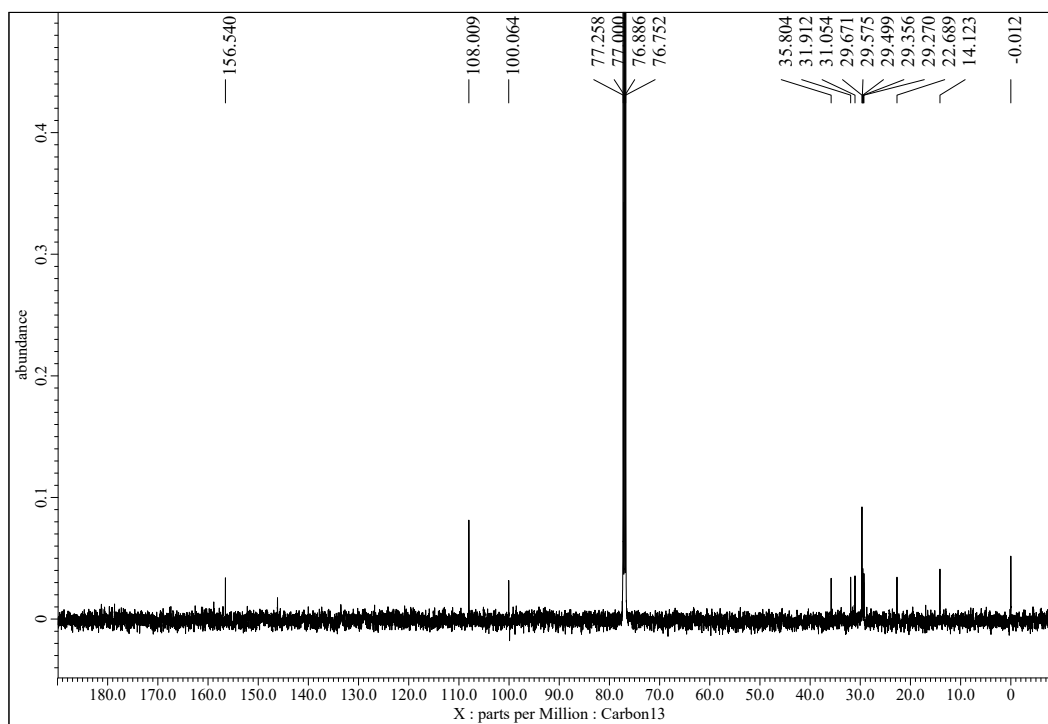**Fig. S43** ^{1}H NMR (500 MHz) spectrum of Grevillol (**4f**) in DMSO-d_6.

Fig. S44 ^{13}C NMR (125 MHz) spectrum of Grevillol (**4f**) in DMSO-d_6.